A search for muon-catalysed dd fusion in a deuterated organic crystal

Marian Jean Oliver

A thesis submitted to the University of Cape Town
in fulfilment of the requirements for the degree of
Master of Science in Physics

November 1992

Abstract

The possibility of muon-catalysed dd fusion via a Vesman-type mechanism in an organic crystal of deuterated anthracene is considered. In order to test this possibility the production of muons by 200 MeV protons incident on a 1 mm Pb target is investigated. Two experiments to search for evidence of muon-catalysed fusion in a cylindrical deuterated anthracene crystal (9 mm diameter by 20 mm length) are described. The results indicate, tentatively, a fusion rate of 0.2 – 1.1 per incident μ^-.

Acknowledgements

I should like to express my sincere gratitude to:

Professor F.D. Brooks, my supervisor and friend, whose unfailing encouragement, boundless enthusiasm, and availability at all times have been a constant source of inspiration to me;

Saalih Allie, POD[1], for much assistance with computing matters, and for a great deal of encouragement and jocularity interspersed among the prophecies;

Andy Buffler, OBP[2], whose assistance in the preparation of diagrams spared me from many hours (days?) of painstaking labour;

Colin Henderson, KCM[3], and Richard Newman, ITH[4], for their proofreading and suggestions;

Rudolph Nchodu, BBC[5], for his readiness to relieve me of various tasks during times of crisis;

The staff of the National Accelerator Centre, for their cooperation and efficiency;

The Foundation for Research Development, for financial assistance.

[1]Prophet of Doom
[2]Owned By Paula
[3]Knight of the Order of the Catalysing Muon
[4]Is This Hillbrow?
[5]'Bold and Beautiful' Connoisseur

For Timothy, who is always with me, despite his absence.
ὃν οἱ θεοὶ φιλοῦσιν ἀποθνήσκει νέος

Contents

List of Figures

List of Tables

This it is that leads me to stay awake through the
quiet of the night, studying how by choice of
words and the poet's art I can display before
your mind a clear light by which you can gaze
into the heart of hidden things.

Lucretius (c. 100 - 55 B.C.)
'On the Nature of the Universe'

Chapter 1

Introduction

1.1 Discovery of the muon

The discovery of the muon in 1938 was the culmination of two years of detective work [An 36, Ne 37, Ne 38] by Anderson and Neddermeyer, whose findings were supported by those of Street and Stevenson [St 37]. The mystery at hand was the identity and nature of certain highly penetrating cosmic ray particles observed during experiments they were conducting with the same Wilson cloud chamber in which the positron had been discovered a few years earlier. These particles were able to traverse thick layers of heavy materials such as lead, lost energy only by ionization, and had unit electric charge, so the first attempts to identify them were, quite naturally, in terms of the only charged particles known at the time viz. electrons, positrons or protons.

However the clues provided by the experiments made it difficult to recognize the particles as protons. The most important of these was that the spectrum of δ rays (electron secondaries) produced by these particles contained too large a proportion of high energy electrons compared with the energy spectrum expected from a particle as massive as the proton. Rather, the spectrum indicated that the particles producing the secondaries were much lighter than protons. In addition to this, there were approximately equal numbers of these positively and negatively charged particles at sea-level, which meant that the existence of negatively charged protons would have to be assumed.

Various difficulties also prevented the identification of the cosmic ray particles as electrons and positrons. One of these arose from theoretical calculations performed by Bethe, Heitler and Sauter which showed that high energy electrons should lose considerable amounts of energy through bremsstrahlung. And indeed, Anderson and Neddermeyer had observed individual cases of electrons undergoing large energy losses (sometimes as much as 100 MeV per cm of lead) through radiation. If the penetrating cosmic ray particles had been electrons, the implication would have been that electrons of greater than a few hundred MeV did not lose energy by bremsstrahlung. In a paper describing his involvement in the discoveries of the positron and the muon [An 61], Anderson said of the mysterious particles, " They seemed to be neither electrons nor protons. We tended, however, to lean toward their

interpretation as electrons and 'resolved' the paradox in our informal discussions by speaking of green electrons and red electrons—the green electrons being the penetrating type, and the red the absorbable type which lost large amounts of energy through the production of radiation".

The realisation that the particles could be interpreted neither as protons nor electrons came finally to Anderson and Neddermeyer after they had inserted a 1 cm thick plate of platinum in their cloud chamber [Ne 37]. They found that particles of a given energy which passed through the plate fell into two groups: one was strongly absorbed (electrons and positrons), and the other was highly penetrating. They had to postulate the existence of positive and negative singly charged particles with a mass intermediate between those of the proton and electron. Shortly afterwards Street and Stevenson found excellent evidence [St 37] to support this hypothesis. Later Anderson and Neddermeyer estimated the mass of these particles to be about 240 electron masses [Ne 38]. They were known initially as mesotrons and later as mu mesons, but the term meson came to be reserved for intermediate mass particles which are subject to the strong interaction, so the particles finally became known as muons.

Much work has been done since the nineteen-thirties to establish the properties of the muon accurately. It is now known to be a second-generation lepton with a mass of 106 MeV (207 times the mass of its first-generation counterpart, the electron, into which it decays), and having a lifetime for free decay of 2.2 μs.

1.2 Muon-catalysed fusion

In 1956 Luis Alvarez and his collaborators observed some unusual events on the photographic film exposed during an experiment performed at Berkeley, in which K^- mesons were stopped in a 10-inch liquid hydrogen bubble chamber [Al 57]. The quality of the separated K^- beam was such that the tracks they observed were made mostly by negative pions or muons, while many were also due to protons or positively charged pions and muons. The 15 interesting events (see Figure 1.1 for an example) which stood out from the several thousand observed π^- and μ^- stoppings were caused by a negative particle brought to rest in the hydrogen, then, after drifting as a neutral particle, giving rise to another negative particle, which in turn decayed into an electron after a 1.7 cm range. Even if π^- nuclear capture had not precluded it[1], these events could not have been π^-–μ^-–e^- decays since the 4.1 MeV muons from pion decay at rest would have a range of 1.0 cm in hydrogen. In fact, the curvature and range of the primary tracks seemed to indicate that they had been made by negative muons, while the gaps between primary and secondary tracks were interpreted as the diffusion of small, neutral, muonic atoms. The energy spectrum of electrons from the decay of the secondary particles revealed them also to be muons, with a unique energy of 5.4 MeV, determined from their range. The real puzzle to be solved was thus not the identification of the particles responsible

[1]The timescale of the nuclear capture reaction is considerably shorter than the lifetime of the pion.

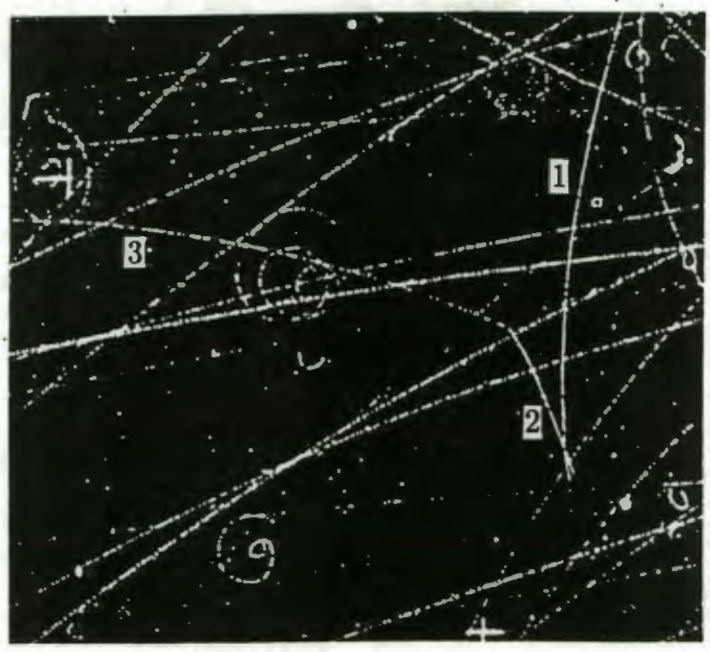

Figure 1.1: A muon-catalysed pd fusion seen by Alvarez *et al.* The incident muon (1) is brought to rest and captured to form a neutral dμ atom which recoils leaving a gap between the primary track and the secondary (2) made by the 5.4 MeV muon released after the fusion reaction. The muon stops again and decays into an electron (3).

for the tracks, but rather, the origin of the 5.4 MeV imparted to each secondary muon.

The suggestion that the energy was provided by a fusion reaction was made by Jack Crawford [Al 72], a Berkeley astrophysicist. The entire research group then discussed this possibility with Edward Teller, and eventually published its explanation of the events as follows [Al 57]: the primary muon comes to rest and is captured by a proton to form a pμ^- muonic hydrogen atom. This neutral atom is then free to drift until it encounters an HD molecule. The deuteron, because of its higher mass, robs the μ^- from the pμ^- atom and forms a more tightly bound dμ^- atom, which recoils from the muon transfer like a heavy neutron (hence the gap between primary and secondary tracks). The dμ^- then binds with a proton to form a (pdμ)$^+$ muonic molecular ion. In this system the p-d separation is about 200 times smaller than that in the ordinary (pde)$^+$ molecular ion (to a good approximation, the linear dimension scales as m_e/m_μ), thus the probability of the two nuclei penetrating the repulsive Coulomb barrier between them is greatly enhanced. The p and d fuse to form ^{3}He, and in some cases the 5.4 MeV released in the reaction is carried off by the muon through the mechanism of internal conversion.

Thus it was that Alvarez *et al.* stumbled across muon-catalysed fusion (μCF), a phenomenon which, quite unbeknown to them at the time, had been proposed some nine years earlier by Frank [Fr 47] and others [Sa 48, Ze 54].

The initial burst of activity started by the discovery of μCF quietened down until around 1966. Feverish experimental and theoretical research was then sparked off by the work of Dzhelepov *et al.*, leading to an understanding of a fascinating mechanism of resonant muomolecular formation in ddμ and dtμ fusion. The muon-

catalysed dd and dt fusion rates are therefore orders of magnitude larger than the pdμ fusion rate which depends on molecular formation via the Auger effect.

1.2.1 ddμ fusion

Fusion experiments using deuterium established that after the stopping and atomic capture of muons, and the deexcitation of muonic atoms, the formation rate $\lambda_{dd\mu}$ of ddμ molecules was an order of magnitude higher than the expected rate [Ge 77], calculated in a manner analogous to that which had yielded rates consistent with experimental measurements for pdμ formation in hydrogen. In addition $\lambda_{dd\mu}$ was found to increase fourfold when the temperature of the deuterium was raised from 113 K to 373 K (resulting in an increase of 0.04 eV in collision energy) [Ge 77].

To account for this discrepancy between theory and experiment, Vesman suggested the following ddμ molecular formation mechanism, depicted in Figure 1.2, in 1967 [Ve 67]. The ddμ molecule possesses a very weakly bound state with rotational and vibrational quantum numbers J and v both equal to 1. The sum of the binding energy $|\varepsilon_{11}| = 1.97$ eV of the molecule in this state and the kinetic energy ϵ_0 of the dμ + D_2 collision prior to binding goes into exciting the νth vibrational state of a compound molecule $[(dd\mu)dee]_{\nu K}$, which forms in the rotational state $K = 1$ and in which the $(dd\mu)^+$ muomolecular ion serves as a nucleus (replacing one of the deuterons in the ground state of a D_2 molecule, which has $K = 0, \nu = 0$). The formation of the excited compound molecule thus allows the ddμ to survive, and the process is a resonant one because varying the temperature of the deuterium is like 'tuning' ε_0 until $\varepsilon_0 + |\varepsilon_{11}|$ matches the energy difference between the $K = 1$, ν state of the compound molecule $[(dd\mu)dee]$ and the ground state of the initial D_2 molecule. Were it not for the Vesman mechanism, the ddμ would be able to form only with the ejection of an electron from the compound molecule, i.e.

$$d\mu + D_2 \rightarrow [(dd\mu)de]^+ + e \ ,$$

and while this process does indeed occur, it is with a probability very much smaller than that governing the formation of $[(dd\mu)dee]$ molecules. The molecular formation rate $\lambda_{dd\mu}$ is therefore temperature-dependent partly because of the temperature-dependence of the initial rotational states K_i of the deuterium molecule, but mainly because the initial dμ + D_2 kinetic energy ε_0 varies with temperature according to the Maxwell distribution.

Figure 1.3 depicts the ddμ fusion cycle, showing the intermediate steps of dμ formation and three possible fusion reactions (distinguished by their reaction products), two of which lead to the release of the catalysing muon and therefore the possibility of it entering the cycle again. The dμ atoms can occur in either of two hyperfine states ($F = \frac{1}{2}, \frac{3}{2}$) 48.5 meV apart [Br 89]. There is some probability for back decay of a ddμ molecule to these atomic states in the reverse of the molecular formation reaction

$$d\mu + [D_2]_{\nu_i K_i} \rightarrow [(dd\mu)_{11}dee]^*_{\nu_f K_f} \ .$$

Thus a certain fraction of ddμ molecules is lost from the fusion cycle, and the effective molecular formation rates $\tilde{\lambda}_{dd\mu}^{F=\frac{1}{2}}$ and $\tilde{\lambda}_{dd\mu}^{F=\frac{3}{2}}$ (which lead to fusion) are governed by

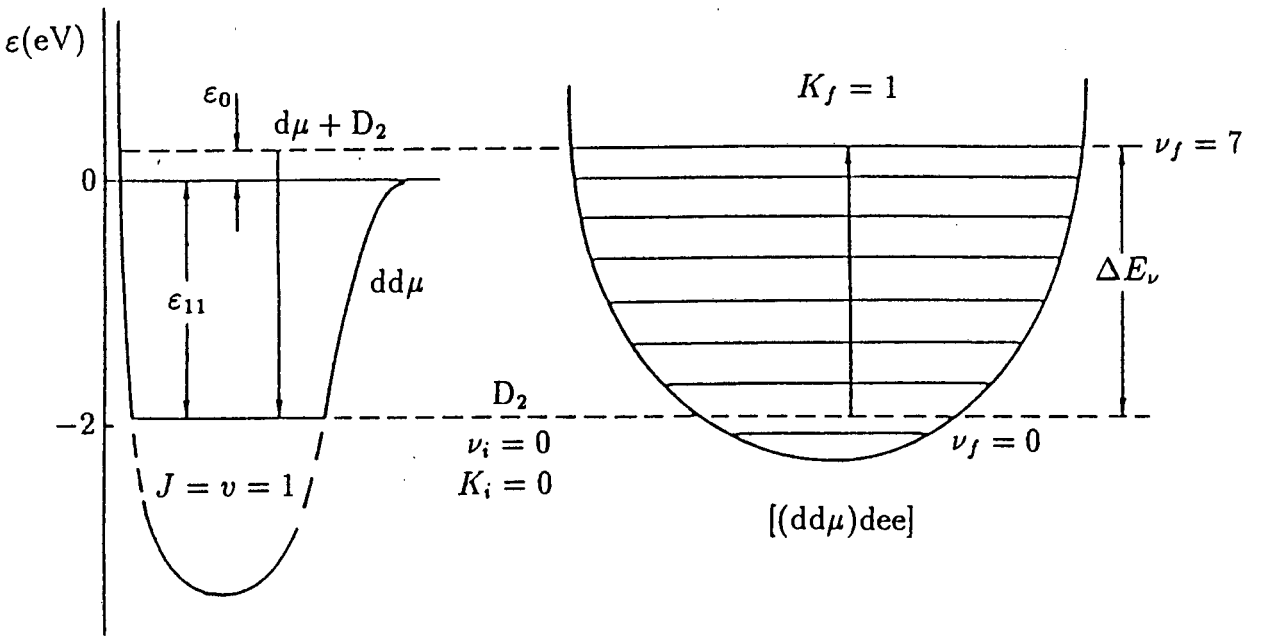

Figure 1.2: Energy level scheme of the resonance formation of the ddμ molecule: ε_0 is the kinetic energy of the dμ + D_2 collision, $|\varepsilon_{11}|$ the binding energy of the ddμ molecule in the state ($J = 1,\ v = 1$). The resonance condition is met when the released energy $\varepsilon_0 + |\varepsilon_{11}|$ is transferred to the excitation of the [(ddμ)dee] molecule in the rotational state $K = 1$ and vibrational state $\nu = 7$ from the ground state ($K = 0,\ \nu = 0$) of the D_2 molecule. From [Po 90].

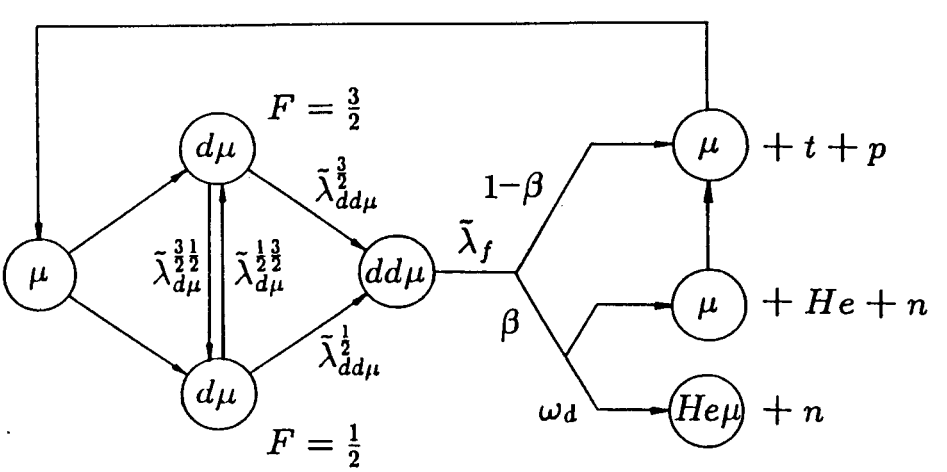

Figure 1.3: Schematic diagram of the ddμ fusion cycle. From [Br 89].

the strength of this back decay. The average effective molecular formation rate $\tilde{\lambda}_{dd\mu}$ has been measured[2] accurately and found to be $\tilde{\lambda}_{dd\mu} = (2.76 \pm 0.08) \times 10^6$ s^{-1} at 300 K [Ba 84], in excellent agreement with theory. The experimentally measured ddμ binding energy (excluding hyperfine splitting) is $\varepsilon_{11} = -1965.9 \pm 0.3$ meV, which is within ~ 1 meV of the calculated values [Br 89].

The ddμ fusion cycle in pure deuterium is thus now well understood, in contrast to the more complicated dtμ cycle.

1.2.2 dtμ fusion

The understanding of the resonant ddμ formation mechanism in deuterium led to some exciting predictions regarding dt fusion in tritium mixtures. In 1977 Gerstein and Ponomarev estimated that the rate governing molecular formation in the process $t\mu + D_2 \rightarrow [(dt\mu)dee]^*_{K=1,\nu}$ would be a maximum for $\nu = 4$, and would be $\lambda_{dt\mu} \approx 10^8$ s^{-1}—about two orders of magnitude faster than the corresponding rates in other fusion cycles, and more than two orders of magnitude greater than the muon decay rate of 4.55×10^5 s^{-1}—and that a single negative muon in the dt mixture could catalyse ~ 100 fusions, releasing ~ 2 GeV of energy [Ge 77]. These predictions were made after calculations done by Vinitsky *et al.* had put the binding energy of the $J, \nu = 1, 1$ dtμ state at $\varepsilon_{11} = -1.1$ eV, and had led to the expectation that the dtμ molecular formation rate in dt mixtures would be strongly temperature-dependent, in like manner to the ddμ formation rate in deuterium [Vi 77].

In an early experiment using a low-tritium-concentration D_2-T_2 mixture, Bystritsky *et al.* confirmed the high rate expected for dtμ formation [By 80]. They measured the absolute neutron yield Y_n and its time distribution dN/dt for the reaction $dt\mu \rightarrow {}^4He + n + \mu^- + 17.6$ MeV, and obtained a rate of muon transfer from deuterium to tritium of $\lambda_{dt} = (2.7 \pm 0.9) \times 10^8$ s^{-1}, and found a lower limit (at the 90 % confidence interval) for the dtμ molecular formation rate of $\lambda_{dt\mu} > 10^8$ s^{-1}. These results were later verified in an experiment performed by Jones *et al.*, which will be discussed below.

Figure 1.4 shows a scheme of the dtμ fusion cycle. The muon is brought to rest and captured by a deuteron or a triton, the probabilities for dμ or tμ atomic formation being determined by the concentrations of deuterium and tritium in the mixture. For the sake of clarity Figure 1.4 does not depict the dμ hyperfine states. The cascade of $(d\mu)^*$ atoms down to the ground state is followed by transfer of the muon to tritium via the irreversible isotopic exchange reaction $d\mu + t \rightarrow t\mu + d$ [Po 90] at a rate λ_{dt}. The tμ atoms can form in singlet ($F = 0$) or triplet ($F = 1$) states, with the hyperfine transition between them proceeding via the processes

$$(t\mu)^1 + t \rightarrow (t\mu)^0 + t$$

$$(t\mu)^1 + d \rightarrow (t\mu)^0 + d \, .$$

The rates for these transitions are different, but are denoted by a single triplet quenching rate $\lambda^{10}_{t\mu}$ in Figure 1.4. The formation of dtμ molecules from tμ atoms

[2]Measurements involve detecting the 2.5 MeV neutrons from dd fusion, or the charged products from the other two reaction channels.

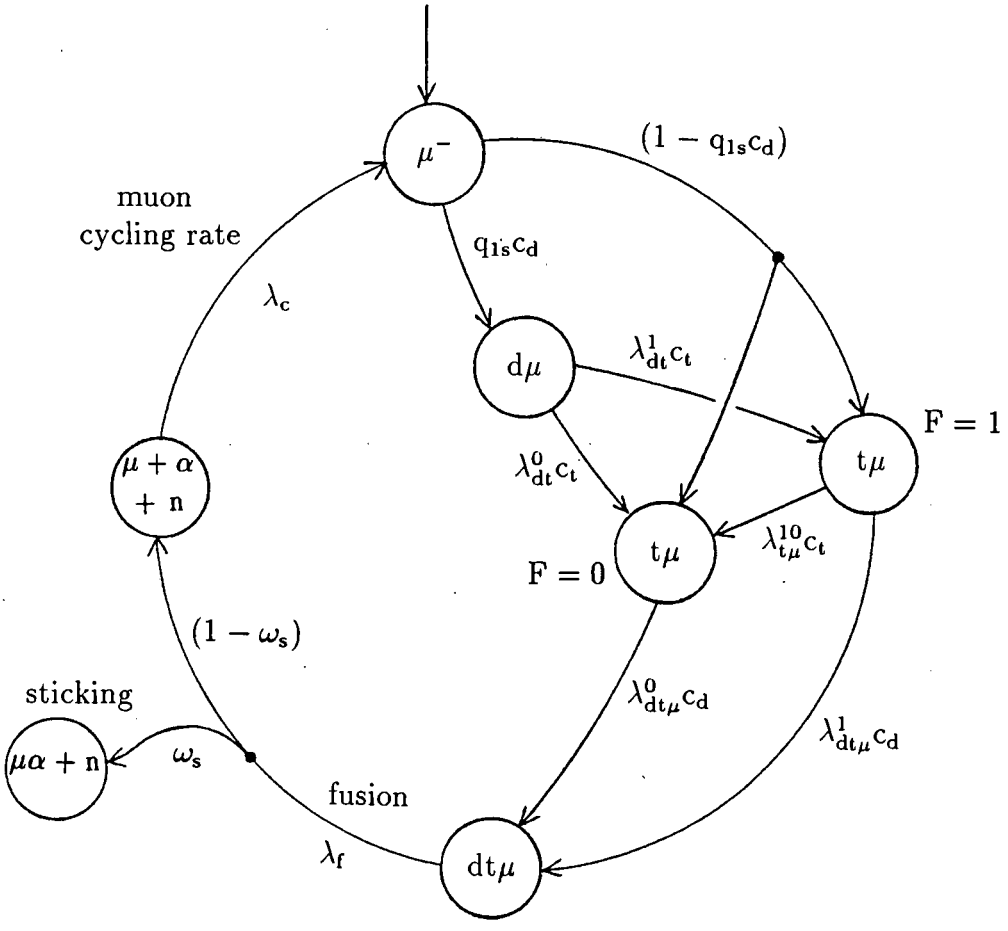

Figure 1.4: Scheme of the dtμ fusion cycle.

occurs at rates $\lambda^1_{dt\mu}$ and $\lambda^0_{dt\mu}$, each of which in turn comprises two components, since the molecular formation can occur through either of the two reactions

$$t\mu + D_2 \rightarrow [(dt\mu)dee]^*$$

$$t\mu + DT \rightarrow [(dt\mu)tee]^*,$$

both of which appear to be resonant, with the former being about three times stronger than the latter [Jo 83]. Thus $\lambda^F_{dt\mu} = \lambda^F_{dt\mu-d}c_d + \lambda^F_{dt\mu-t}c_t$, where c_d and c_t are the concentrations of deuterium and tritium respectively ($c_d + c_t = 1$). The muon cycling rate λ_c depends on the time spent by the muon at each stage in the μCF process. The atomic capture time and the ground state cascade time are both of the order of picoseconds at liquid hydrogen density [Br 89], and the fusion rate λ_f is too large to be measured [Jo 83], so that these processes contribute negligibly to the cycling time. The thermalization time of $t\mu$ atoms can also be neglected [Br 84]. The muon cycling time is then given by the sum of the time spent in the $d\mu$ ground state before transfer of the μ to tritium, and the time $t\mu$ atoms in the four (three triplet and one singlet) available states wait for molecular formation. With the aid of Figure 1.4 this can be seen to be

$$\frac{1}{\lambda_c} = \frac{q_{1s}c_d}{\lambda_{dt}c_t} + \frac{3/4}{\lambda^{10}_{t\mu}c_t + \lambda^1_{dt\mu}c_d} + \frac{1/4 + (3/4)\chi}{\lambda^0_{dt\mu}c_d}$$

[Br 89, Le 84] where $q_{1s} < 1$ [Po 90] is the probability that a $(d\mu)^*$ atom will reach the ground state, $\lambda_{dt} = \lambda^0_{dt} + \lambda^1_{dt}$, and χ is the branching ratio of the hyperfine

transition for $t\mu$ atoms

$$\chi = \frac{\lambda^{10}_{t\mu} c_t}{\lambda^{10}_{t\mu} c_t + \lambda^{1}_{dt\mu} c_d}.$$

Muons are removed from the catalysis cycle by a number of processes, the most obvious one being muon decay, which can occur from any stage of the cycle. Then there is some probability ω_s for effective[3] sticking of the muon to the ^{4}He produced in the fusion. Also, as the concentration of ^{3}He from tritium beta decay in the target increases, so do the probabilities of μ capture on these nuclei, and transfer of muons to ^{3}He either during the muonic hydrogen cascade or from the ground states of $d\mu$ and $t\mu$ atoms. Writing the muon decay rate as λ_0, the total probability of muon loss from each cycle as W, and the ratio of the target density N to that of liquid hydrogen ($N_0 = 4.2 \times 10^{22}$ cm^{-3}) as ϕ, the rate of removal of active muons from the cycle can be written $\lambda_n = \lambda_0 + W\phi\lambda_c$ [Br 89]. Substituting this into the expression for the yield (average number of fusions per muon) $Y_n = \phi\lambda_c/\lambda_n$ gives

$$\frac{1}{Y_n} = \frac{\lambda_0}{\phi\lambda_c} + W.$$

In 1983 Jones *et al.* performed the first experiment to investigate μCF in high-density d-t mixtures [Jo 83]. They confirmed the results of Bystritsky *et al.*, finding $\lambda_{dt} = (2.8 \pm 0.3) \times 10^8$ s^{-1} and $\lambda_{dt\mu} > 10^8$ s^{-1}; they were able to separate the components $\lambda_{dt\mu-d}$ and $\lambda_{dt\mu-t}$, and found both to be resonant and temperature-dependent, as predicted. The sticking probability was found to be $\omega_s = (0.77 \pm 0.08)\%$, compared with the theoretical values of 0.86 % [Ge 81] and 0.91 % [Br 82]. The fusion yield was determined to be $Y_n = 90 \pm 10$ fusions per muon (for an equimolar d-t mixture, with $\phi = 1$ and at 540 K), in agreement with the early predictions of Gerstein and Ponomarev.

A later experiment [Jo 86] revealed an unexpected target-density effect on $\lambda_{dt\mu-d}$ and on the sticking probability: the combined effect of the increase in $\lambda_{dt\mu-d}$ and the decrease in ω_s with increasing ϕ leading to a rise in the number of fusions per muon to 150 ± 4(stat.) $\pm$ 20(syst.). The density-dependence of $\lambda_{dt\mu-d}$ is presumed by Jones *et al.* to be a result of three-body contributions to the resonant molecular formation mechanism; that of ω_s is not clear.

Recent calculations by Faifman and Ponomarev [Fa 91], in which they consider the resonant molecular formation

$$t\mu + HD \rightarrow [(dt\mu)pee]$$

in a triple $H_2 + D_2 + T_2$ mixture, indicate that the rate $\lambda_{dt\mu-p}$ could reach a value of 2×10^{10} s^{-1}! These predictions reveal the need for experiments which will study μCF in triple mixtures at high densities over a range of temperatures and concentration ratios.

Thus, despite years of dedicated research, there is still much to be learnt about $dt\mu$ fusion.

[3]There is a possibility for the stuck muon to be stripped from the energetic alpha particle before it comes to rest in the gas. If the probability of stripping is R, then the initial sticking probability ω_s^0 is modified by a factor (1 – R). The effective sticking is thus $\omega_s = \omega_s^0(1 - R)$.

1.2.3 Other fusion cycles

Muon-catalyzed fusion is also possible via the formation of pdμ, ptμ and ttμ molecules. However, since these molecules possess no suitable loosely bound states, no resonant channel is available and the compound molecules form only by Auger processes. These cycles contribute to the muon loss probability W, because they compete with the main dtμ cycle, and they have significantly higher sticking probabilities than dtμ [Br 89].

1.3 Possibility of μCF in deuterocarbon systems

Muon-catalysed fusion experiments have traditionally employed gaseous H_2-D_2 or D_2-T_2 mixtures. Higher-Z atoms are avoided because their introduction would lead to scavenging of muons from the hydrogen isotopes and hence from the catalysis cycle. It is conceivable, however, that dd fusions could be induced by muons in solid or liquid deuterocarbon (deuterated hydrocarbon) targets. The success of muons in catalysing fusions depends on the rate of formation of compound molecules which contain pdμ, ddμ or dtμ atoms. Deuterocarbon systems may, by virtue of their complex molecular structures, provide environments which facilitate the formation of ddμ atoms within compound deuterocarbon molecules, despite the presence of carbon nuclei.

1.3.1 Vibronic states

The total energy E_t of a ground state molecule (excluding its translational energy and internal nuclear energy) can be written [Bi 70]

$$E_t = E_e + E_v + E_r$$

where E_e, E_v and E_r are the electronic, vibrational and rotational energies of the molecule respectively. Using primed symbols to denote excited states, the total energy E'_t of an excited state molecule can likewise be written

$$E'_t = E'_e + E'_v + E'_r \ .$$

An absorption transition can then be defined as

$$\Delta E_x = E'_x - E_x$$

where x is the appropriate subscript t, e, v or r. Absorption spectra can thus be classified as rotational, vibrational, electronic, or various combinations of these. States are referred to as *vibronic* if they involve vibrational and electronic energy only. Vibronic transitions, then, are those which occur between such states. Each electronic absorption transition ΔE_e thus comprises a band of vibronic states provided by the different values of ΔE_v, as illustrated in Figure 1.5.

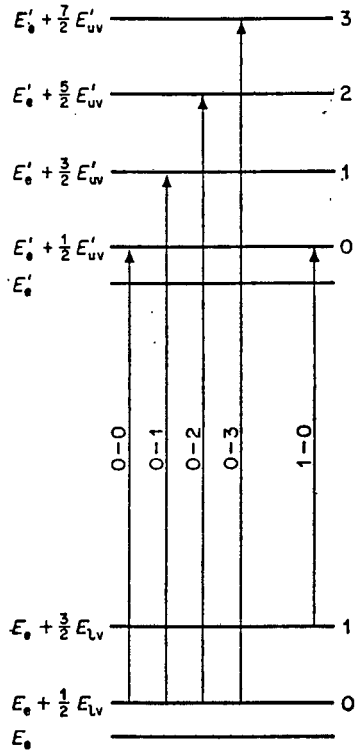

Figure 1.5: Vibronic absorption transitions for a molecule with one dominant vibrational mode, such that it approximates a harmonic oscillator. From [Bi 70].

1.3.2 Molecular structure of anthracene

Anthracene is a pure organic crystalline scintillator with the molecular formula $C_{14}H_{10}$, and having the highest scintillation efficiency of all known organic scintillators. The crystal structure of anthracene is depicted in Figure 1.6.

Aromatic hydrocarbons such as anthracene are complex molecules with many vibronic states. The vibronic structure of each electronic band, resolvable at low temperatures, is blurred by thermal broadening at room temperature, resulting in a system of a few relatively broad maxima [Bi 70].

In deuterated anthracene, dd fusion would result from the muomolecular formation reaction $d\mu + C_{14}D_{10} \rightarrow C_{14}D_9(dd\mu)$. This would occur if the kinetic energy of the $d\mu$ atom and the $dd\mu$ binding energy combined to excite some vibronic state of the $C_{14}D_9(dd\mu)$ compound molecule, thereby allowing the $dd\mu$ to survive in a Vesman type of mechanism. In contrast to the Vesman mechanism, however, this would not be a temperature-dependent resonant process. The $C_{14}D_9(dd\mu)$ compound molecule could provide a matching absorption transition from the continuum of vibrational excitations available in its absorption spectrum. This continuum of absorption transitions is attributed to broadening of the discrete states of the isolated anthracene molecule due to intermolecular coupling in the crystal. The formation of $dd\mu$ muomolecular ions may thus occur over a range of $d\mu$ kinetic energies.

The crystal structure of (deuterated) anthracene could also enhance $dd\mu$ formation. Corridors of deuterons running parallel to the c axis (see Figure 1.6) exist due to the relative orientations of adjacent $C_{14}D_{10}$ molecules. If muons were to enter a deuterated anthracene crystal along its c axis, they could be confined by channelling to regions containing a higher density of deuterons relative to carbon nuclei than in some other direction, thereby improving the muon capture probability for deuterons,

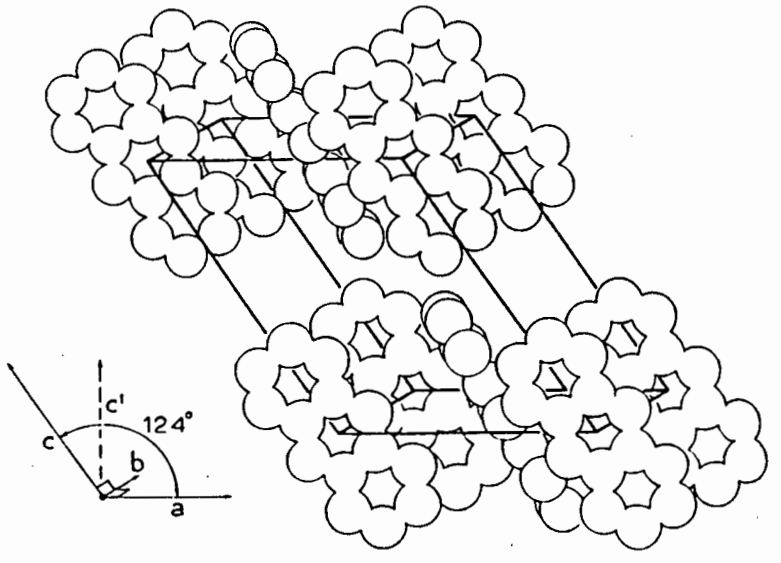

Figure 1.6: Arrangement of molecules in the unit cell of the anthracene crystal. The lengths (in Å) of the sides of the unit cell are $a = 8.56, b = 6.04$ and $c = 11.16$. From [Br 74].

and hence the ddμ formation rate.

1.3.3 Muon interactions in anthracene

Consider the fate of a muon entering deuterated anthracene. If positive, the muon will experience only Coulomb interactions with electrons and nuclei, and decay with its free lifetime of 2.2 μs. If negative, it will be brought to rest and captured to form muonic carbon or deuterium within a nanosecond [Wu69]. The ratio of the capture probabilities on carbon and deuterium is 8.4:1. This is the product of the C:D ratio in anthracene and the ratio of their atomic numbers, since the muon capture probability is proportional to Z [Fe 47], and the atomic capture ratio in a binary compound A_nB_m is thus nZ_A/mZ_B [Wu 69].

Once captured, the muon will then cascade down to lower (muonic) atomic states, reaching the 1s level within 10^{-13} s [Wu 69]. From here it will either decay into an electron, or undergo a nuclear interaction. The nuclear capture time is inversely proportional to Z [Wu 69], and combines with the free lifetime of the muon to form a Z-dependent characteristic lifetime – or disappearance time – for bound muons. This is illustrated in Figure 1.7. In light elements the effect is small, reducing the muon lifetime to around 2.0 μs in carbon. (As Z increases, however, the nuclear capture probability competes more strongly with the muon decay branch, resulting eventually in lifetimes as low as 80 ns).

Figure 1.8 shows the possible channels available to a negative muon finding itself in deuterated anthracene. For a muon initially captured on carbon there are two possibilities, as described above: it will either decay into an electron, or it will undergo nuclear capture in a weak interaction with the carbon nucleus to form

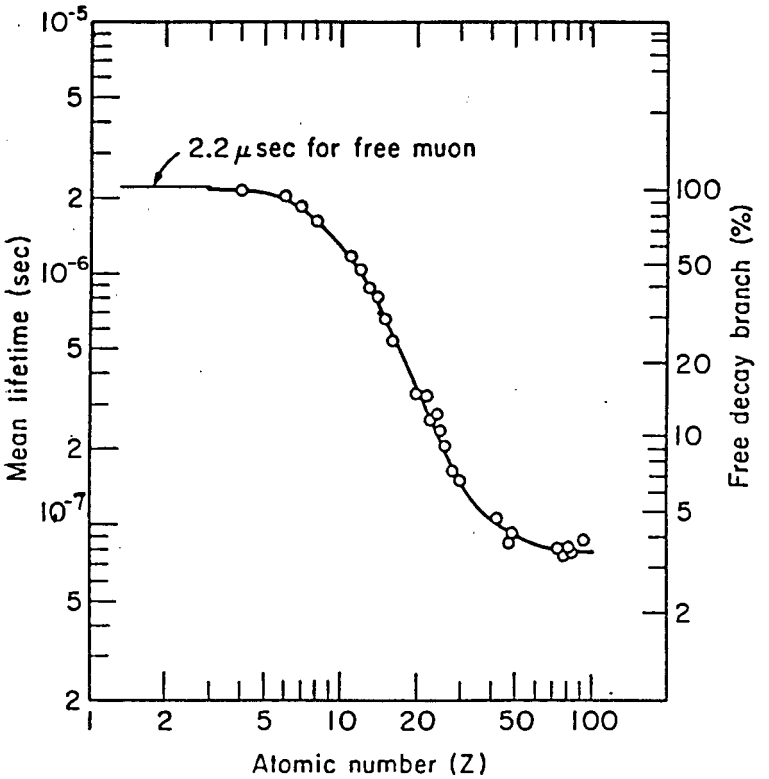

Figure 1.7: Mean lifetimes and decay electron branches of the muonic $1s_{1/2}$ state versus the atomic number Z of the nucleus to which the negative muon is bound. From [Ya 75].

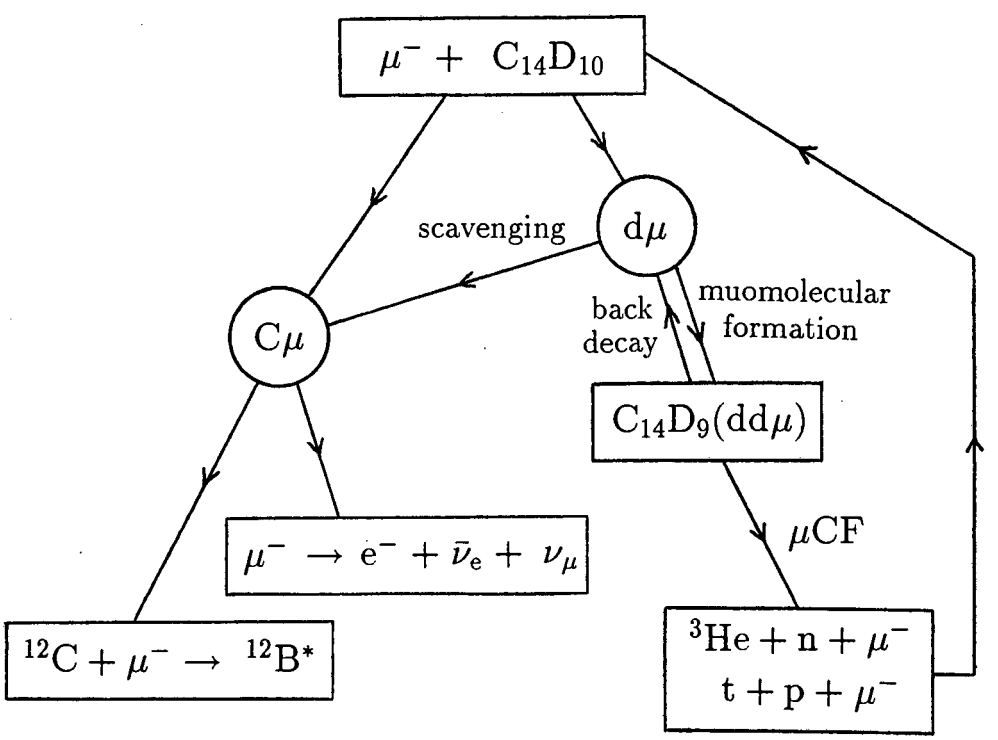

Figure 1.8: Possible muon interactions in deuterated anthracene.

$^{12}B^*$. If the muon initially forms a $d\mu$, however, it has two routes to follow other than disappearing via decay or nuclear capture. It could be scavenged from the d by carbon, or the $d\mu$ could survive to form a compound molecule $C_{14}D_9(dd\mu)$, as suggested in the previous section. The branching ratio for this to occur will depend on the molecular formation mechanism. It may well compete with muon scavenging by carbon if a process *à la* Vesman exists for $C_{14}D_9(dd\mu)$ formation. Presumably $dd\mu$ molecules formed in this way will be subject to back decay in a similar way to those produced in the $[(dd\mu)dee]^*$ complex in pure deuterium [Br 89]. The competition for back decay will thus result in fusions occurring for only some fraction of the $dd\mu$ molecules. Usually the fusion will release the muon to join the system again (see Figure 1.8).

In contrast to the μCF cycle in pure deuterium, however, a single muon is extremely unlikely to catalyze more than one fusion in this medium because of the scavenging by carbon. The search for μCF in a deuterocarbon system is therefore not of interest from the point of view of energy release, but merely as an investigation into the possibility of a mechanism allowing $dd\mu$ formation at an enhanced rate in a solid environment.

The motivation for this work thus arose from the question of whether a deuterated organic crystal could provide an environment in which μCF would occur.

In the following chapters, the course of this investigation will proceed through three stages. Chapter 2 describes a test experiment to determine the feasibility of producing muons at a locally available cyclotron. In Chapter 3, two phases of the search for μCF in deuterated anthracene are presented. Each phase consists of an experiment in which deuterated and natural anthracene crystals were placed in the muon 'beam' produced at the cyclotron. The second phase made use of an improved experimental setup resulting from the experience gained in the Phase 1 experiment.

The thesis is concluded in Chapter 4, in which suggestions for further work are also made.

Chapter 2

Muon production at NAC

2.1 Making muons

In nature pions are produced when protons of cosmic origin collide with light nuclei in the upper atmosphere. Free positive and negative pions then decay (with lifetimes of 26 ns[1]) into muons via the processes $\pi^+ \rightarrow \mu^+ + \nu_\mu$ and $\pi^- \rightarrow \mu^- + \bar{\nu}_\mu$.

Meson factories around the world (e.g. TRIUMF, LAMPF, ISIS, PSI) mimic the natural π-producing nucleon-nucleon collisions in order to produce beams of muons for use in nuclear and particle physics experiments.

It can be shown using relativistic kinematics (see Appendix A) that the threshold energy required for pion production from a proton incident on a free stationary nucleon is given by

$$m_\pi c^2 \left(2 + \frac{m_\pi}{2m_N}\right) = 290 \text{ MeV}$$

(using $m_\pi c^2 = 140$ MeV and $m_N c^2 = 939$ MeV).

However in reality the Fermi motion of nucleons inside the nuclei of a stationary target gives some of the nucleons momenta with components antiparallel to the incident proton beam [Mc 47, Lo 82]. This has the effect of increasing the centre-of-mass energy in a collision involving an accelerated proton and such a nucleon, and the minimum proton energy required for pion production is thus reduced to around 140 MeV [Ma 79, Cl 82, Lo 82].

The variable-energy separated-sector cyclotron at the National Accelerator Centre (NAC) in Faure, near Cape Town, is capable of accelerating protons up to 225 MeV. Sub-threshold pion production should therefore be possible at this facility. A test experiment at the NAC to measure the muon yield from 200 MeV protons on ^{nat}Pb was planned for April 1991, the intention being to assess the feasibility of using such muons in a search for μCF in deuterated anthracene.

[1]This lifetime may seem rather long for a strongly interacting particle such as the pion. However since the pion is the lightest meson it cannot decay strongly and is forced to do so via the weak interaction instead, hence its nanosecond existence.

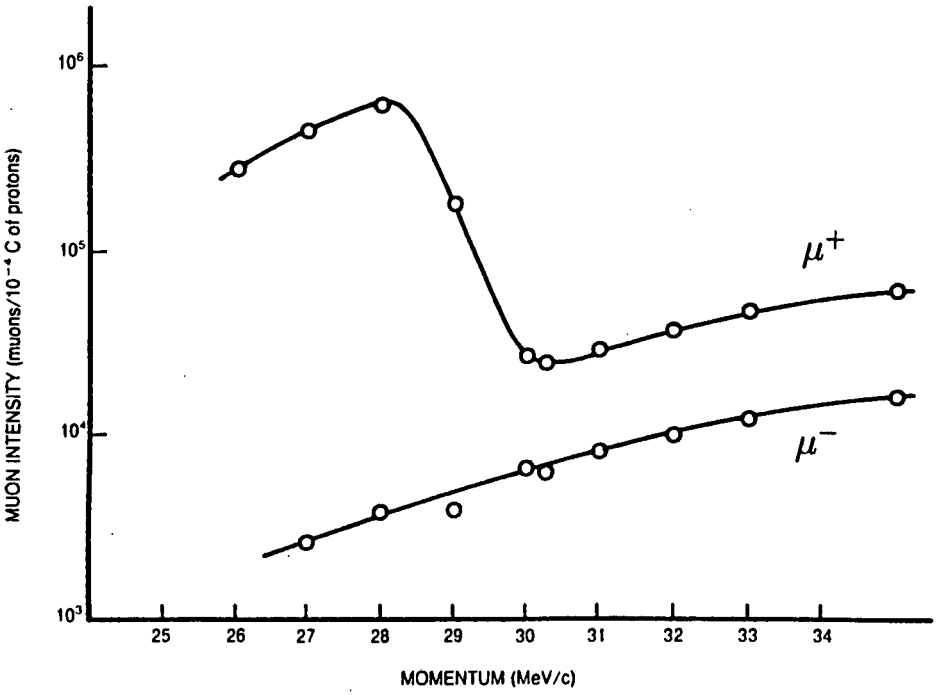

Figure 2.1: Intensities of μ^+ and μ^- as a function of momentum from high energy protons incident on a beryllium target at PSI. For μ^+ the surface muon peak appears at momenta less than 30 MeV/c, while there is no corresponding peak for μ^- because of π^- capture by nuclei. These intensities are typical for any 0.6–1.0 GeV proton accelerator. From [Bo 85].

2.1.1 Surface, cloud and decay muons

Muon production from pion decay can be classified into three categories according to the position and momentum of the pion when it decays. Muons from these three classes of pion decay are referred to as '*surface*, '*decay*' and '*cloud*' muons respectively.

'*Surface*' muons arise from the decay of pions brought to rest close to the surface of the pion production target. Since the π-μ decay has a two-body final state, a pion decaying always produces a muon with a kinetic energy of 4.1 MeV and a momentum of 30 MeV/c in its own rest frame. Surface muons therefore emerge from the target with laboratory energies less than or equal to 4.1 MeV, depending on how close to the surface of the accelerator beam target the pion decays. The surface mechanism is strong for π^+ because coulomb repulsion inhibits π^+ capture by nuclei as the pion comes to rest. For π^- the opposite is true; π^- coming to rest in the production target are scavenged by nuclear interactions before they can decay. Figure 2.1 shows μ^+ and μ^- intensities as a function of momentum, with the surface muon peak at momenta less than 30 MeV/c for μ^+.

A common method of muon beam production, employed at meson facilities worldwide and requiring a proton beam energy of 0.5 to 1.0 GeV, is to collect pions electromagnetically from the primary production target, and allow them to coast through a decay region before selecting muons of the desired momenta. The muons thus arise from pions decaying in flight, and so are dubbed '*decay*' muons.

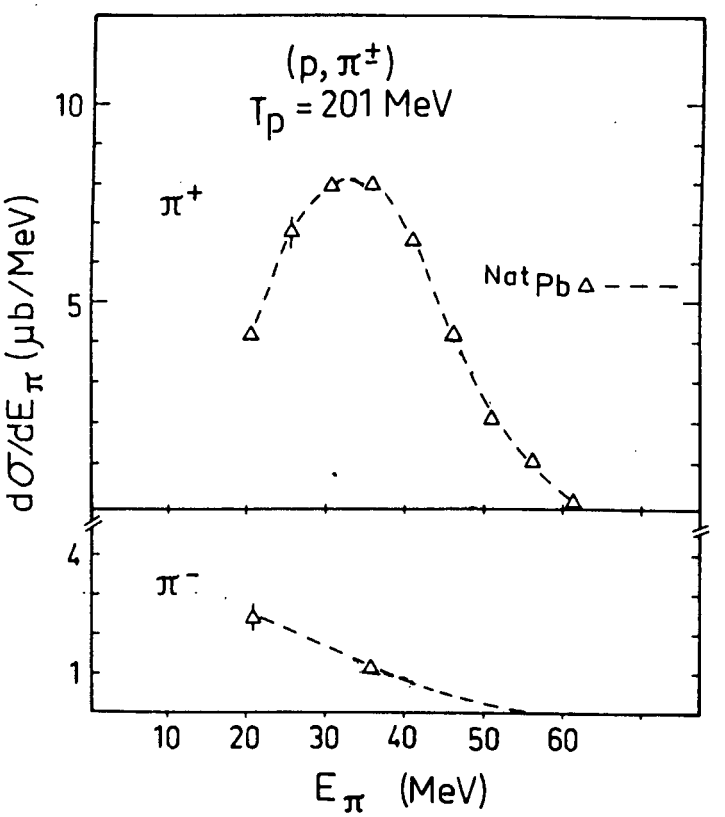

Figure 2.2: Pion energy dependence of the angle-integrated charged pion production in (p,$\pi^{\pm}$) from 201 MeV protons on ^{nat}Pb. From [Bi 85].

See for example [Th 79], which describes the stopped muon channel at LAMPF.

The category intermediate between surface and decay muons is that of '*cloud*' muons. These are muons whose precursors are pions which creep out of the production target with small kinetic energies, emerging so slowly that they form a decaying 'cloud' close to its surface.

2.1.2 Sub-threshold muon production

Prior to the commencement of the muon production test experiment at the NAC, calculations were performed to provide an order-of-magnitude estimate of the expected muon yield. The calculations were based on the published cross-section data of Bimbot *et al.* [Bi 85] for (p,$\pi^{\pm}$) reactions at E_p = 201 MeV. The work was carried out at the Orsay Synchrocyclotron in France, where beams of two incident energies (201 and 180 MeV) were used to induce charged pion production on ^{12}C, ^{89}Y and ^{nat}Pb. Of particular interest were the results from 201 MeV protons on ^{nat}Pb, since the proposal for the test experiment at the NAC was to direct 200 MeV protons onto natural lead.

Using a ^{nat}Pb target 130 mg/cm^2 (or 115 μm) thick and tilted at 45° to the incident beam, Bimbot *et al.* measured the double differential cross section $\left(\frac{d^2\sigma}{d\Omega\ dE_\pi}\right)$. The energy dependence ($d\sigma/dE_\pi$) for π^+ and π^- (Figure 2.2) was then estimated by extrapolating these measurements and integrating over the solid angle, while

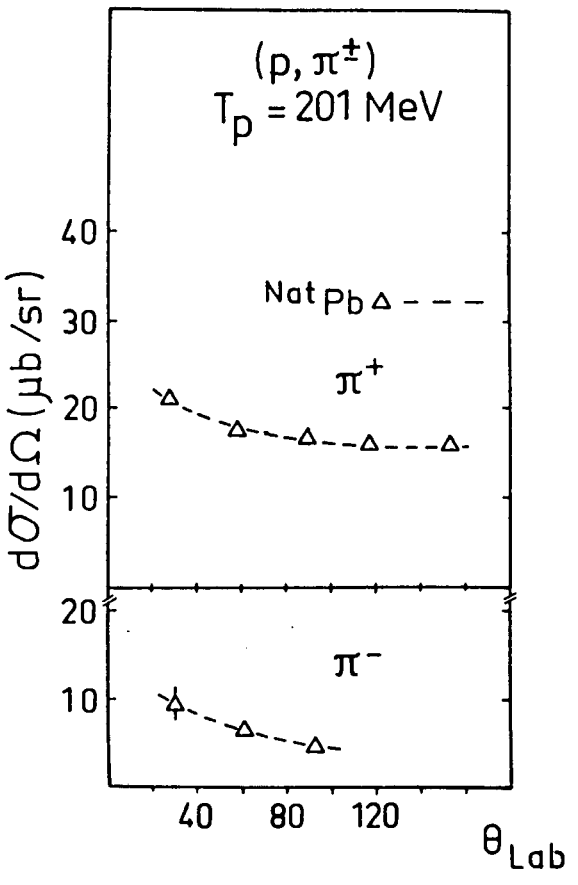

Figure 2.3: Angular distributions of the energy-summed charged pion production in (p,$\pi^{\pm}$) from 201 MeV protons on ^{nat}Pb. From [Bi 85].

integrating over the pion energy gave the angular distributions ($d\sigma/d\Omega$) shown in Figure 2.3. This figure shows the angular distribution to be more isotropic for π^+ than for π^- (for π^+ the ratio of ($d\sigma/d\Omega$) at 30° to that at 151° is 1.4, while for π^- the ratio of ($d\sigma/d\Omega$) at 30° to that at 90° is 2.0). For the purposes of an order-of-magnitude calculation these angular distributions for π^+ and π^- can be taken as isotropic.

Figure 2.4 shows the layout of the NAC in Faure. A muon flight pipe roughly 8 m in length and 10 cm in diameter was constructed, leading out from the N-line target chamber at 90° to the direction of the incident proton beam (this configuration was chosen so that muon test experiments could be performed parasitically while the proton beam was dedicated to other projects on the N-line). The geometry of this muon flight pipe should favour the arrival of cloud and surface muons rather than decay muons at the downstream end, since a large fraction of the higher energy pions entering the pipe will be absorbed in its walls, and there is an additional solid angle factor from the angular distribution of the decay muons, making it extremely unlikely for them to go into the solid angle subtended by the flight pipe. Since pions will be produced at a variety of depths within the target, a range of initial pion energies from zero to that of a pion whose range is the thickness of the target will lead to the emergence of surface muons, or pions suitable for decaying into cloud muons, into the hemisphere on the side of the target facing the muon flight pipe. For example, a 9.5 MeV pion has a range in lead of 1.0 mm. Pions of up to 9.5 MeV will therefore contribute to the surface muons (positive) and cloud pions (positive

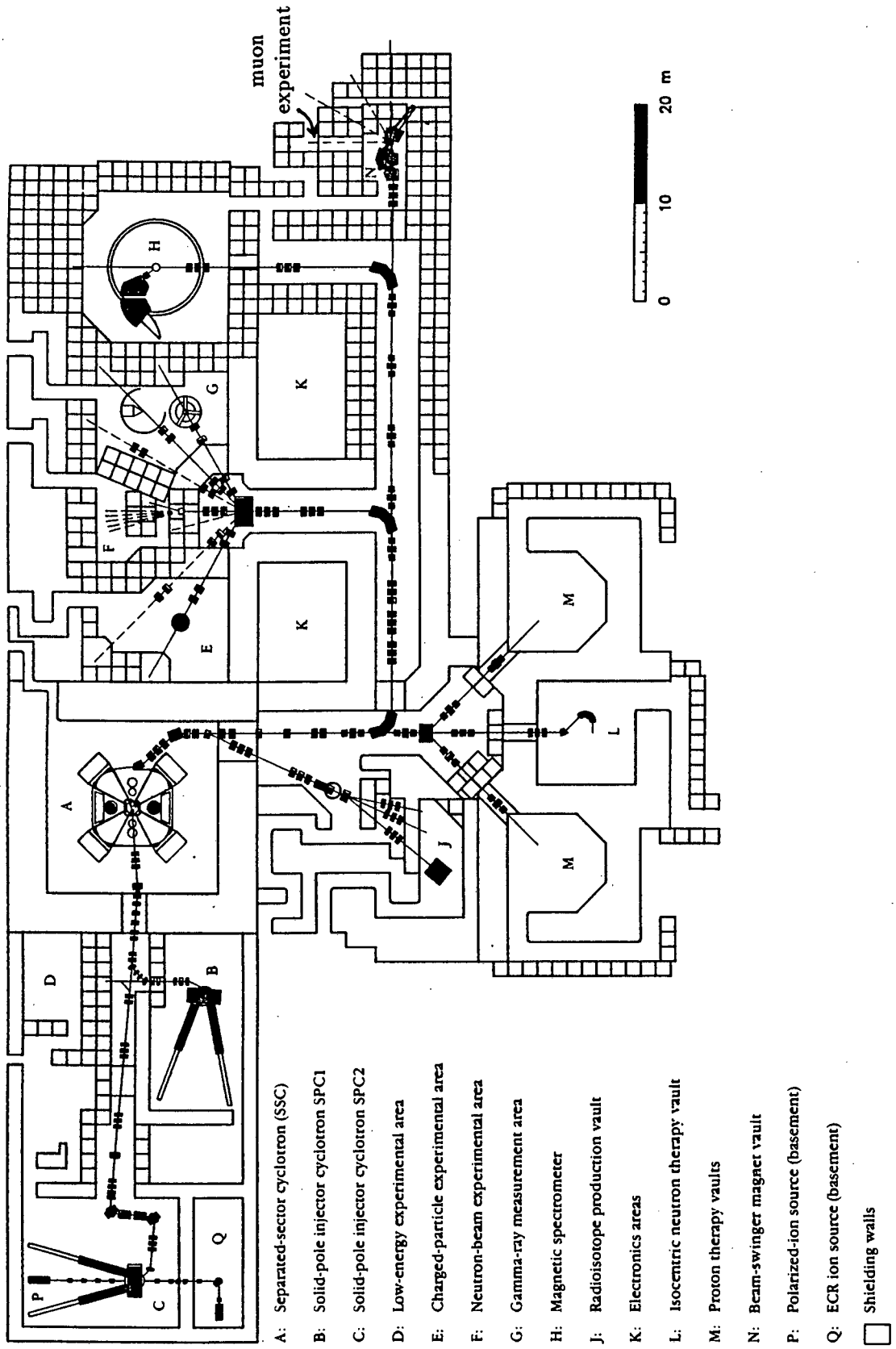

Figure 2.4: Layout of the National Accelerator Centre, showing the position of the muon flight pipe perpendicular to line N.

and negative) emitted on one side of a 1 mm thick lead target.

The expected muon production rate from 200 MeV protons on 1 mm of ^{nat}Pb can be calculated as follows:

$$\left(\frac{dN_\mu}{dt}\right)_T = \frac{dN_0}{dt}\, n \left(\frac{1}{2}\right) \int_0^{9.5} \frac{d\sigma}{dE_\pi} dE_\pi \ ,$$

where $\frac{dN_\mu}{dt}$ is the number per second of surface muons and low (close to zero) energy cloud pions emitted into the 2π solid angle in view of the muon flight pipe; $\frac{dN_0}{dt}$ is the number per second of 200 MeV protons delivered onto the 1 mm thick lead target; and n is the number of nuclei per barn 'seen' by the proton beam i.e. n is the thickness of lead (1.13×10^{-24} g b^{-1}) divided by the atomic weight of lead (207 amu, with 1 amu = 1.67×10^{-24} g). If the pion energy dependent (p,$\pi^\pm$) cross sections at E_p = 200 MeV are assumed, with the aid of Figure 2.2, to be a constant 2.0 μb MeV^{-1} over a range of pion energies from 0.0 to 9.5 MeV, then, for a beam current of 200 nA,

$$\begin{aligned}
&\left(\frac{dN_\mu}{dt}\right)_T \\
&\quad = \left(\frac{200 \times 10^{-9} A}{1.6 \times 10^{-19} C}\right) \left(\frac{1.13 \times 10^{-24} \text{ g b}^{-1}}{207 \times 1.67 \times 10^{-24} \text{ g}}\right) \left(\frac{1}{2}\right) (2.0\ \mu\text{b MeV}^{-1})\,(9.5 \text{ MeV}) \\
&\quad = 3.9 \times 10^4 \text{ s}^{-1} \ .
\end{aligned}$$

The number of muons per cm^2 per second expected at a distance of 8 m from the target is then obtained by multiplying $\left(\frac{dN_\pi}{dt}\right)_T$ by the appropriate solid angle factor. Thus for a target area of 1 cm^2 at a distance of 8 metres

$$\left(\frac{dN_\mu}{dt}\right)_C = \left(\frac{dN_\pi}{dt}\right)_T \times \left(\frac{1 \text{ cm}^2}{2\pi\ 800^2 \text{ cm}^2}\right) = 0.010 \text{ s}^{-1} = 0.60 \text{ min}^{-1} \ .$$

For the purposes of μCF experiments the flux of negative muons is of interest. If the cross section for π^+ production is estimated, using Figure 2.2 at E_π = 20 MeV, to be twice that for π^- production from 200 MeV protons on ^{nat}Pb, and further, if the surface muon enhancement for μ^+ production is, at most, a factor of 20 (see Figure 2.1), then the ratio of μ^- to μ^+ production is given by (0.5)(0.05) = 0.025. The negative muon flux at the catcher can then be estimated as $\frac{0.025}{1+0.025}$ of the total muon flux, i.e.

$$\begin{aligned}
\frac{dN_{\mu^-}}{dt} &= 0.024 \times 0.60 \text{ cm}^{-2} \text{ min}^{-1} \\
&= 0.014 \text{ cm}^{-2} \text{ min}^{-1} \ .
\end{aligned}$$

In general this very low intensity would make it unthinkable to conduct muon experiments at this facility. It was thought, however, to be sufficient for attempting an experiment in which every muon would be absorbed in the target, and in which the target itself could provide a 4π detection system for fusion reaction products.

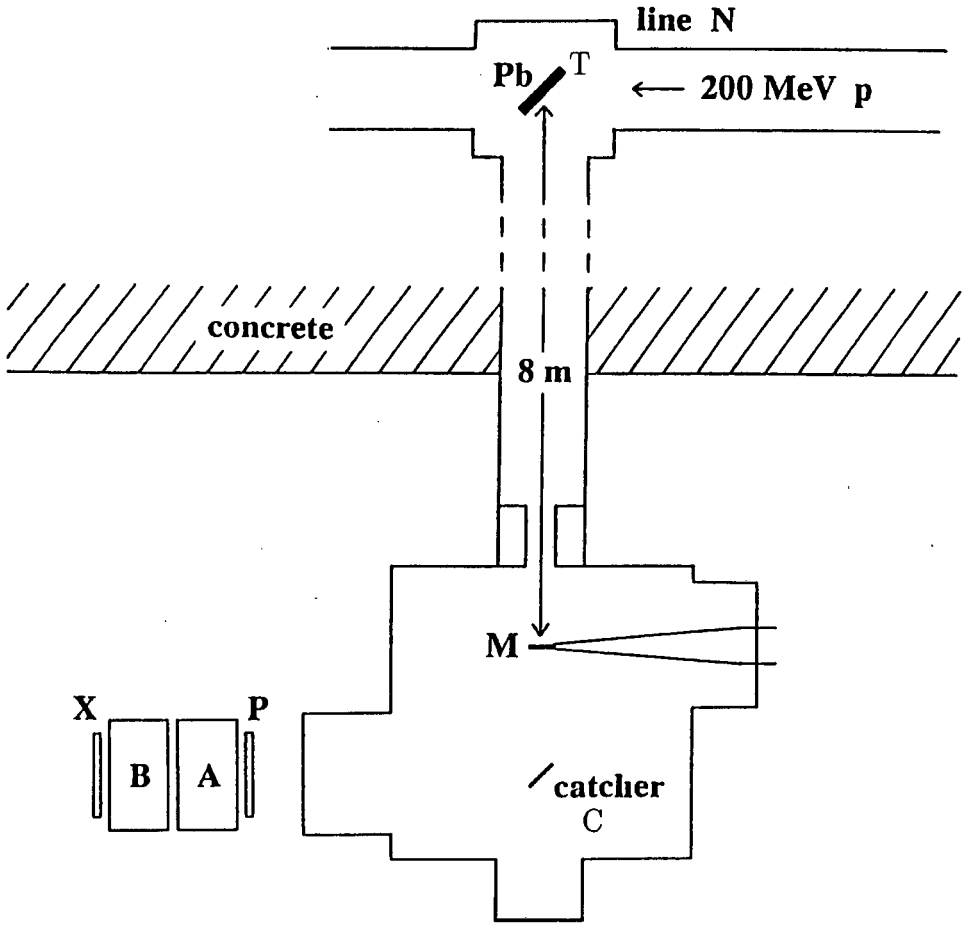

Figure 2.5: Schematic representation of the detector setup used in the muon production test experiment at the NAC. The detector marked X is referred to later in the text.

2.2 The experiment at NAC

2.2.1 Arrangement of target and detectors with reference to expected muon signatures

The system of detectors and its position relative to the target are depicted in Figure 2.5. Natural lead was used for the pion production target T, which was oriented at 30° to the 200 MeV pulsed incident proton beam. Perpendicular to the beam was an evacuated pipe 8 metres long which connected the target chamber to a chamber containing a thin plastic scintillator M (0.25 mm NE102A) and an aluminium 'catcher' C. A three-detector telescope comprising a plastic scintillator P (3 mm thick, 126 mm diameter NE102A), and two liquid scintillators A and B (each $13 \times 13 \times 7$ cm^3 NE213), was situated outside the catcher chamber. The construction of the liquid scintillators, referred to collectively as the 'K detectors', is described in Appendix B. The detector labelled X is mentioned later in the text.

This system was designed to look for evidence, from amongst an expected abundance of spallation particles, of positive or negative muons produced at T and which travel in the direction TC. One 'signature' of the muon is based on the time-of-flight from T to the thin scintillator M. Another is the detection and identification of electrons or positrons, in the telescope, from the decay of muons brought to rest in the

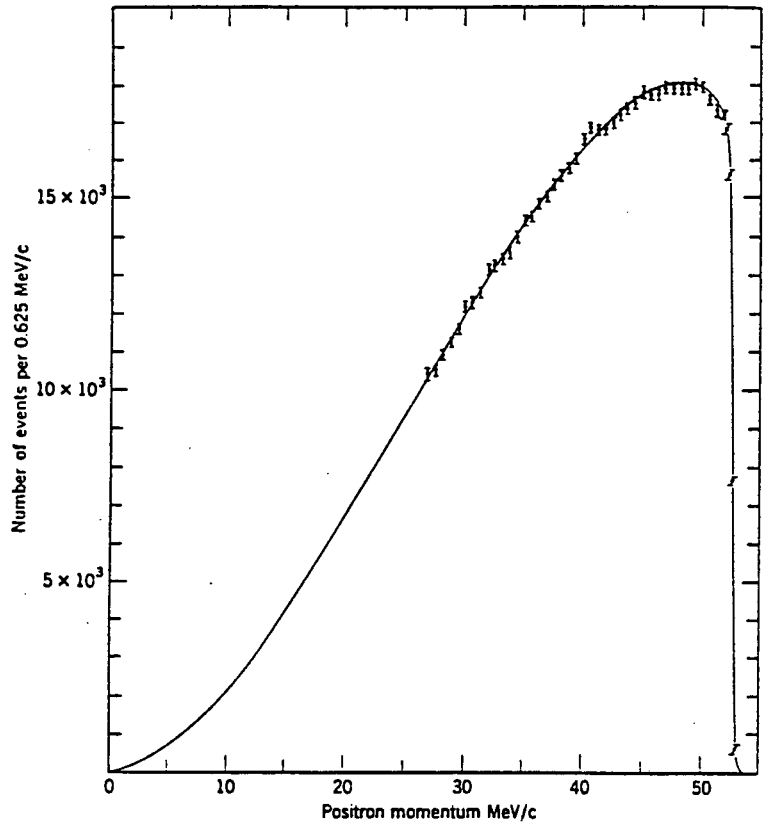

Figure 2.6: Experimental spectrum of positrons from μ^+ decay. The solid line is the theoretically predicted spectrum. From [Ba 65].

catcher C. A third possible signature is a combination of the first two, viz. a delayed coincidence between M and the telescope, indicating the arrival of the muon at C followed by the detection of its decay electron or positron (within the characteristic μ^+ or μ^- lifetime). A variety of backgrounds could mask or mimic these signatures to some extent. For example, scattered protons or other charged particles which heavily outnumber the muons reaching M could dominate the time-of-flight spectrum, and cosmic muons could trigger the telescope in like manner to electrons or positrons.

The choice of telescope detectors, and their geometry, was governed by the momentum spectrum of positrons (or electrons) from μ^+ (or μ^-) decay, which is shown in Figure 2.6. An electron or positron having the maximum momentum of 53 MeV/c, corresponding to a kinetic energy of 52 MeV, would be brought to rest in the second liquid scintillator B. Pulse shape discrimination (see Appendix C) was used for particle identification in the two liquids. The event requirement was a PAB coincidence.

2.2.2 Electronics

The ten parameters recorded for each event were the following:

L_A, the pulse height in detector A;

F_A, the fast component of L_A;

L_B, the pulse height in detector B;

Bit	Input	Value
0	γ_A	1
1	γ_B	2
2	$n\gamma_A$	4
3	$n\gamma_B$	8
4	AB	16
5	AP	32
6	W_E	64

Table 2.1: Pattern register inputs. An explanation of the symbols used appears in the text.

F_B, the fast component of L_B;
L_P, the pulse height in detector P;
L_M, the pulse height in detector M;
T_M, the time-of-flight over the distance TM;
T_A, the time between the proton beam pulse and a signal in A;
T_E, the time between signals in M and A;
R, the pattern register value.

Figure 2.7 is a simplified block diagram representing the salient features of the electronic system used in the experiment. The anode signals from detectors A and B were fed into their respective LINK 5010 pulse shape discrimination (PSD) units. Each of these gives pulse heights L and F, a fast timing output and three particle identification outputs: one (γ) signifying gamma events[2] only, another (n) for selecting neutron events only, and a third ($n\gamma$) marking an event as either a neutron or a gamma. The particle identification process is outlined in Appendix C.

The pulse height signals L_M and L_P were taken from the dynode outputs of the photomultipliers coupled to detectors M and P, while the anode outputs were used in the coincidence logic. The anode output of M was also used to start the T_M and T_E TACs. The γ_A output of LINK A provided the STOP for T_E and the START for T_A. Both T_A and T_M were stopped by the pulse selector radio frequency (PSRF) of the cyclotron. Each of the three TACs was operating on a range of 500 ns.

The function of the coincidence logic was to provide an event gate under the required condition of a fast PAB coincidence, and to provide inputs for a pattern register (not shown in Figure 2.7 for simplicity).

The pattern register was used to tag events so that more stringent requirements could be placed on the data during the off-line analysis. Table 2.1 shows the pattern register inputs in detail. The symbols γ and $n\gamma$ with the appropriate subscripts indicate the outputs of the respective LINK 5010 units controlling the PSD on detectors A and B. AB and AP represent fast coincidences, and W_E implies a slow

[2]Here, and elsewhere in this work, gamma events should be taken to mean gamma rays *or* electrons in the context of PSD, since gamma rays are identified through the detection of the Compton electrons they produce in the scintillator.

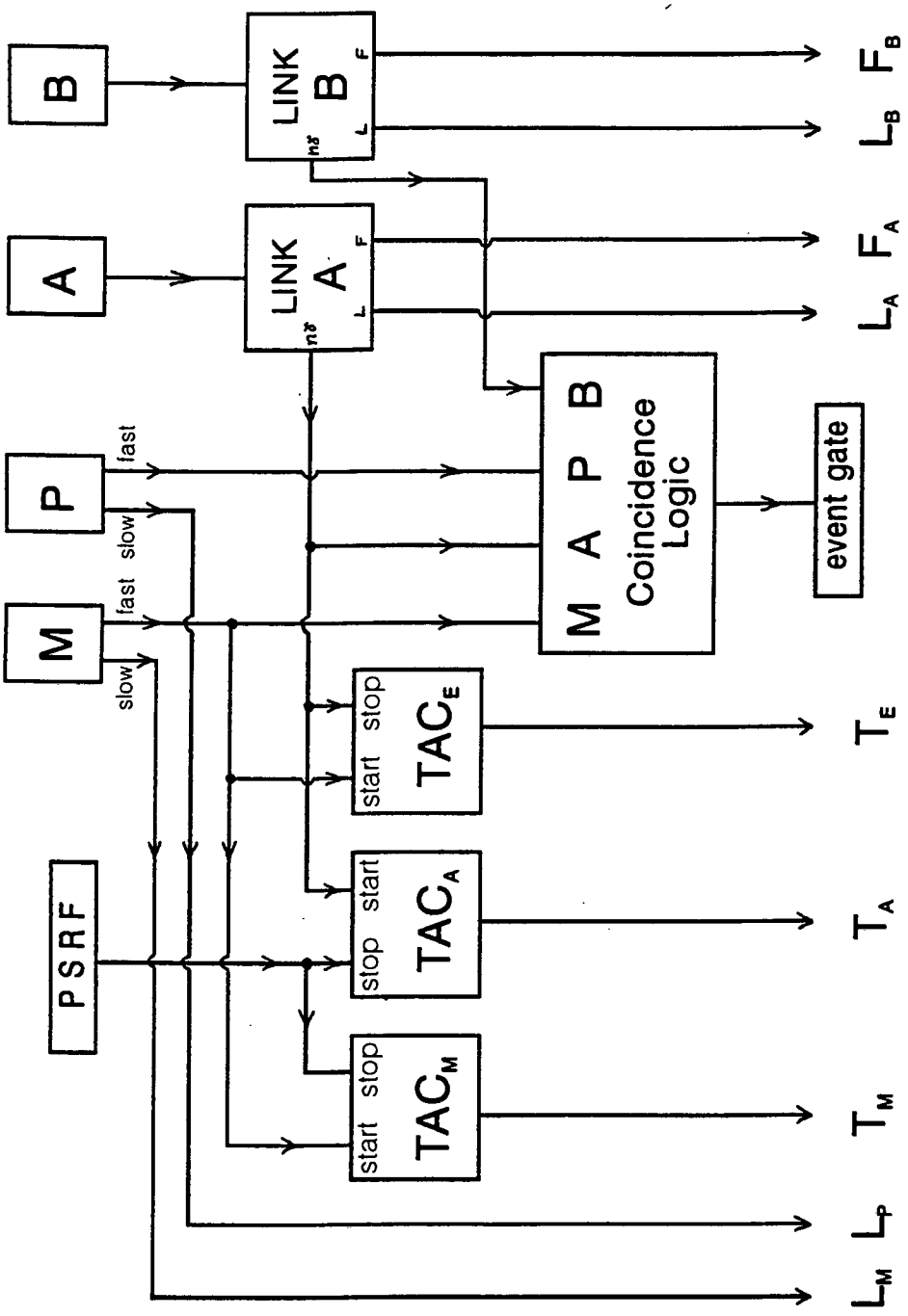

Figure 2.7: Simplified block diagram of the electronics used in the muon production test experiment.

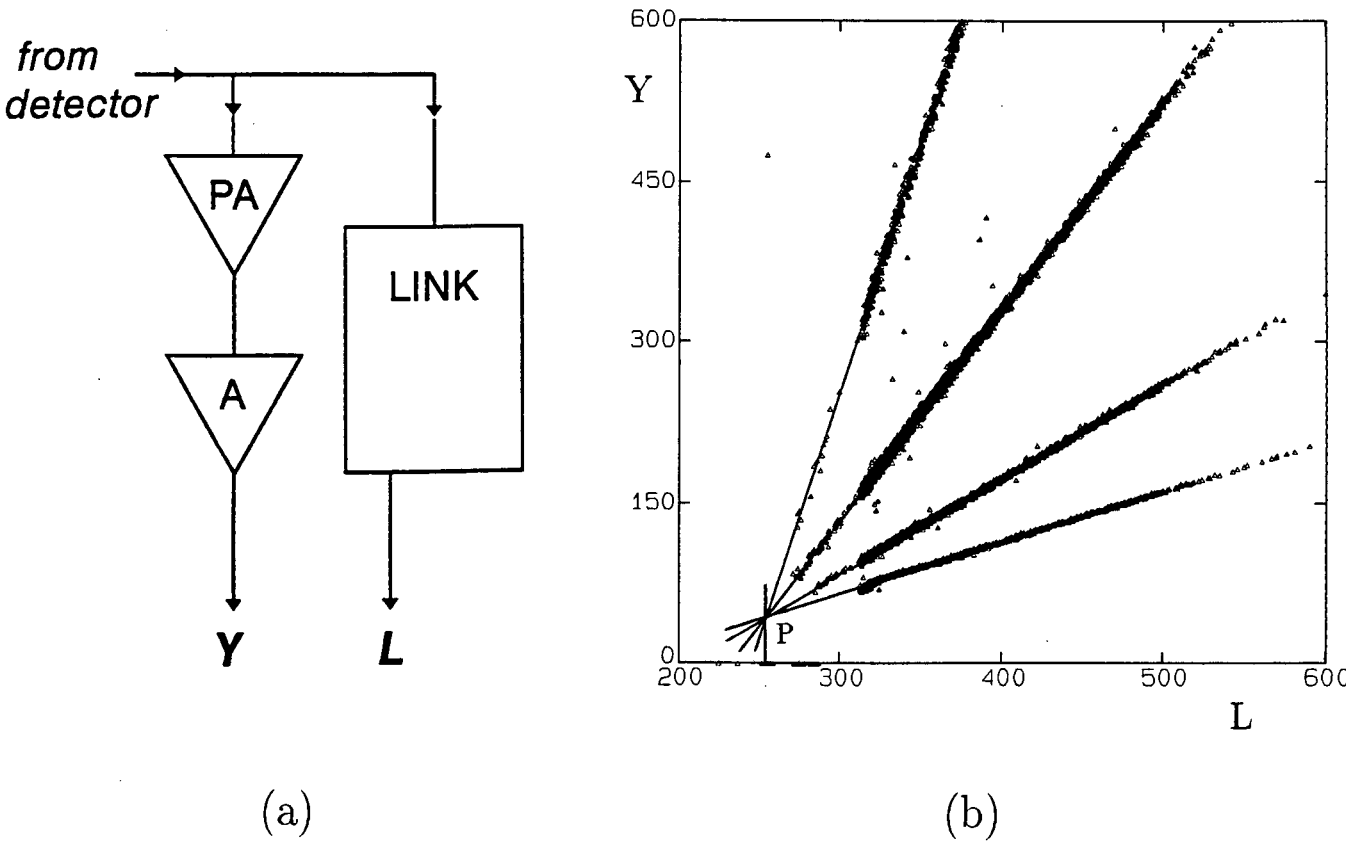

Figure 2.8: (a) System used to determine true zero pulse height L from LINK pulse shape discriminators; and (b) loci of Y vs L measured for detector A using different amplifier gains. The point P shows the true zero of L_A to be at channel 252.

coincidence between M and A by indicating a signal in the T_E TAC.

2.3 Calibrations

2.3.1 Pulse height to energy calibrations

The calibration of pulse heights L from the NE213 detectors A and B in units of MeV-electron-equivalent (MeVee) involved two steps: (i) determining the true zero of the L scale; (ii) recording the L spectrum for Compton electrons ejected in the NE213 by gamma rays from an Am-Be source. The true zero was determined for each detector in turn using the system shown in Figure 2.8(a), in which the detector signal to the LINK was (temporarily) fed in parallel to a preamp-amplifier system, and the resulting linearly-correlated outputs L and Y from the same signal were plotted against one another as shown in Figure 2.8(b). For a given amplifier gain this leads to a linear plot of Y against L, and the loci from a set of plots at different gains all pivot about the point P whose coordinates correspond to the true zeroes of L and Y. The L_A and L_B true zeroes were thus determined to be at ADC channels 252 and 310 respectively. The electron spectrum from detector A, recorded

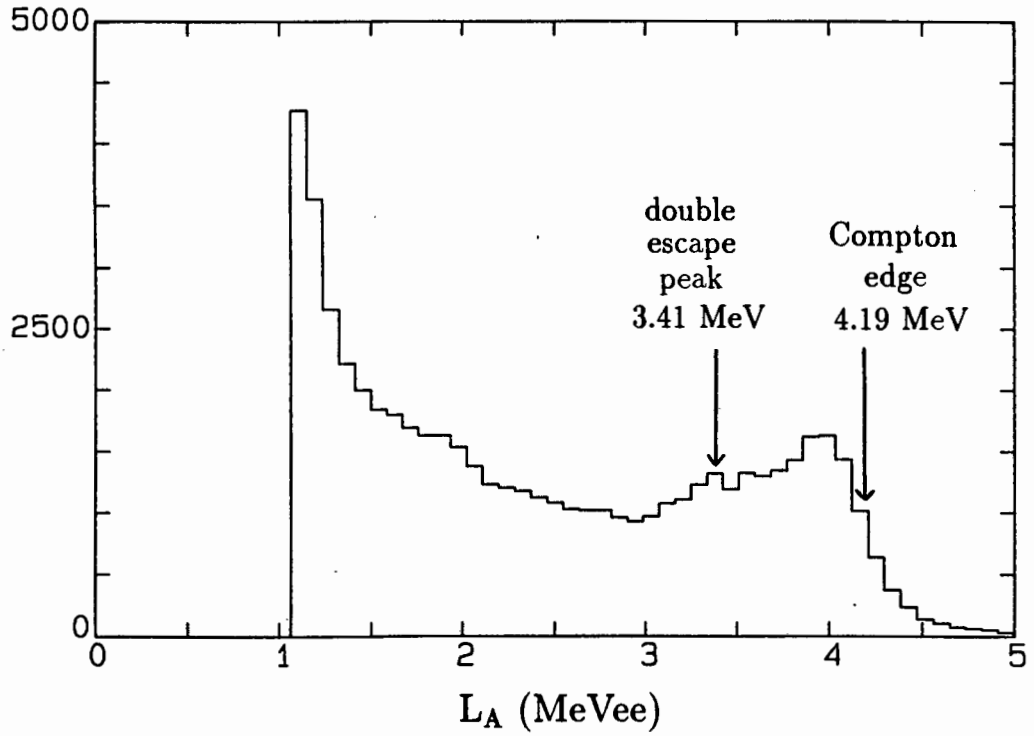

Figure 2.9: Pulse height calibration spectrum measured by detector A using PSD to select electrons released in interactions of gammas from an Am-Be source.

using the Am-Be source, appears in Figure 2.9. It shows an edge corresponding to the maximum Compton electron energy of 4.19 MeV, and a double-escape peak at 3.41 MeV, both of which are associated with the 4.43 MeV gamma ray from this source. The pulse height spectrum of Figure 2.9 was calibrated on these points after correcting for the true zero. The L_B spectrum was calibrated in a similar fashion.

2.3.2 Time calibrations

The scales of the three time parameters T_M, T_A and T_E were calibrated simultaneously as follows: with the Am-Be source providing signals in detectors A and B, either of the two LINK γ outputs was used to start the T_M, T_A and T_E TACs. All three TACs were self-stopped by their start signals, which were subsequently delayed by 40 ns for each of T_M and T_A, and by 200 ns in the case of T_E. This procedure gave rise to two sharp spikes separated by the amount of the delay in each time calibration spectrum, thus facilitating the conversions from channel number to time in each case.

2.4 Results and discussion

Figure 2.10 shows counts versus pulse shape S and pulse height L from detector A for all accepted events (i.e. PAB coincidences). The proton and electron loci are clearly separated on this plot. The prominent peak at L_A=13 MeV is attributed to muon decay electrons (or positrons), and to cosmic muons, which were not excluded by

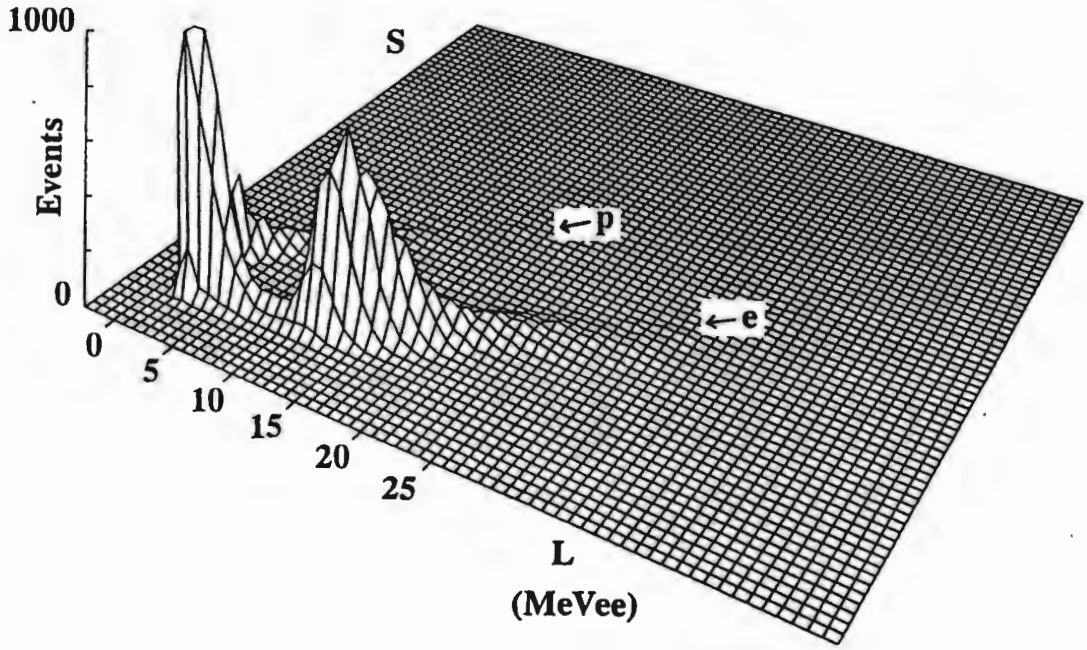

Figure 2.10: Counts versus pulse shape S and pulse height L from detector A (for PAB coincidences).

the PAB coincidence requirement. According to Figure 2.11, the minimum ionizing specific energy loss of electrons is 2 MeV g^{-1} cm^2. This occurs at 1.5 MeV electron energy, with dE/dx rising slowly to around 2.5 MeV g^{-1} cm^2 at higher energies. Muon decay electrons traversing 7 cm of NE213, which has a density of 0.874 g cm^{-3}, are therefore expected to deposit between 12 and 15 MeV in the liquid. Most cosmic muons are also minimum ionizing particles, however, and so are indistinguishable from electrons on this plot.

A similar LS plot can be obtained for detector B, and is shown in Figure 2.12. The peak in the L_B spectrum is not as prominent as that obtained in detector A,

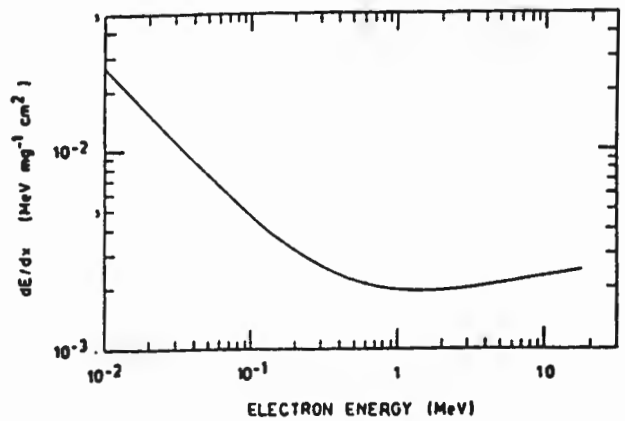

Figure 2.11: dE/dx for electrons.

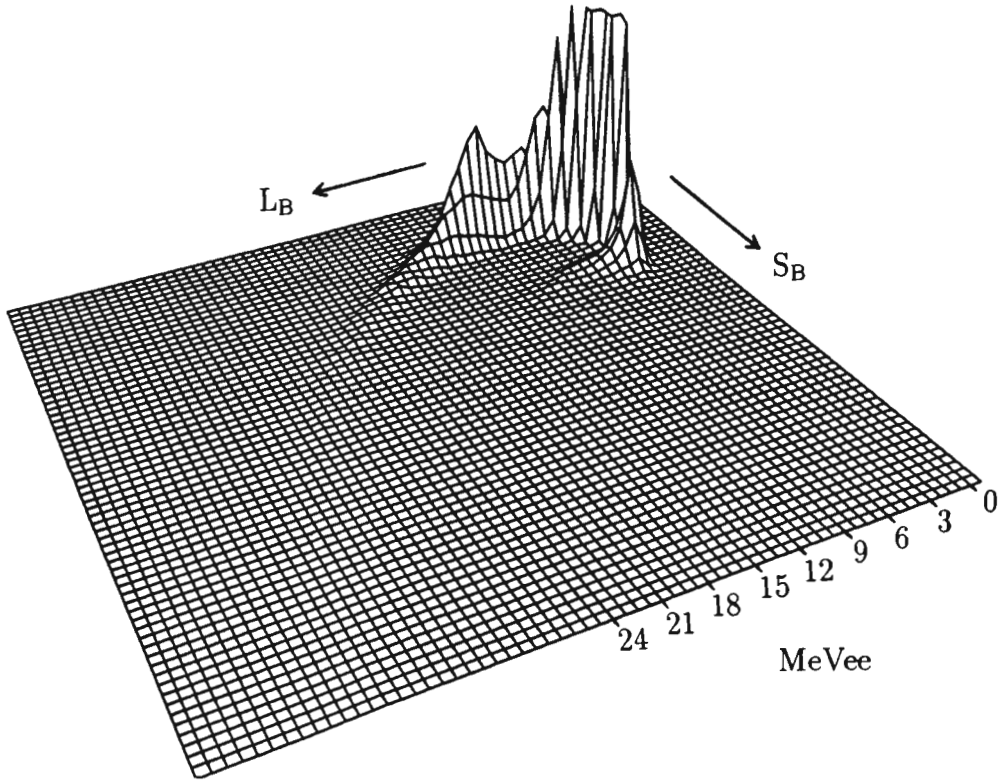

Figure 2.12: Counts versus pulse shape S and pulse height L from detector B (PAB coincidences).

and occurs at a slightly lower pulse height of 12 MeV (this is more easily observed in later figures). This is because the event requirement PAB is satisfied by muon decay electrons stopping in B, or crossing the edges of the detector, after traversing P and A. There is thus a higher proportion of low-energy pulses in B than in A.

2.4.1 Selecting muon decay electron events

The LS displays of Figures 2.10 and 2.12 contain all PAB coincidences. A number of cuts can be applied to these data to exclude events which could not be interpreted as possible muon decay electrons. The rejected events would include those made by scattered protons, neutrons or gamma rays that had penetrated the telescope in such a way as to satisfy the event requirement. The most obvious cuts to apply are those selecting events which lie only on the electron loci of Figures 2.10 and 2.12. These will be referred to as LS_γ^A and LS_γ^B cuts respectively. Next, a restriction can be placed on the pulse height L_A so as to retain only those events lying in the 'decay electron' peak i.e. L_A would be between 9 and 20 MeV. In addition to these cuts the event reqirement can be tightened by using the pattern register values to select events in which the PAB signal occurred in delayed coincidence with a signal in detector M, the idea being that a muon passing through M is brought to rest on the catcher, and the signal of its decay electron in the telescope is seen a time of the order of the muon lifetime after the signal in M. This coincidence of M with PAB occurs for a pattern register value of R=127, since bits 0 to 3 fire if electrons are

seen in both A and B, bits 4 and 5 register the PAB coincidence, and bit 6 is set if the event is inside the T_E TAC window W_E (refer to Table 2.1).

2.4.2 Spectra

Figure 2.13 shows density plots of S_A vs L_A and S_B vs L_B for all PAB events collected during the beam runs (i.e. the data presented in Figures 2.10 and 2.12), indicating the positions of the pulse shape cuts LS_γ^A and LS_γ^B. The L_A and L_B spectra obtained from those events satisfying both pulse shape cuts are shown in Figure 2.14. Figures 2.15 and 2.16 display the corresponding density plots and pulse height spectra for data obtained with the beam off (the total 'beam on' run time was greater than the 'beam off' run time by a factor of 1.7). Clearly cosmic muons form a substantial portion of the background to the beam measurements. The number of events collected during the 'beam on' runs which could be attributable to accelerator-produced muons was therefore estimated as follows. The L_A and L_B spectra were divided into regions labelled 1 and 2 as shown in Figure 2.17. Various types of event are represented schematically in the same figure, with the notation A_mB_n being used to denote an event which produced pulse heights in the mth and nth regions of L_A and L_B respectively. Figures 2.18 and 2.19 show the positions of these different types of event on scatter plots of L_B vs L_A for beam on and beam off conditions respectively. Also shown are the corresponding three dimensional versions of the scatter plots. Muon decay electrons are expected to be chiefly events of type A_2B_1, which pass through detector A, coming to rest or traversing only short distances in detector B. Type A_2B_2 events are almost certain to be cosmic muons, which would penetrate detectors A and B easily, leaving relatively high pulse heights in each.

Assuming A_2B_2 events to be *all* cosmic muons, the 'beam on' and 'beam off' runs can be normalised in this region, thus facilitating a comparison of the A_2B_1 events in each data set. Suppose that C_I and C_O represent the numbers of A_2B_2 events for beam ON and beam OFF conditions respectively, and that the symbols N_I and N_O do likewise for the A_2B_1 events (see Table 2.2). The number of muon decay electrons N_e from accelerator-produced muons is then given by

$$N_e = N_I - \left(\frac{C_I}{C_O}\right) N_O \ .$$

Inserting the figures displayed in Table 2.2 this becomes

$$\begin{aligned} N_e &= 7880 - \left(\frac{6203}{3589}\right) 4413 \\ &= (7880 - 7626) \pm \sqrt{7880 + 7626} \\ &= 254 \pm 125 \ . \end{aligned}$$

The muon flux at the catcher can then be estimated from

$$\frac{dN_\mu}{dt} = \frac{dN_e}{dt} \left(d\Omega_B\right) ,$$

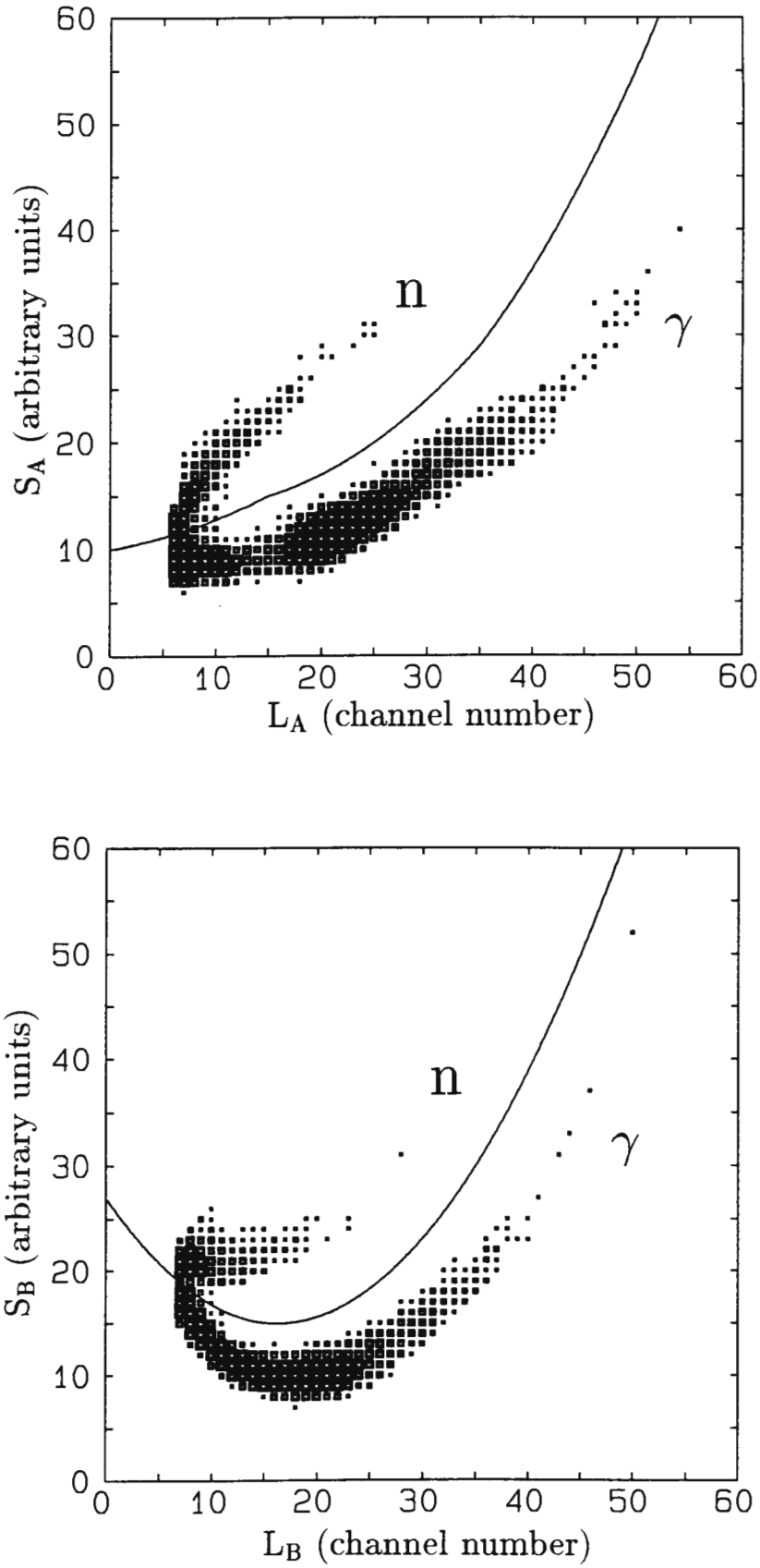

Figure 2.13: Pulse shape S vs pulse height L for detectors A (top) and B (all PAB events, beam ON). The points in order of increasing size represent count thresholds of 5, 10, 20, 50 and 100 respectively.

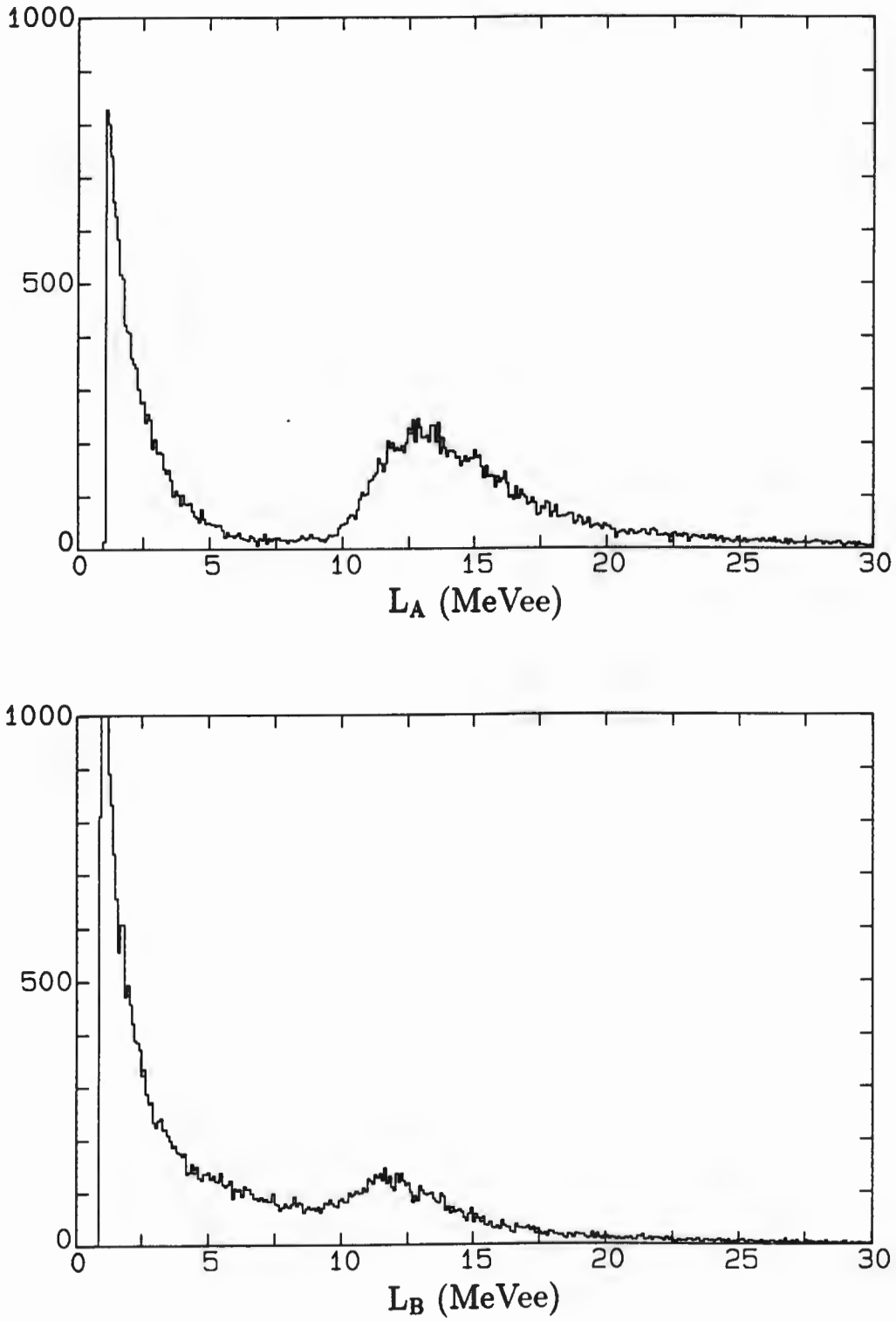

Figure 2.14: L_A (top) and L_B spectra for events satisfying both pulse shape cuts LS_γ^A and LS_γ^B (beam ON).

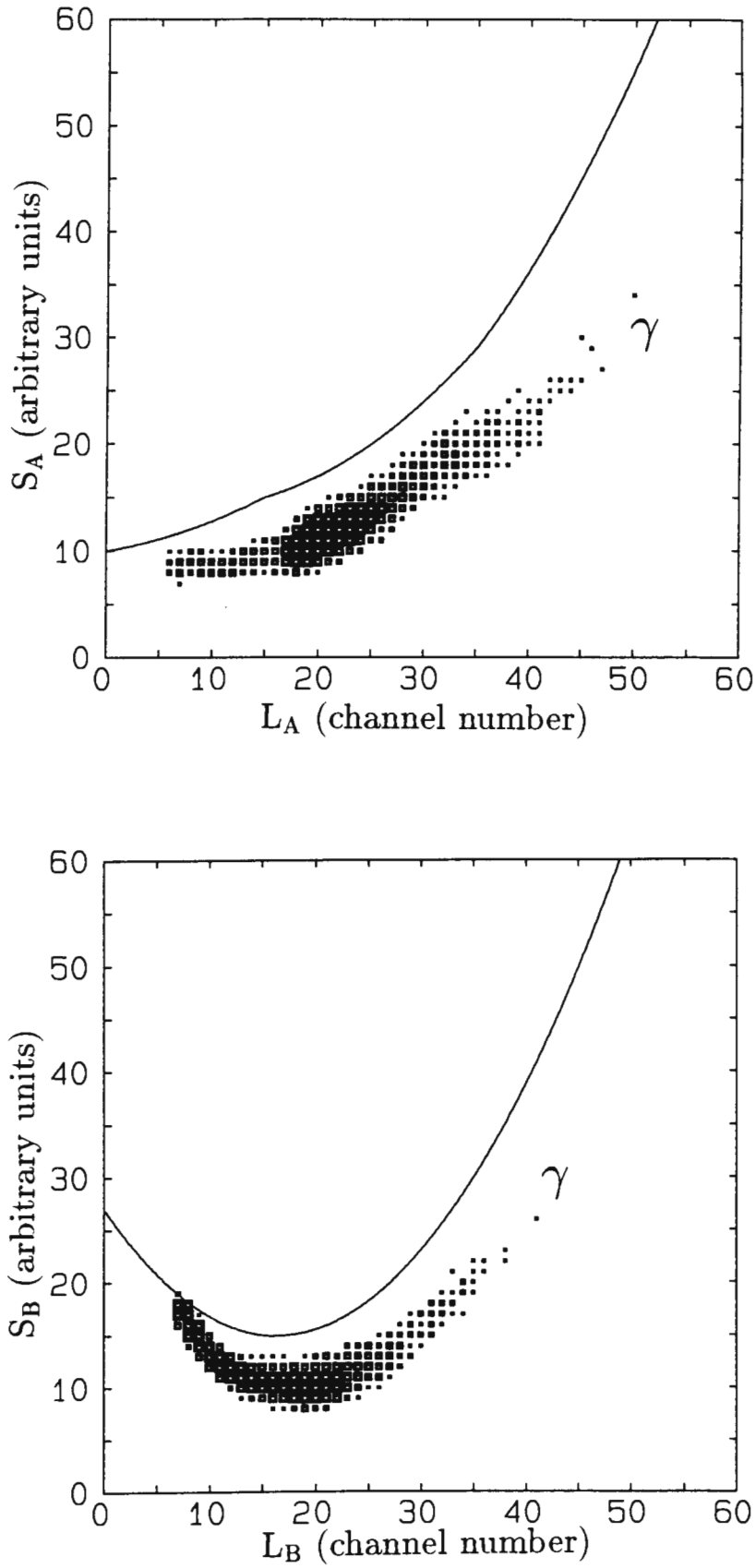

Figure 2.15: Pulse shape S vs pulse height L for detectors A (top) and B (all PAB events, beam OFF). The points in order of increasing size represent count thresholds of 5, 10, 20, 50 and 100 respectively.

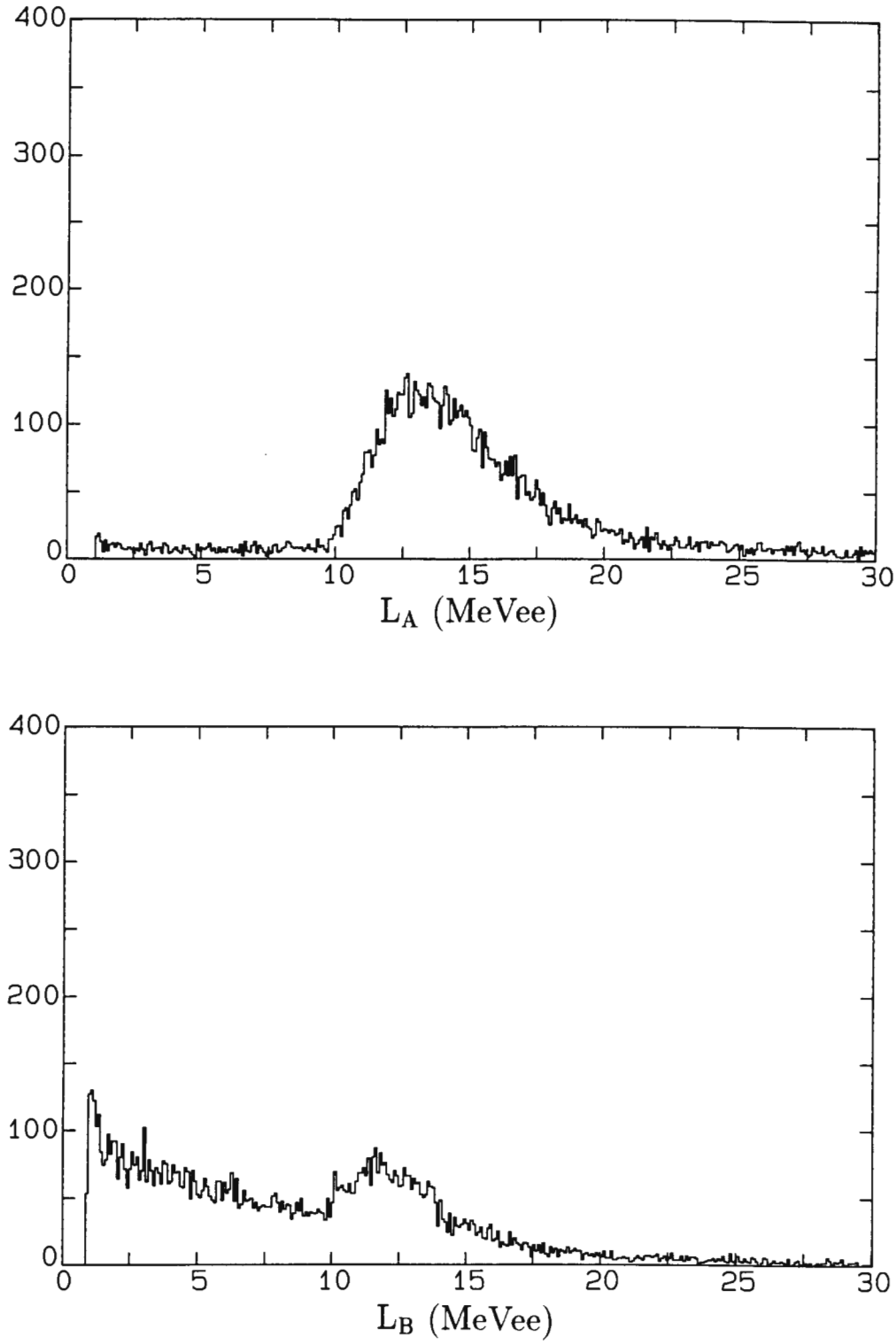

Figure 2.16: L_A and L_B spectra for events satisfying both pulse shape cuts LS_γ^A and LS_γ^B (beam OFF).

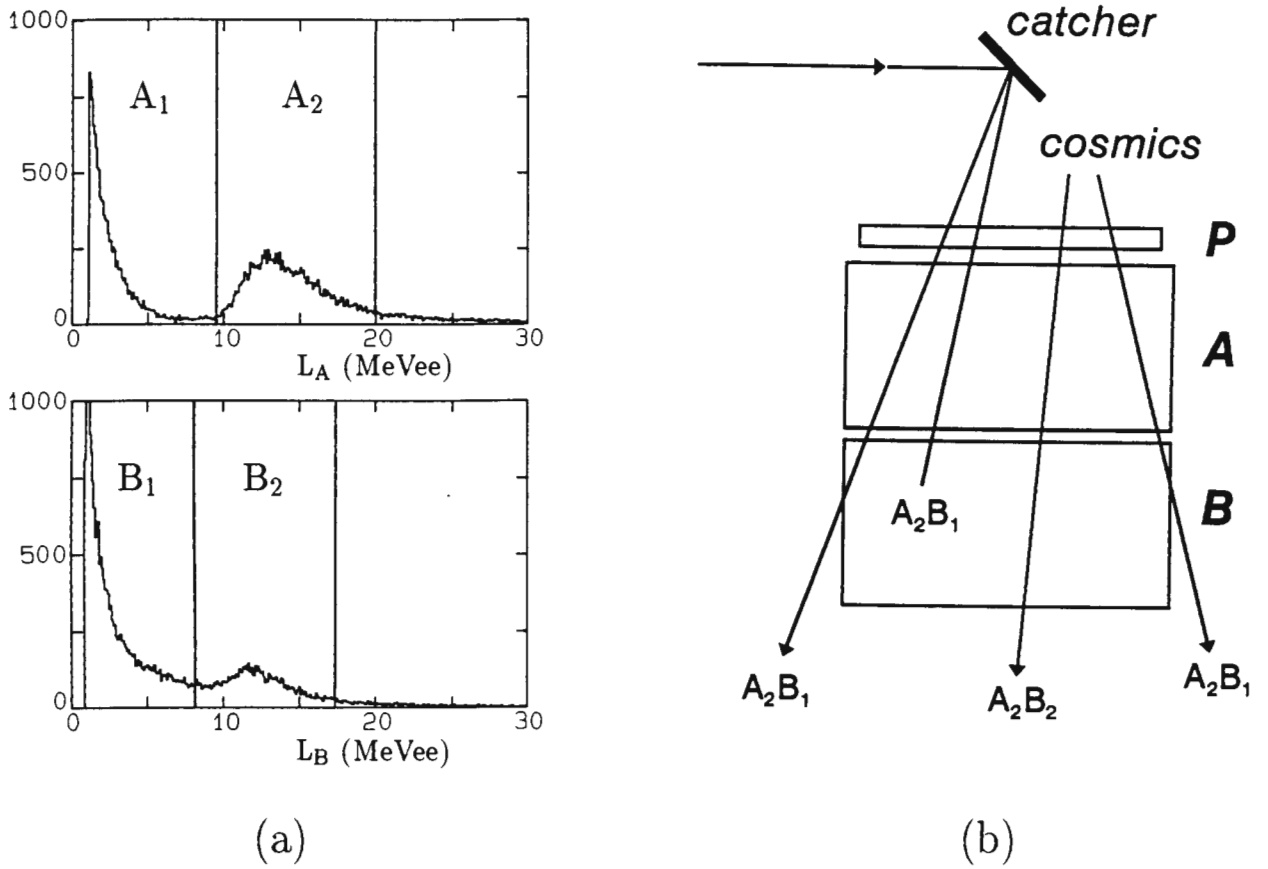

Figure 2.17: (a) L_A and L_B spectra showing the pulse height regions used to identify different types of event; and (b) a schematic representation of the event types.

C_I	6203
C_O	3589
N_I	7880
N_O	4413

Table 2.2: Table showing the numbers of events of types A_2B_2 (C) and A_2B_1 (N) for 'beam on' (I) and 'beam off' (O) conditions.

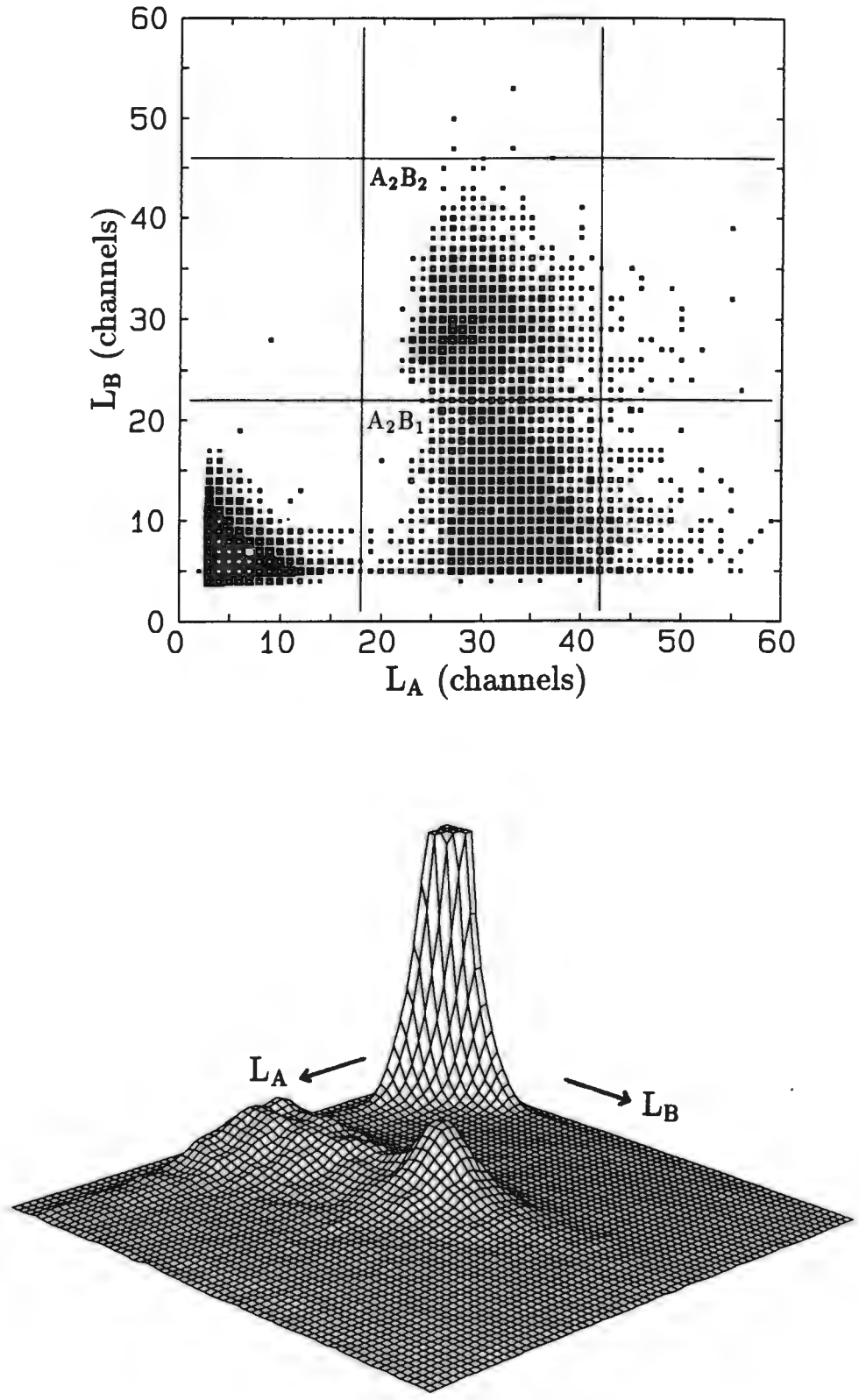

Figure 2.18: Scatter plot and its three dimensional counterpart of L_A vs L_B for data obtained with the beam ON, and satisfying both pulse shape cuts LS_γ^A and LS_γ^B.

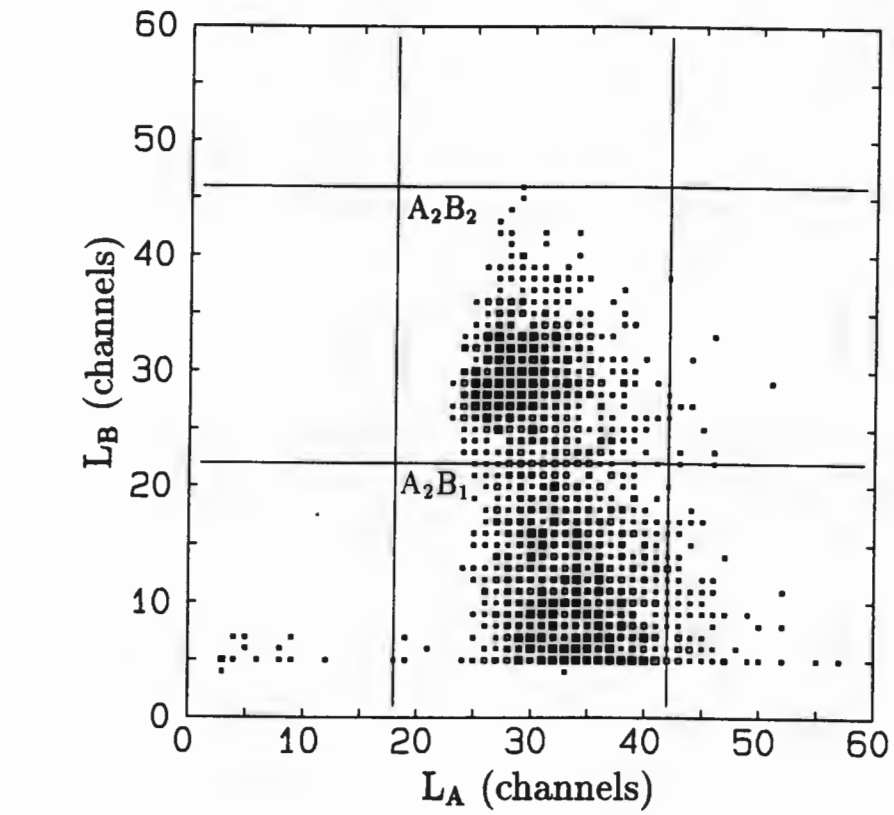

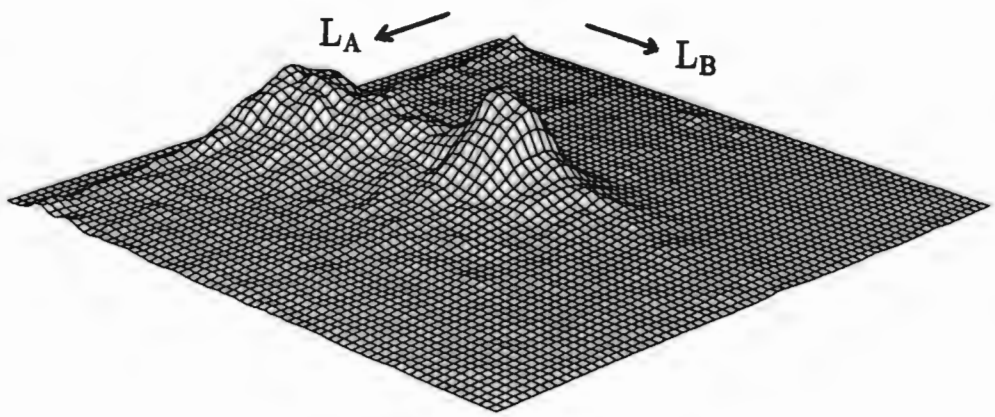

Figure 2.19: Scatter plot and its three dimensional counterpart of L_A vs L_B for data obtained with the beam OFF, and satisfying both pulse shape cuts LS_γ^A and LS_γ^B.

where $\frac{dN_e}{dt}$ is the number of accelerator-produced A_2B_1 events per second, and $d\Omega_B$ is the solid angle fraction of 4π subtended at the catcher by detector B. Since the beam was on for a total of 166601 seconds, this gives

$$\begin{aligned}\frac{dN_\mu}{dt} &= \frac{254}{166601\ s} \times \frac{1}{0.0126} \pm 49.2\% \\ &= 0.121 \pm 0.060\ s^{-1} \\ &= 7.26 \pm 3.57\ min^{-1}\end{aligned}$$

incident on the catcher. The area of the catcher illuminated by the muon beam was 10.2 cm^2, hence the observed muon intensity is

$$\frac{dN_\mu}{dt} = 0.71 \pm 0.35\ cm^{-2}\ min^{-1}\ .$$

As before, the negative muon flux is expected to approximately 0.024 times the total muon flux, i.e.

$$\begin{aligned}\frac{dN_{\mu^-}}{dt} &= 0.024 \times (0.71 \pm 0.35)\ cm^{-2}\ min^{-1} \\ &= 0.012 \pm 0.008\ cm^{-2}\ min^{-1}\ ,\end{aligned}$$

which is in good agreement with the expected negative muon flux of 0.014 cm^{-2} min^{-1} calculated in Section 2.1.2.

2.4.3 T_M spectra

Recall that T_M is the time-of-flight over the distance TM (see Figure 2.5). The T_M singles spectrum is presented in Figure 2.20. It consists of a sharp gamma ray peak at T_M = 27 ns followed by a broad distribution containing particles which travelled the 8055 mm flight path at lower velocities. These particles could be spallation protons, deuterons, alphas or neutrons (which knock out protons from the plastic, thus making scintillations), or muons. They are unlikely to be pions emitted in the solid angle subtended at the target by the catcher, since the vast majority of these pions (τ_π = 26 ns) will decay before completing the 8 metre distance to the end of the flight path. Imposing the cuts LS_γ^A, LS_γ^B, L_A = 9–20 MeV and R = 127 on the data produces the T_M spectrum shown in Figure 2.21. A comparison of the vertical scales (counts per channel) of the two T_M spectra indicates that only a small fraction of the original events satisfies all the cuts.

If T_M is plotted against the pulse height L_M in detector M, the scatter plot in Figure 2.22 is obtained. The general form of this distribution is as expected for such a passing detector: particles of higher energies have lower times-of-flight and lower stopping powers, hence lower pulse heights Lm (the pulse height in the thin plastic scintillator is approximately proportional to the specific energy loss of the penetrating particle). The T_M versus L_M distribution is essentially a plot of E versus ΔE, which usually yields a separate locus for each type of particle traversing the detector. In this case, however, the pulse height resolution of the M detector is unfortunately not sufficient to permit the appearance of distinguishable loci, and particle identification is not possible.

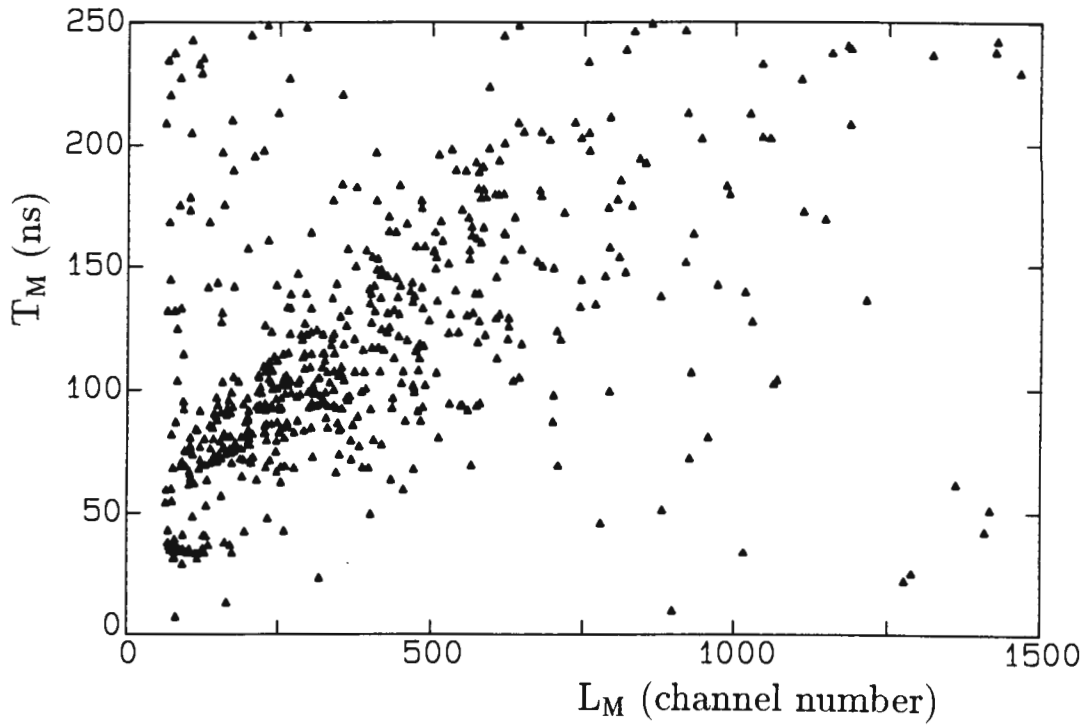

Figure 2.22: Time between the beam pulse and detector M (T_M) versus pulse height (L_M) in the same detector. The data shown satisfy the cuts LS_γ^A, LS_γ^B, L_A = 9–20 MeV and R = 127.

2.5 Summary

Starting with published cross-section data for (p,$\pi^\pm$) reactions at E_p = 201 MeV, an expected muon flux at the catcher of 0.60 cm^{-2} min^{-1} was calculated.

The muon production measurements were hampered by a strong cosmic muon background, as indicated by the large number of PAB coincidences obtained with the beam off. Attempts were made to exclude such cosmic events by means of a veto detector X (a plastic scintillator similar to detector P) placed behind detector B (refer to Figure 2.5). These attempts were unsuccessful, however, because of uncertainties regarding the operating threshold and efficiency of this X detector. The number of muon decay electrons attributable to the beam was thus estimated from the excess in the number of A_2B_1 type events in the 'beam ON' measurements over that of the 'beam OFF' measurements. From this the negative muon flux at the catcher was estimated to be 0.012 ± 0.009 cm^{-2} min^{-1}, in good agreement with the expected μ^- flux of 0.014 cm^{-2} min^{-1}.

Chapter 3

The search for μCF in deuterated anthracene

3.1 Phase 1: Objective and experimental approach

Section 1.3 focused on speculation regarding the existence of energy levels in anthracene molecules which could facilitate μCF by providing suitable states to take up the 1.97 meV ddμ binding energy in the formation of $C_{14}D_9$(ddμ) complex molecules.

The analysis of data from the muon test experiment presented in the previous chapter indicated a muon (μ^+ and μ^-) rate at the catcher of 0.71 ± 0.35 cm^{-2} min^{-1}, with the μ^- rate being 0.012 ± 0.009 cm^{-2} min^{-1}. Due to constraints imposed by the availibility of accelerator beam time, however, an experiment to seek μCF in deuterated anthracene was performed prior to the data of the test experiment being analysed, and thus without a full appreciation of this very low muon (in particular, μ^-) rate.

The primary objective of the experiment presented in the following sections was therefore to seek muon-catalysed fusions in deuterated anthracene.

Figure 3.1 illustrates the experimental setup at the NAC designed to meet this objective. The lead target T was oriented at 45° to the 200 MeV proton beam. The catcher chamber used in the previous experiment was replaced by a small box, $9 \times 9 \times 9$ cm^3, which housed a thin (200 μm) NE101 plastic scintillator M (diameter 4 cm), and either of two anthracene crystals C, one natural and the other deuterated. Each of these crystals is a cylinder 10 mm in diameter and 20 mm long, which was oriented with its cylindrical axis perpendicular to the flight path TM. The accelerator vacuum was sealed off with a flange containing a 50 μm Kapton[1] window of 2 cm diameter. A 10 cm long brass collimator with internal diameter 2 cm was nested in the flight pipe 90 cm upstream of the Kapton window. The box containing M and C was mounted outside the window, with a 2 cm diameter hole covered by thin aluminium foil directly opposite it, while a four-detector telescope was positioned

[1]Kapton is a polyimide film manufactured by Du Pont, having the chemical composition $C_{22}H_{10}N_2O_4$ and a density between 1.08 and 1.14 g/cm^3.

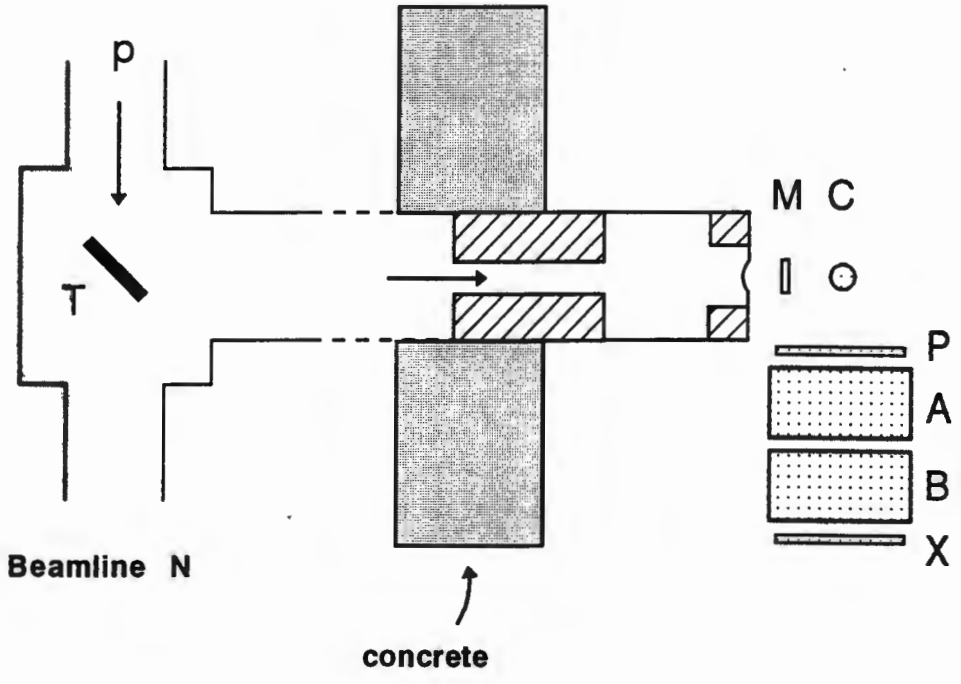

Figure 3.1: Schematic diagram of the detector setup used in the Phase 1 experiment.

outside the box. The telescope comprised the plastic and liquid scintillators P, A and B used previously, and an additional detector X (similar to P).

In this configuration the deuterated crystal replaced the 'catcher' of the previous experiment, to be used as an active target i.e. a target which is simultaneously used as a detector. In addition to providing the medium for ddμ fusion, this active target in combination with M would lead to an improved method of tagging charged particles into C. The natural anthracene crystal would be used as a control for comparison with the deuterated one.

The experimental arrangement was designed so that different coincidence signatures could be used to identify and distinguish between various types of event, such as μCF, the decay of muons stopped in C, and the passage of cosmic muons through the system. The signature for dd fusion is the detection of 2.5 MeV neutrons in prompt coincidence with the arrival of muons in C (recall that fusion would occur within a time of the order of a nanosecond after the muon entered the crystal). Electrons from muon decay in C would be identified in the telescope as before, with PSD being used to separate n and γ events in the NE213 detectors. Cosmic muons imitating electrons in the telescope would be eliminated by their detection in the veto detector X.

3.1.1 Electronics

The following eleven parameters were recorded for each event:

L_A, the pulse height in detector A;

Bit	Input	Value
0	A	1
1	B	2
2	CA	4
3	CB	8
4	PA	16
5	BA	32
6	—	64
7	—	128
8	W_1	256
9	W_2	512
10	XA	1024
11	XB	2048

Table 3.1: Inputs to the pattern register. A single letter refers to a signal in the detector represented by that letter; double letters indicate fast coincidences between two detectors; and W_1 and W_2 are the window outputs of two TACs.

F_A, the fast component of L_A;
L_B, the pulse height in detector B;
F_B, the fast component of F_B;
L_M, the pulse height in detector M;
L_C, the pulse height in detector C;
L_P, the pulse height in detector P;
T_M, the time between the proton beam pulse and a signal in M;
T_1, the prompt coincidence time between C and A;
T_2, the delayed coincidence time between C and A;
R, the pattern register value.

A simplified block diagram of the electronics appears in Figure 3.2. A fast MC coincidence started all three TACs, with the T_2 START delayed by 400 ns, and provided an external strobe for L_M, L_C and T_M. The T_1 and T_M TACs were each operating on a range of 500 ns, while the T_2 TAC range was 5 μs. All three TAC windows were wide open, allowing time pulses of any amplitudes within their respective ranges to be processed. The T_M STOP was provided by the pulse selector RF (PSRF) of the cyclotron. The other two TACs were both stopped by a signal in either of the two liquid scintillators. This A *or* B STOP pulse was provided by the output of a logic FIFO having A and B as its inputs. Another FIFO was used to produce an output indicating W_1 *or* W_2. The event gate was controlled by a Universal Coincidence unit which required a triple coincidence between the outputs W_M, W_1 *or* W_2, and A *or* B. In other words, the event requirement was effectively an MC coincidence in conjunction with T_1 *or* T_2. Separation of the T_1 and T_2 events was to be achieved in the offline analysis with the aid of the pattern register, the inputs to which are displayed in Table 3.1. (The additional TAC T_2 was introduced in this run in an

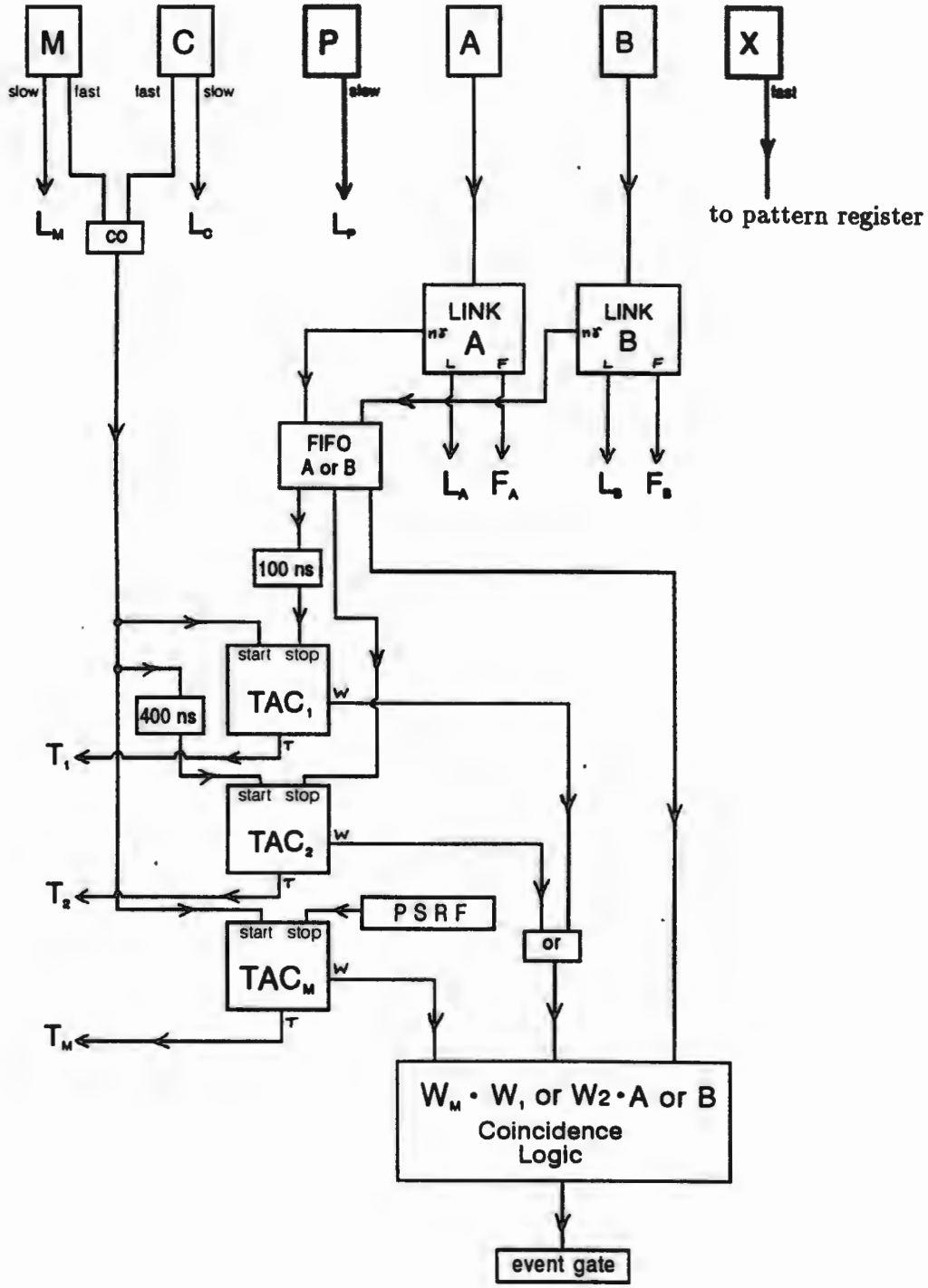

Figure 3.2: Simplified block diagram of electronics (Phase 1 experiment). Pattern register excluded for simplicity.

attempt to search for μ-e decays over a period comparable with the μ^- lifetime in carbon of 2 μs (refer to Figure 1.7). High backgrounds prevented this investigation from being useful however.)

3.2 Calibrations

3.2.1 Pulse height to energy calibrations

The pulse height calibrations of the NE213 scintillators were performed in the manner described earlier in Section 2.3.1.

The pulse height scales for detectors C, P and X were calibrated to MeVee from Compton electron spectra obtained using a ^{22}Na source. This produces gamma rays of 0.511 and 1.274 MeV, which in turn give rise to Compton edges at 0.341 and 1.061 MeV respectively. These two edges allow both the true zero and the energy scale to be established in each case.

An ^{241}Am source was used to calibrate the thin plastic scintillator M. The pulse height spectrum recorded with the source positioned a few millimetres from the scintillator contains a peak due to α particles (whose initial energies of 5.48 MeV are reduced a little by their passage through the air between the source and the scintillator). This corresponds to approximately 620 keVee pulse height. The true zero of the L_M scale was assumed to be at ADC channel 0, and the operating threshhold of the detector was determined to be 193 keVee.

3.2.2 Time calibrations

As mentioned earlier, the START for the T_M TAC was provided by a fast MC coincidence, while the STOP came from the PSRF of the cyclotron. Since the START could occur at any time between two proton beam pulses, the T_M distribution extends over a range equal to the time separating the pulses, in this case 269 ns. The zero of the T_M scale was then established from the position of the gamma peak in the spectrum, which must lie at a time corresponding to the time of flight of gamma rays over the distance TM (Figure 3.1).

For the calibration of T_1 a ^{22}Na source was placed on the axis between C and P. The T_1 TAC was started by C and self-stopped. After a short period of running in this mode, 100 ns was added to the T_1 STOP delay. The calibration spectrum thus contained two sharp peaks separated by 100 ns. The estimation of the T_1 zero will be discussed later in the text.

3.3 Results and discussion

The presentation and discussion of results below covers the following topics: first, the pulse shape discrimination cuts separating neutrons and gammas in the two liquid scintillators are presented. This is followed by general discussions of two two-parameter distributions (T_M vs L_C and T_1 vs L_A) central to the search for μCF.

The procedure for selecting μCF candidates from these distributions by means of various software cuts on the data is then explained. The effects of imposing the cuts are subsequently examined, and comparisons are made between the data collected with the deuterated and natural anthracene crystals.

3.3.1 Pulse shape discrimination cuts

Figure 3.3 shows scatter plots of pulse shape S versus pulse height L for detectors A and B, for a sample of the data from the deuterated anthracene runs (the number of neutron events has been enhanced relative to that of gamma events for clarity). The quality of PSD is good down to low pulse heights L (around 0.3 MeVee) in both detectors. The dashed lines on these plots indicate the positions in the LS planes of the software cuts used to separate neutron and gamma events during the data analysis. The symbols LS_n^A and LS_γ^A will be used to represent the selection of neutron and gamma events respectively in detector A, while LS_n^B and LS_γ^B will do likewise for detector B.

3.3.2 T_M vs L_C distributions

Mass discrimination by time-of-flight is a well-known particle identification technique. It can be explained in simple, non-relativistic terms as follows: with E, m, d and t representing the kinetic energy, mass, distance travelled and time-of-flight of a particle respectively,

$$E = \frac{1}{2}mv^2 = \frac{m}{2}\frac{d^2}{t^2}$$

$$\text{thus} \quad t = d\sqrt{\frac{m}{2E}} \quad \text{or} \quad t \propto \sqrt{\frac{m}{E}}$$

$$\text{i.e.} \quad t = \mathcal{F}(m, E) \; .$$

For a particular mass $t = \mathcal{F}(E)$, so that plotting t against E for particles of various masses produces a series of curves (one for each mass) as illustrated in Figure 3.4. Note that the curves move further out from the origin with increasing mass.

Although the pulse height responses of scintillators are not linear functions of energy, plots of time-of-flight vs scintillator pulse height yield distinct loci for particles of different masses. It should be possible, therefore, to separate muons from other particles arriving in the crystal using this technique.

Figure 3.5 shows a scatter plot of T_M versus L_C for an 8000 event sample of the deuterated anthracene data, and an accompanying schematic diagram to represent the prominent features of the distribution. A, B and C are identified (first from their relative numbers, and subsequently from calculations of pulse height in anthracene expected for different types of particles at a variety of times-of-flight) as proton, deuteron and alpha loci respectively.

The proton locus turns sharply at point P showing a different relationship between T_M and L_C, to wit, one of decreasing pulse height for decreasing T_M along the portion marked F. This is indicative of particles which have sufficient energy to

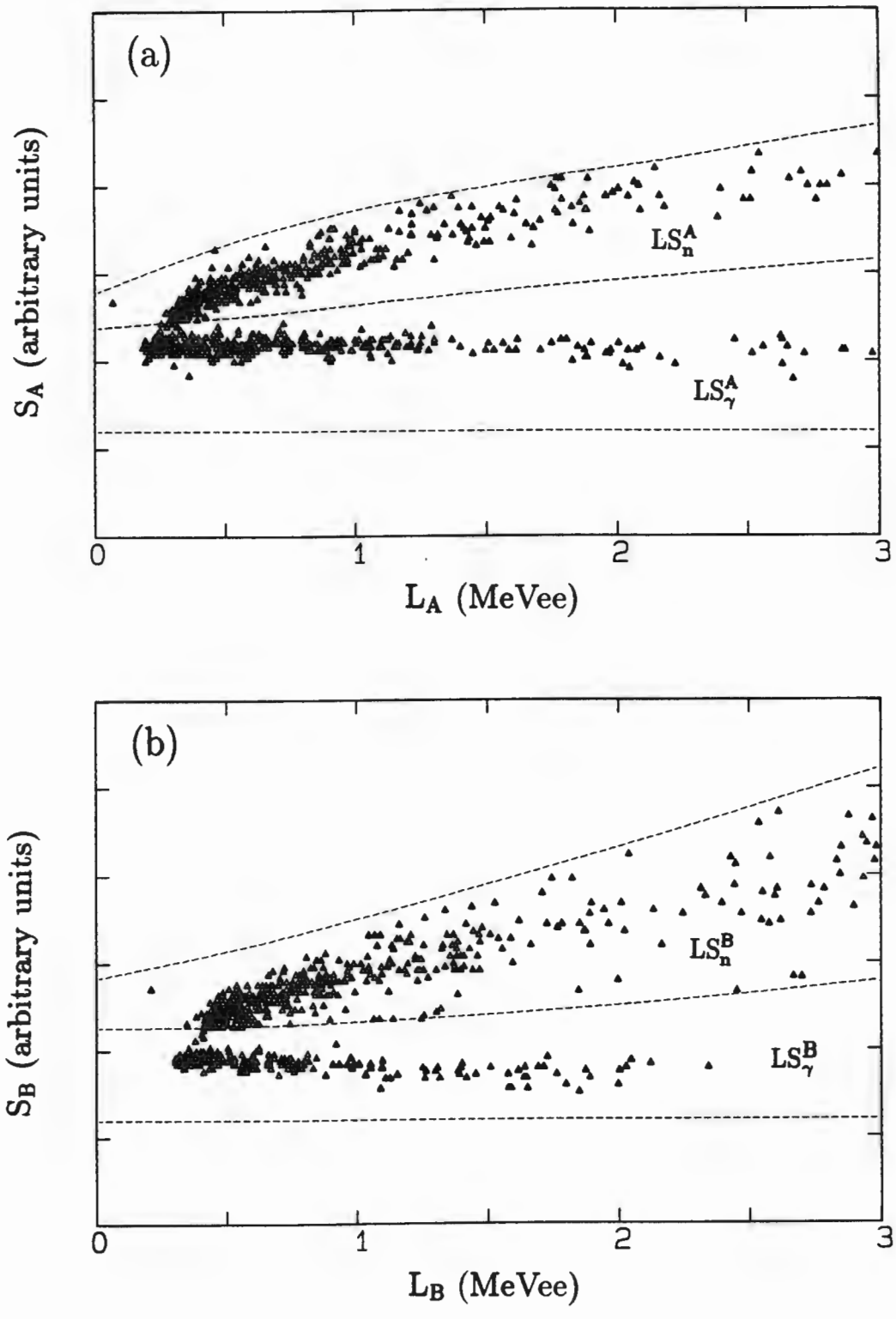

Figure 3.3: Scatter plots of pulse shape S against pulse height L for (a) detector A; and (b) detector B, from a sample of the deuterated anthracene data. The dashed lines indicate the software cuts used to separate neutrons and gammas.

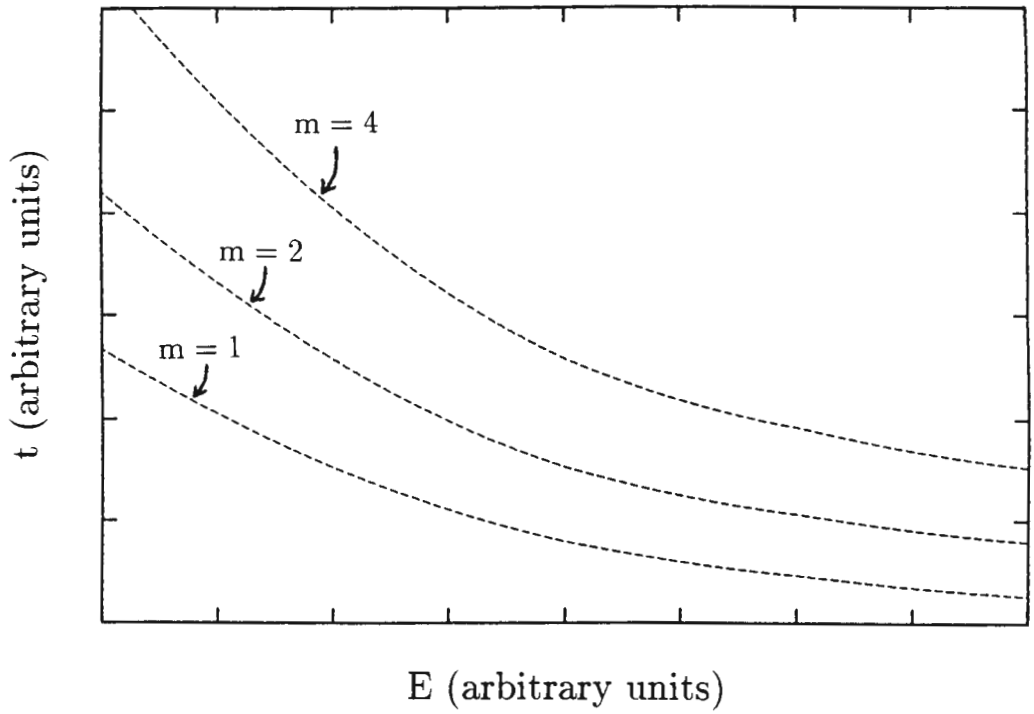

Figure 3.4: Time-of-flight t versus kinetic energy E, showing the proportionality of t to $(1/E)^{\frac{1}{2}}$ for each particle mass m as indicated.

pass right through the crystal C without being stopped. For such particles, the T_M vs L_C distribution is akin to a plot of TOF (hence E) vs ΔE. For increasing kinetic energies (decreasing TOF), the specific energy loss dE/dx of these particles decreases and so, therefore, does the energy they deposit in traversing a certain thickness of material. The turn-around point of the locus thus occurs at an energy for which the range of the particle equals the thickness of the target material, in this case 9 mm (or less, because of the crystal's cylindrical shape) of deuterated anthracene. The other two loci also have back-bending portions in the same way as the proton locus does. They are obscured to a large degree, however, by the high energy protons not stopped in C. At the same time, they must contribute to the diffusion of what appears at first sight to be a single back-bending locus.

The short, slightly curved locus E is attributed to electrons and gamma rays. The TOF of the highest energy electrons approaches that of gamma rays, so the lower edge of this peak in the T_M singles spectrum was used to set the T_M zero.

Muon events should lie somewhere between the proton and electron loci in this distribution. Muons are clearly not present in sufficient numbers to form a distinct locus in Figure 3.5. This is not surprising, however, partly because the intensity of muons is orders of magnitude lower than that of protons, as expected, and also because of the unfortunate position of the proton escape locus which would largely obscure even a fairly prominent muon locus.

Although a muon locus is not apparent in the L_CT_M plane, it is vital to the search for μCF in the deuterated crystal that its position be estimated, as this would enable software cuts to be imposed on the data to select muons entering the crystal. A muon 'corridor', within which the muon locus is expected to lie, was therefore calculated. Its position is indicated in Figure 3.6. This, then, is where

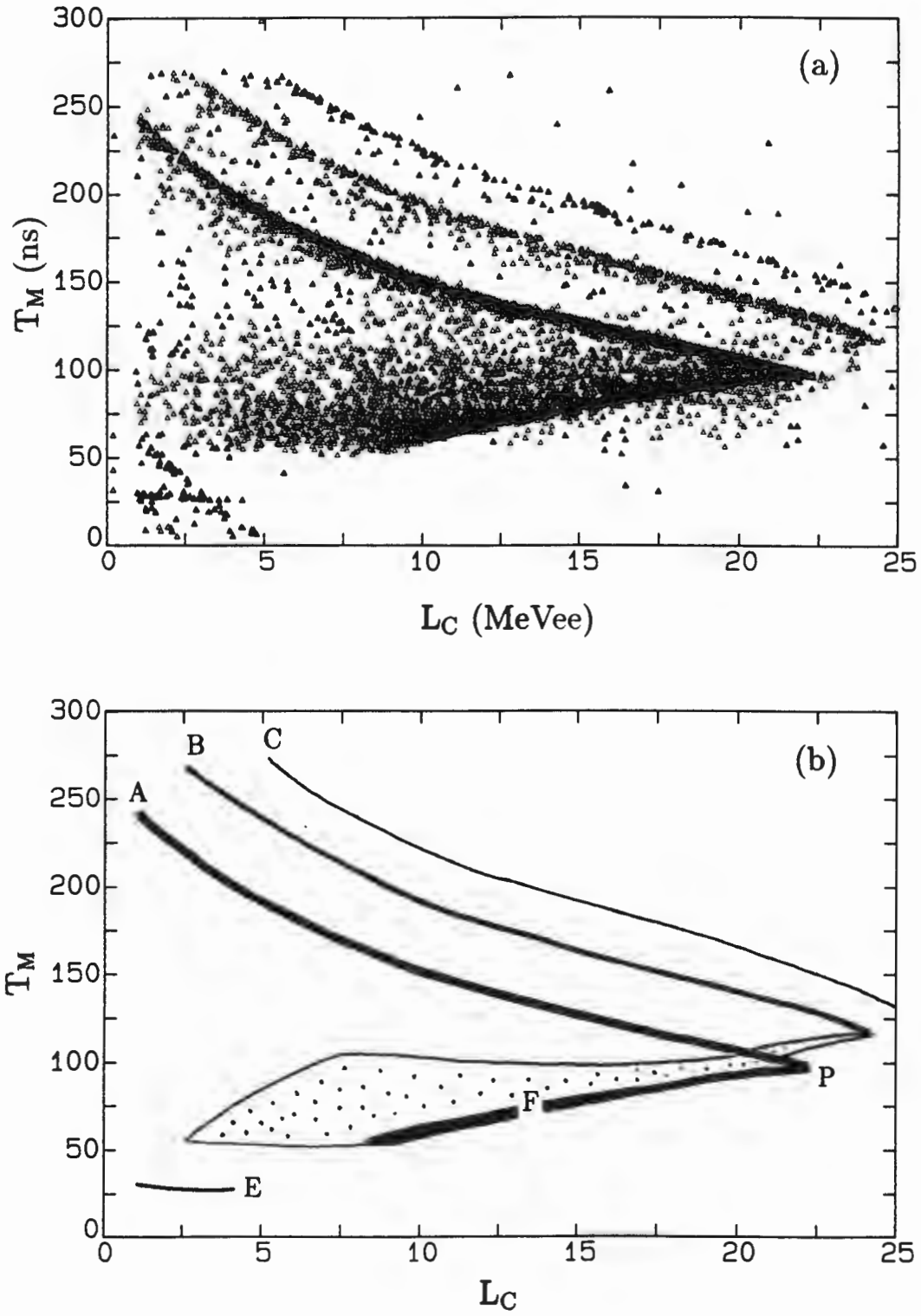

Figure 3.5: (a) T_M vs L_C for a random sample of 8000 events from the entire set of deuterated anthracene data; and (b) a schematic diagram of T_M vs L_C.

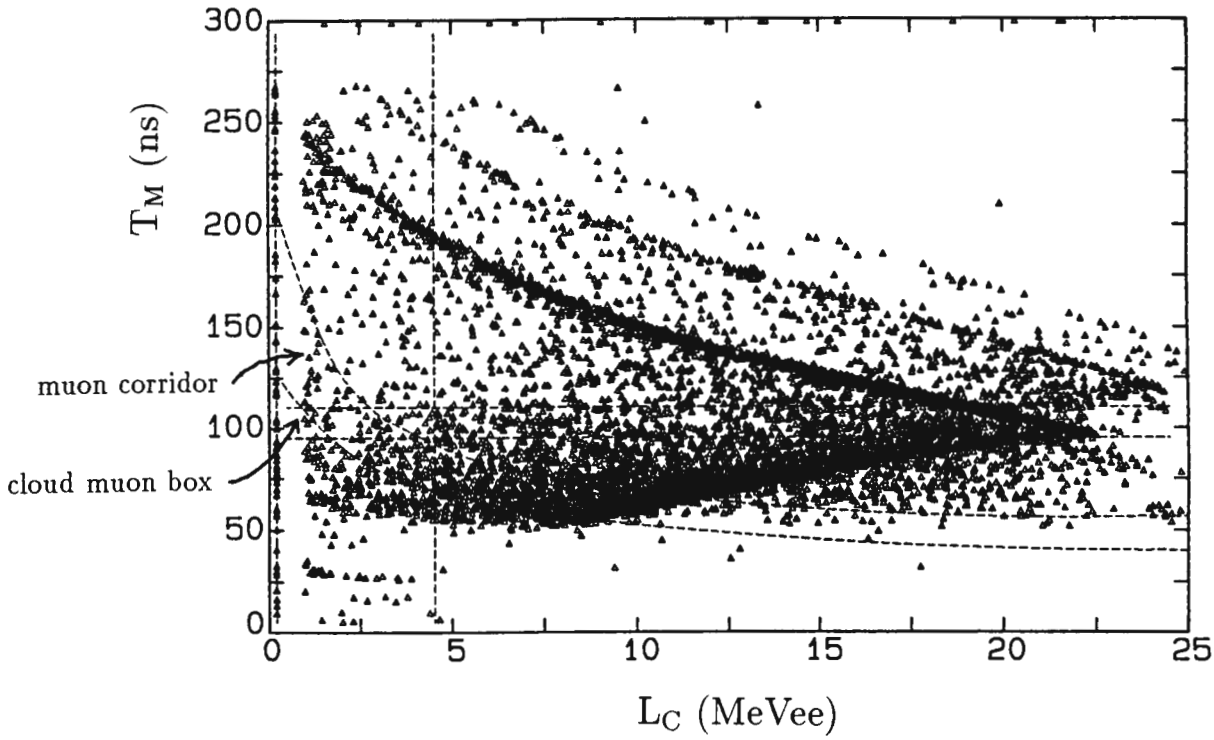

Figure 3.6: T_M vs L_C showing the calculated muon corridor, and the 'cloud muon box' (referred to later in the text).

accelerator-produced muons are expected to be situated on the $L_C T_M$ distribution.

3.3.3 T_1 vs L_A distributions

In Figure 3.7 T_1 is plotted against L_A for a data sample of 10 000 events. An accompanying schematic diagram of the resulting distribution is also shown. The portion marked *B* is attributed to background events i.e. scattered protons or neutrons having a flat distribution of arrival times in detector A, while *G* indicates the position at which γ rays are observed when not suppressed by pulse shape discrimination. The remaining portion *D* has a shape characteristic of neutrons in NE213 when the time to reach the detector from some common origin is plotted against the neutron pulse height in the scintillator. Since neutrons are detected via recoiling protons from np elastic scatters in NE213, the edge labelled *K* demarcates the maximum recoil proton energy possible at each neutron arrival time T_1 (i.e. each neutron kinetic energy).

The T_1 zero was estimated from the position of the γ peak *G* (Fig. 3.7), using the time taken for gammas to cover the known distance between C and A, and the T_1 calibration spectrum.

Figure 3.8 shows T_1 vs L_A from the deuterated anthracene runs for neutrons only (selected with the LS_n^A cut). It is possible that the 'gamma zero time' calculated in the manner described above, and displayed in this figure, does not correspond to the 'neutron zero time', however, because T_1 is governed by the timing output of a LINK 5010 PSD unit. This timing output is triggered by the LINK's internal constant fraction discriminator (see Appendix C), making it dependent on the rise

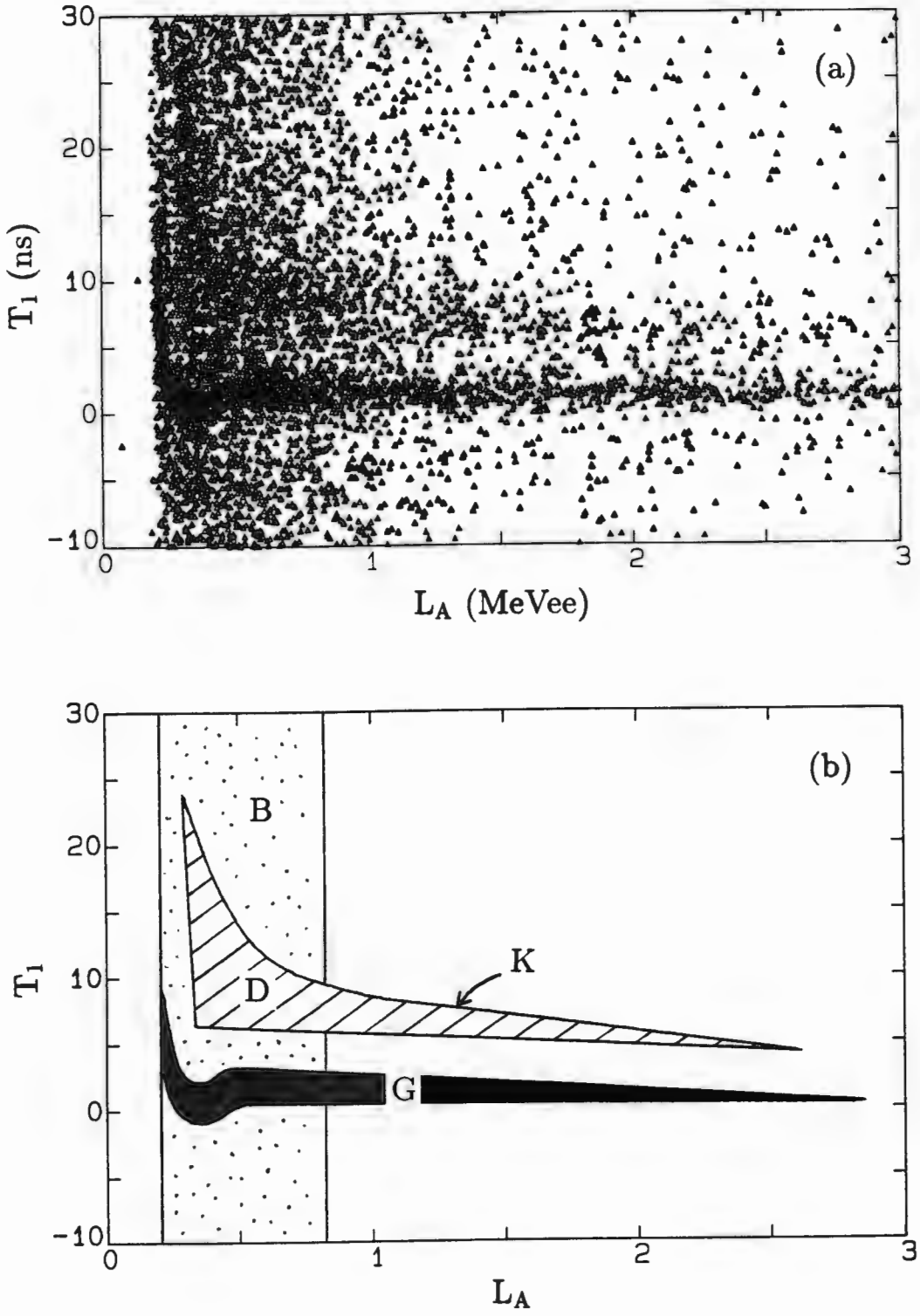

Figure 3.7: (a) T_1 vs L_A for 10 000 W_1 events (from deuterated anthracene runs); and (b) a schematic diagram of T_1 vs L_A.

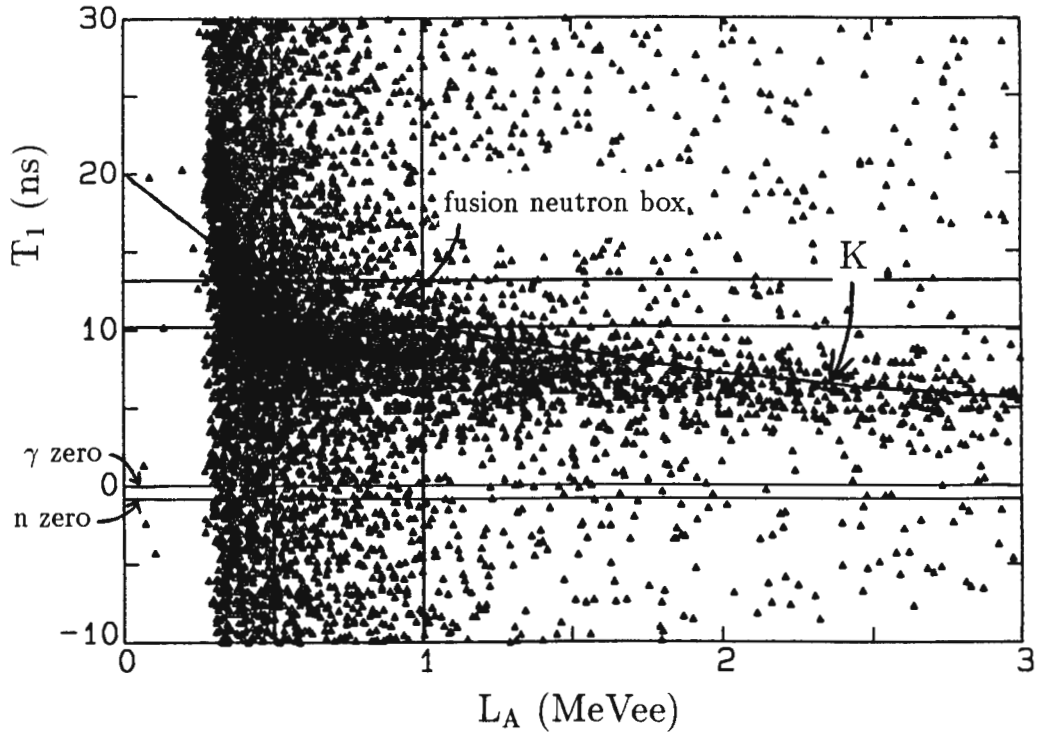

Figure 3.8: T_1 vs L_A for neutrons only (selected with the LS_n^A cut) from the deuterated anthracene runs. The curve K indicates the calculated edge of the distribution, which was used to locate the 'neutron zero time' of T_1 as explained in the text.

time of the pulse. The zero time can therefore be different for neutrons and gamma rays.

The identification of 2.5 MeV neutrons is necessary as they are the products of dd fusion. It is therefore important to estimate the 'neutron zero time' for T_1, as once this has been established it is possible to select fusion neutron candidates (which will have a characteristic flight time between C and A) using an appropriate window in the T_1 spectrum.

The 'neutron zero time' was estimated thus: the coordinates of a few points on the L_AT_1 edge K (see Figure 3.7) were calculated using the known neutron flight distance from C to A, and the NE213 pulse height response in MeVee to neutrons of particular energies in MeV. The curve joining the calculated points was then plotted on axes having the same scales as those in Figure 3.8, and superimposed to fit the data for L_A greater than 0.8 MeVee (at lower pulse heights the data is not expected to match the calculated curve because of the contribution of the background to the shape of the distribution). The position of the zero of the superimposed T_1 axis then indicates the 'neutron zero time', as shown in Figure 3.8. This is seen to be displaced from the 'gamma zero time' by 0.9 ns. The T_1 zero is set at the 'neutron zero time' throughout the discussion that follows.

3.3.4 Selecting μCF candidates

Muon-catalysed dd fusions would be indicated by 2.5 MeV ($L_A \leq 0.88$ MeVee) neutrons in detector A in prompt coincidence with muons entering the deuterated

crystal C. A number of cuts were therefore applied to the data in order to sift out the fusion candidates from other events.

Neutrons in detector A were isolated with the LS_n^A cut, while prompt coincidences between C and A were selected using the pattern register (R = 257–319; refer to Table 3.1).

A T_1 window of 11.5–14.0 ns selects neutrons of 2.02–2.99 Mev. Combined with a window requiring $L_A \leq 1$ MeVee this creates a 'fusion neutron box' in the L_AT_1 plane, as illustrated in Figure 3.8.

As explained early in Chapter 2 (Section 2.1.2), negative muons reaching the crystal are expected to be almost exclusively cloud muons with kinetic energies of about 3.4 MeV, reduced from 4.1 MeV by their passage through the Kapton window and other materials in front of the crystal. Cloud muon candidates were therefore selected by means of TOF (T_M) and pulse height (L_C) windows. A range of T_M from 95 to 110 ns corresponds to muon kinetic energies of 3.5 to 4.8 MeV. This, together with an L_C window of 0 to 4.5 MeVee, forms a 'cloud muon box' in the L_CT_M plane, as indicated in Figure 3.6.

3.3.5 Effects of the cuts: comparison of deuterated and natural anthracene runs

Figure 3.9 shows T_M vs L_C distributions from the deuterated anthracene runs. In (a) data satisfying the cuts LS_n^A and $T_1 = -10$ - 30 ns (i.e. events appearing in Figure 3.8) were selected, while in (b) the L_AT_1 fusion neutron box was applied to the data in (a). The effect of this box is a dramatic reduction in the overall number of events, with no obvious enhancement in the region contained by the L_CT_M cloud muon box.

The distributions of Figure 3.10 were obtained by imposing the same cuts on the natural anthracene data. A comparison of Figures 3.9(b) and 3.10(b) seems to indicate that the effect of these two cuts is not noticeably different for the two crystals.

Attention is now turned from muon candidates detected in C to fusion neutron candidates detected in A. Figures 3.11 and 3.12 each contain two T_1 vs L_A scatter plots for neutrons only in detector A. They are taken from the deuterated and natural anthracene data sets respectively. In each figure the upper plot contains events which are enclosed in the L_CT_M cloud muon box, while the lower one is subject to the tighter restriction imposed by both windows in the L_CT_M plane i.e. the cloud muon box *and* the muon corridor.

Comparing Fig. 3.11(a) with Fig. 3.8, the imposition of the cloud muon box is seen to have reduced the events in the T_1 vs L_A distribution fairly evenly, the remaining events showing no concentrations unusual to the pattern of the uncut plot. Also, there is no significant difference between Figure 3.11(a) and its corresponding figure from the natural anthracene data, Fig. 3.12(a).

A further reduction of events occurs when the muon corridor is applied to Figs. 3.11(a) and 3.12(a), resulting in Figs. 3.11(b) and 3.12(b). The region of interest (i.e. the fusion neutron box) is left with one event for each of deuterated and natural

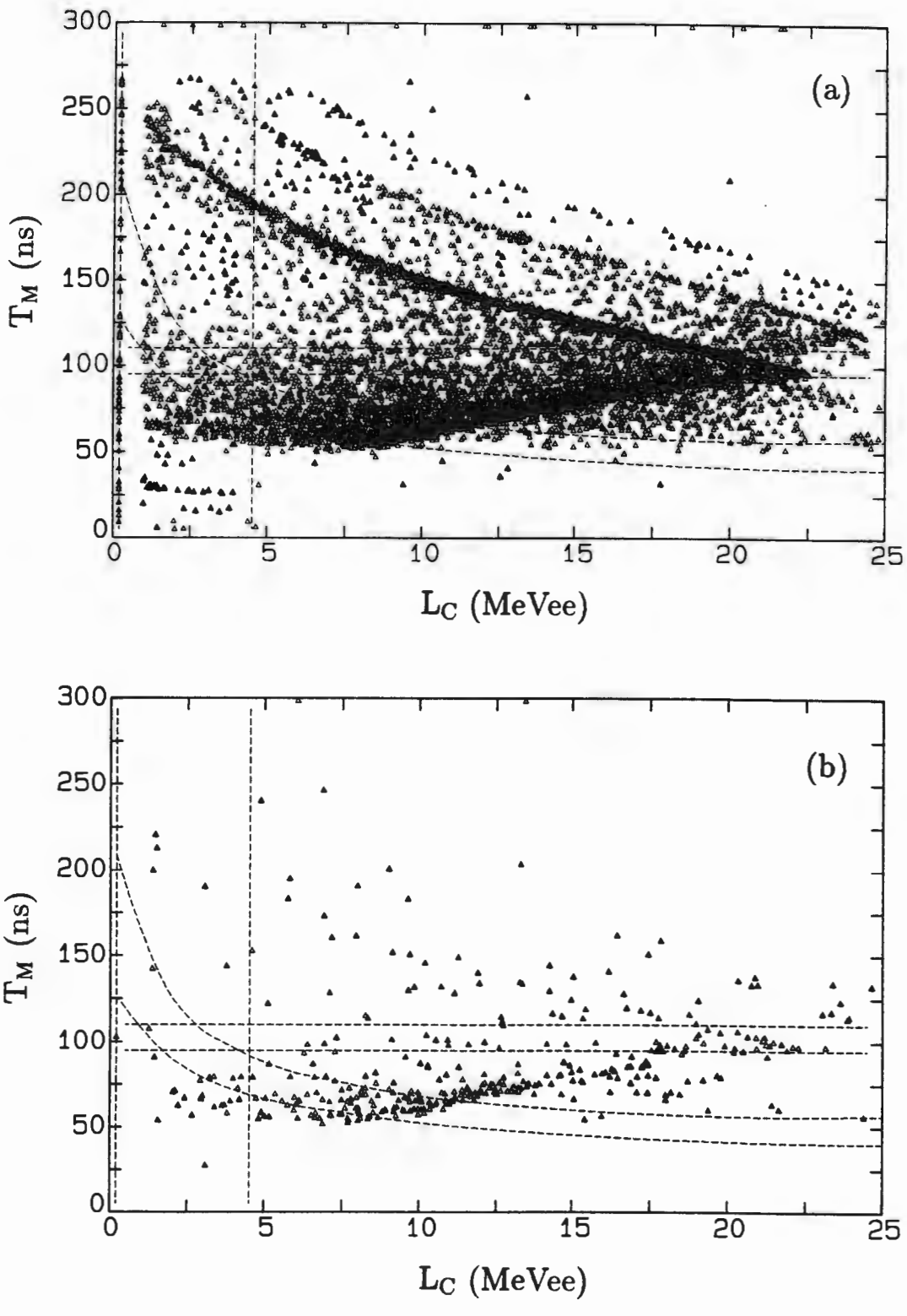

Figure 3.9: T_M vs L_C for deuterated anthracene. In (a) the data satisfy the cuts LS_n^A and $T_1 = -10 - 30$ ns; and in (b) the $L_A T_1$ fusion neutron box is imposed on the data in (a).

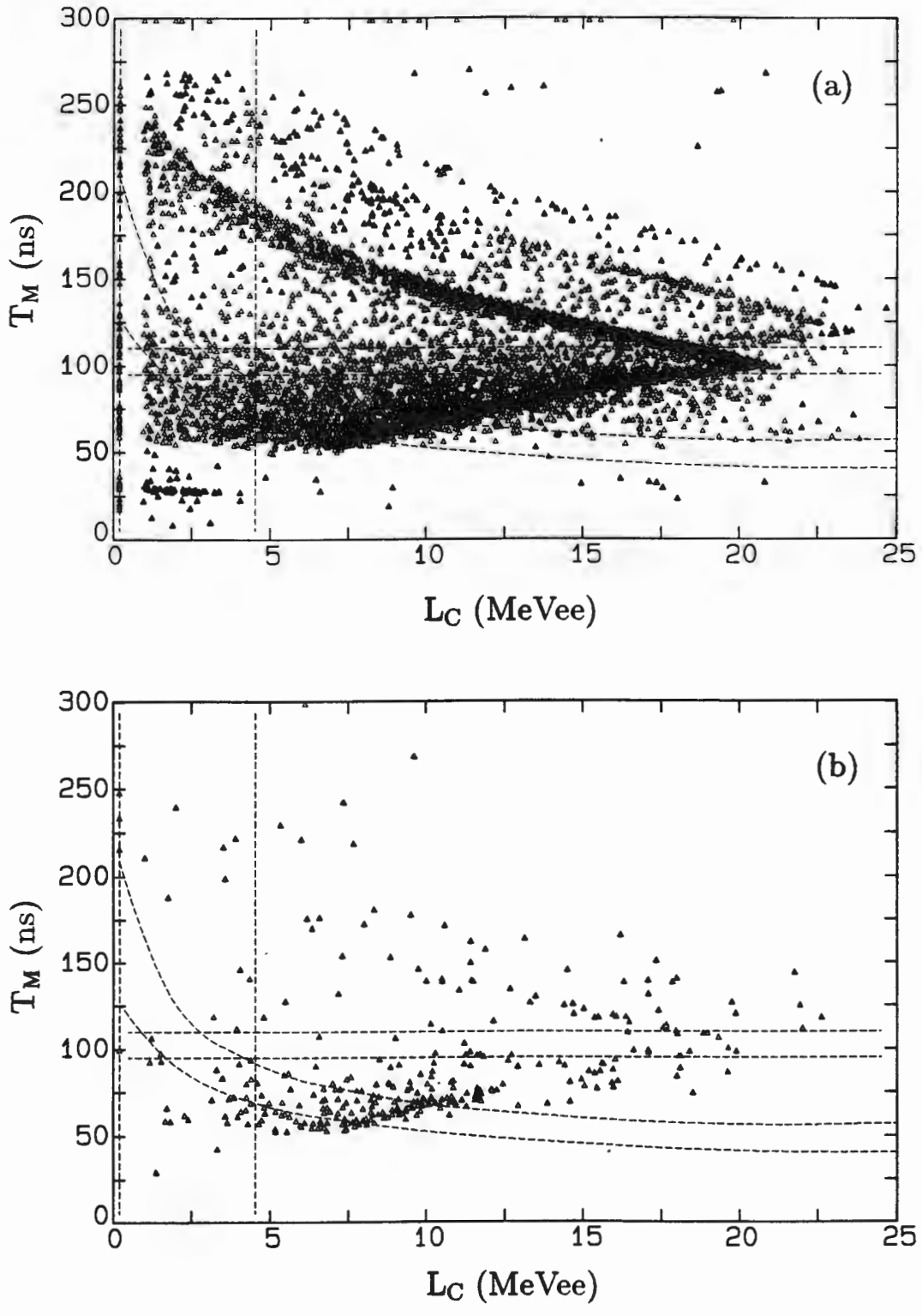

Figure 3.10: T_M vs L_C for natural anthracene. In (a) the data satisfy the cuts LS_n^A and $T_1 = -10 - 30$ ns; and in (b) the $L_A T_1$ fusion neutron box is imposed on the data in (a).

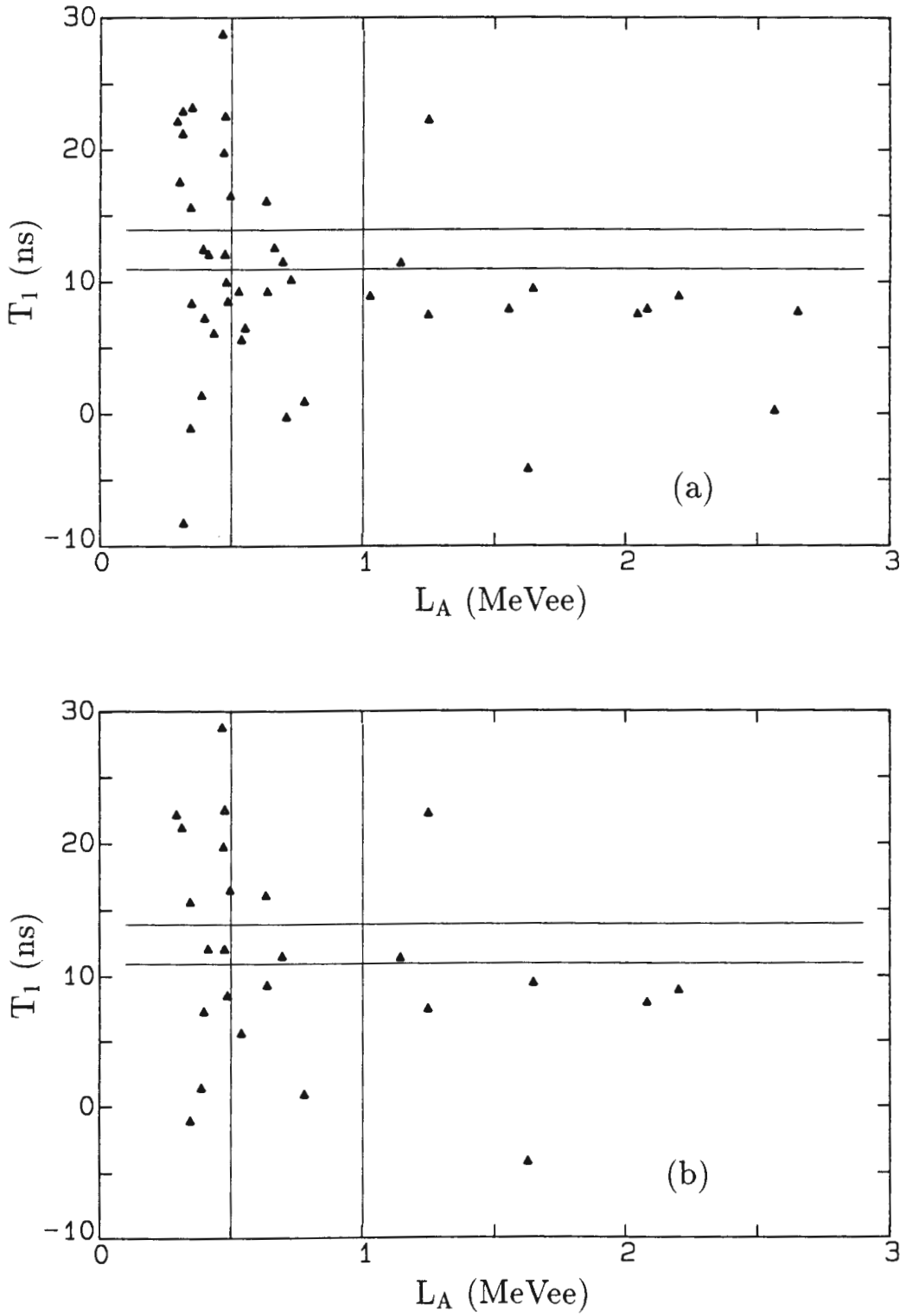

Figure 3.11: T_1 vs L_A (deuterated anthracene) for (a) LS_n^A and the cloud muon box; and (b) for LS_n^A, the cloud muon box *and* the muon corridor.

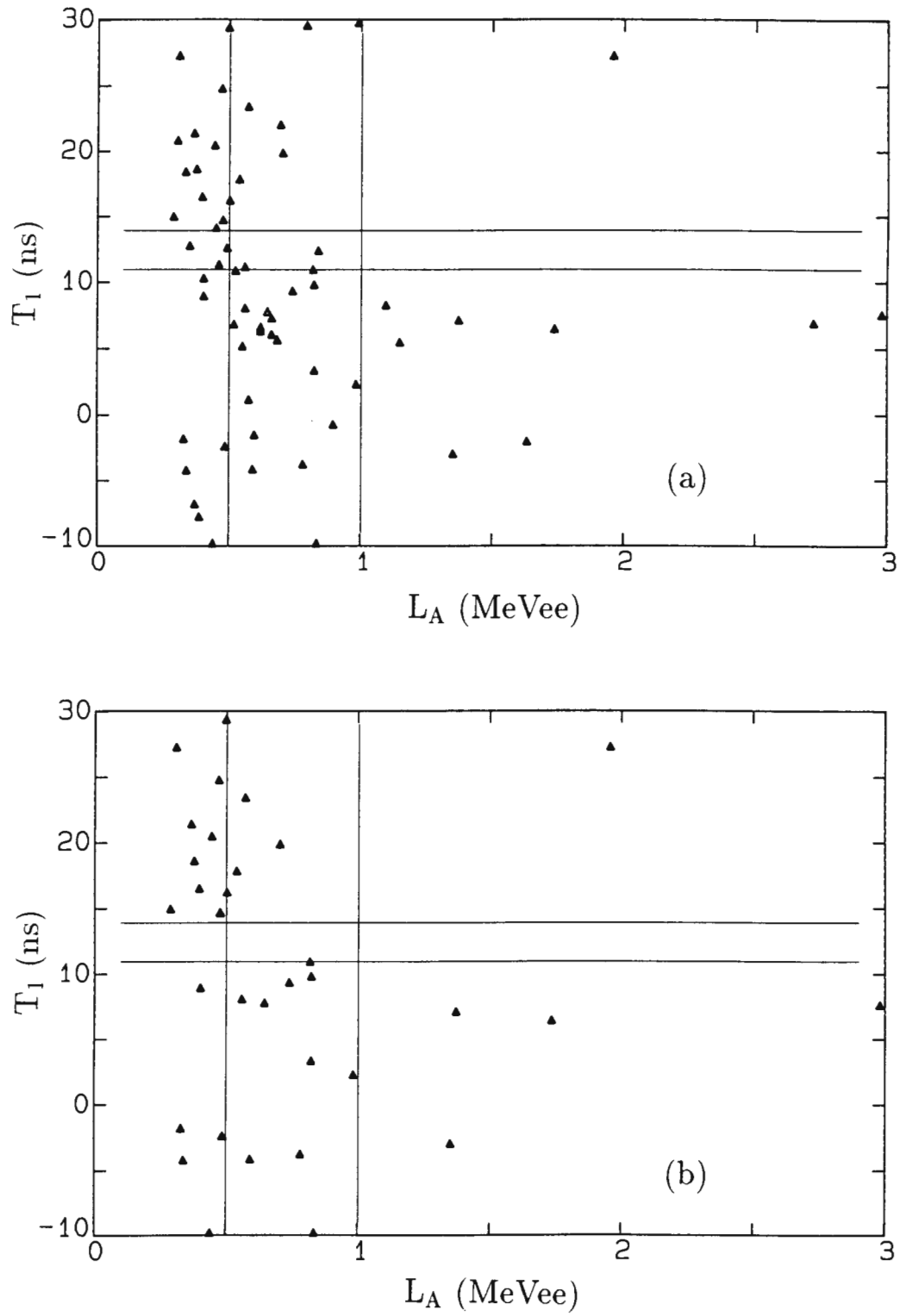

Figure 3.12: T_1 vs L_A (natural anthracene) for (a) LS_n^A and the cloud muon box; and (b) for LS_n^A, the cloud muon box *and* the muon corridor.

anthracene. This indicates that there is no significant evidence of muon-catalysed dd fusion in the deuterated anthracene crystal. However the fact that the fusion neutron box selects so few events inside the cloud muon box in deuterated anthracene (Figure 3.9) may suggest that there was an insufficient presence of muons in the crystal to draw conclusions about the occurrence of μCF. The application of the fusion neutron box to the $L_C T_M$ distribution of natural anthracene ought not to select muons. A comparison of Figs. 3.9(b) and 3.10(b) indicates that the fusion neutron box does not select events inside the cloud muon box preferentially for deuterated anthracene, as it should do if a significant number of muon-catalysed fusions were occurring in C.

3.3.6 Phase 1: Summary

The possibility of μCF in deuterated anthracene was neither confirmed nor negated in the experiment described above. Among the difficulties encountered in this initial experiment were the proton flyback locus in the $L_C T_M$ planes, and the absence of a clear muon signature which could be used to select μCF candidates from the data.

3.4 Phase 2: Objective and experimental modifications

The initial experiment discussed above prompted the performance of a second one designed to seek evidence of μCF in deuterated anthracene via an improved experimental setup. Figure 3.13 shows the arrangement of detectors used in the experiment. As before, a 1 mm thick Pb target was positioned at 45° to both the 200 MeV proton (primary) beam and the 8 m long flight pipe (refer to Figure 3.1). The brass collimator remained in its position 90 cm upstream of the Kapton window. The thin plastic scintillator M used previously was replaced by an NE102 disc 8 mm in diameter and 0.5 mm thick. This increase in thickness from 200 μm was to obtain larger signals from muons passing through the plastic, thus ensuring their detection. The anthracene (either deuterated or natural) crystal C was oriented with its cylindrical axis parallel to the (secondary) beam, and its circular face directly opposite the disc M. In this configuration the thickness of crystal presented to the beam is increased from 9 mm to 20 mm. A stilbene crystal V of thickness 12 mm and diameter 40 mm was placed behind C, its function being to veto events from particles escaping forwards from C. The plastic and liquid scintillators P and A used previously were positioned as shown in Figure 3.13. The purpose of A was to detect 2.5 MeV neutrons from dd fusions occurring in C, while P served to reject events in which charged particles entered A.

In this experiment particle identification by PSD was introduced for the crystal C, in addition to being used to identify neutrons in A as before. Also, the HV of the C detector was increased so that the operating scale of L_C extended to lower energies than before. This was intended to favour muons which were expected to enter the crystal with around 3 MeV kinetic energy.

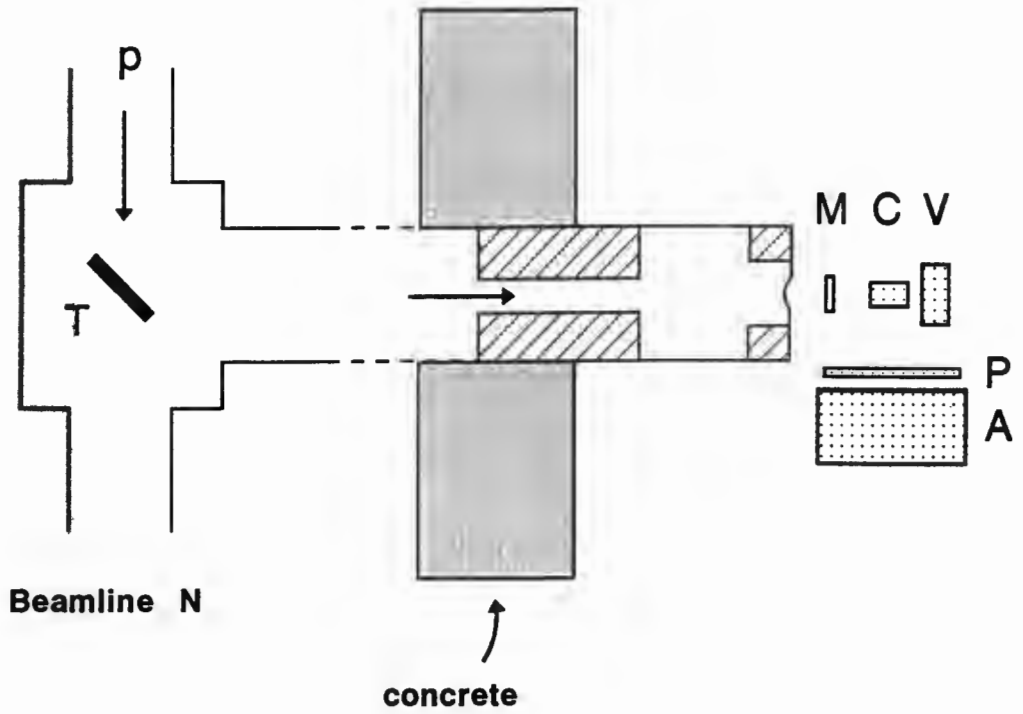

Figure 3.13: Plan view of detectors as arranged for the final (Phase 2) experiment. (Not to scale).

The calibrations (energy, time and PSD) were performed in like manner to those described previously, and the L_C spectra from deuterated and natural anthracene were brought into alignment via high voltage adjustments to the C photomultiplier.

3.4.1 Electronics

A simplified block diagram of the electronics is presented in Figure 3.14. Each 8-parameter event contained the following information:

L_A, the pulse height in detector A;
F_A, the fast component of L_A;
L_C, the pulse height in detector C;
F_C, the fast component of L_C;
L_M, the pulse height in detector M;
T_M, the TOF of particles from the lead target to M;
T_A, the time between signals in C and A;
R, the pattern register value.

Both TACs were started by a fast MC coincidence. The T_M STOP was provided by the PSRF of the cyclotron, while the T_A TAC was stopped by a signal in detector A. Each TAC was operating on a range of 500 ns, with its window open over the entire time spectrum. The event gate was provided by a triple coincidence between W_M, W_A (TAC window outputs) and C. That is to say, an event was accepted only when a fast MC coincidence was accompanied by a signal in A. The pattern register recorded various types of event as shown in Table 3.2.

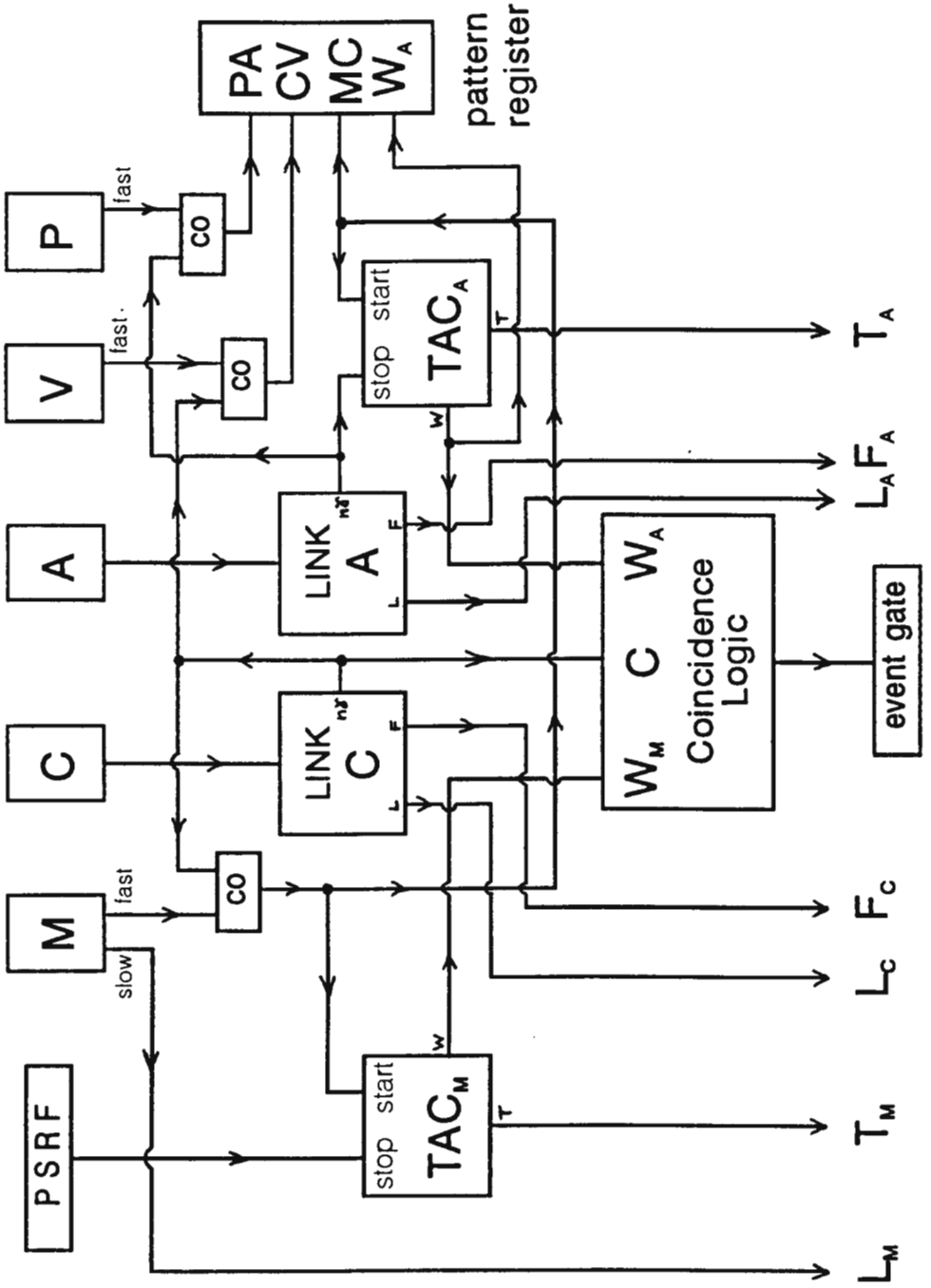

Figure 3.14: Simplified block diagram of electronics used in the final (Phase 2) experiment.

Bit	Input	Value
8	MC	256
9	W_A	512
10	PA	1024
11	CV	2048

Table 3.2: Pattern register inputs. Double letters represent fast coincidences between two detectors. W_A is the window output of the T_A TAC.

3.5 Results and discussion

3.5.1 Effect of the veto detector

Previously, particles which passed right through the crystal C increased the background in a crucial region of the L_CT_M plane, and in doing so possibly obscured muon events. In this experiment, however, the veto detector used in conjunction with the pattern register enabled such events to be eliminated.

Figure 3.15 shows T_M vs L_C with and without the veto condition applied to a sample of the deuterated anthracene data. In (a) all events in a 5400 event sample are accepted and the escaping particles, notably protons, are visible in the form of a backwards-bending locus as before (cf. Figure 3.5). The turn-around point of the locus is not visible here, however, as the L_C range extends only up to 15 MeVee. Also, the locus of escaping protons does not reach down to pulse heights as low as around 7 MeVee as before, because of the greater thickness of crystal that must be traversed in the present geometry. Figure 3.15(b) shows clearly the effect of rejecting events for which a CV coincidence was present. The proton escape locus disappears, and the concentration of events between the proton and gamma/electron loci is reduced.

In the analysis that follows, therefore, the original data sets for both crystals have been reduced to contain only unvetoed (no CV coincidences) events.

3.5.2 PSD on the crystals C

Figure 3.16 is a scatter plot of pulse shape S_C versus pulse height L_C for a sample of 1000 unvetoed events in deuterated anthracene. It shows the distinct separation between the electron (or gamma) locus and that containing protons and other more massive particles. Figure 3.17 was obtained by selecting (for clarity) equal-number samples of events from each of the three corridors of Fig. 3.15(b) respectively, and plotting S_C versus L_C for these events, using a different symbol for each L_CT_M corridor. The positions of the resulting loci in the L_CS_C plane confirm their identities (as determined from mass separation by time-of-flight) as protons, deuterons and alphas, the higher mass particles having greater values of S_C at each particular L_C. The discrimination between protons, deuterons and alphas is rather poor here,

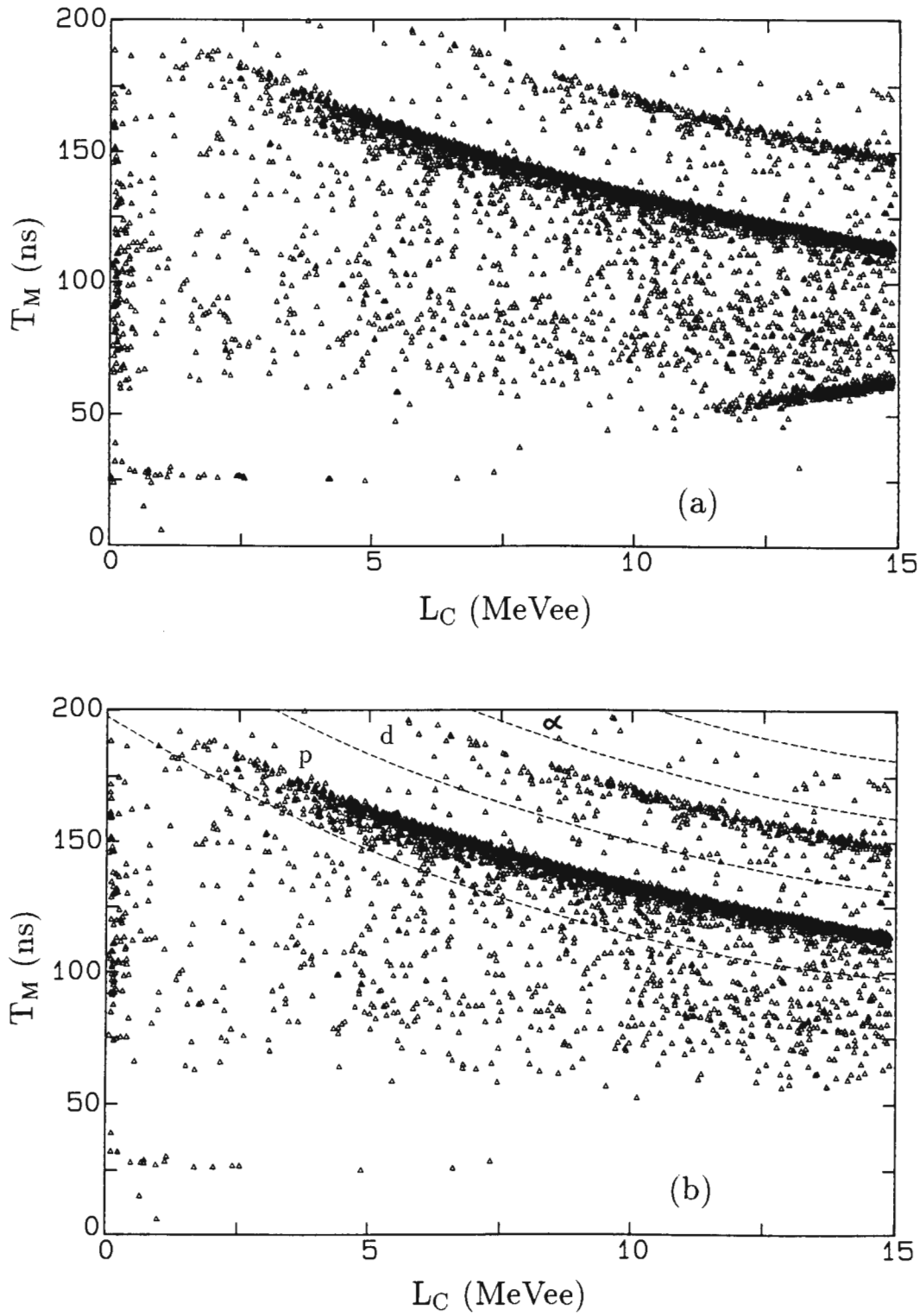

Figure 3.15: T_M vs L_C (deuterated anthracene) for (a) a sample of 5400 events (no cuts applied); and (b) the same sample, where CV coincidences have been rejected. The curved corridors shown in (b) are referred to later in the text.

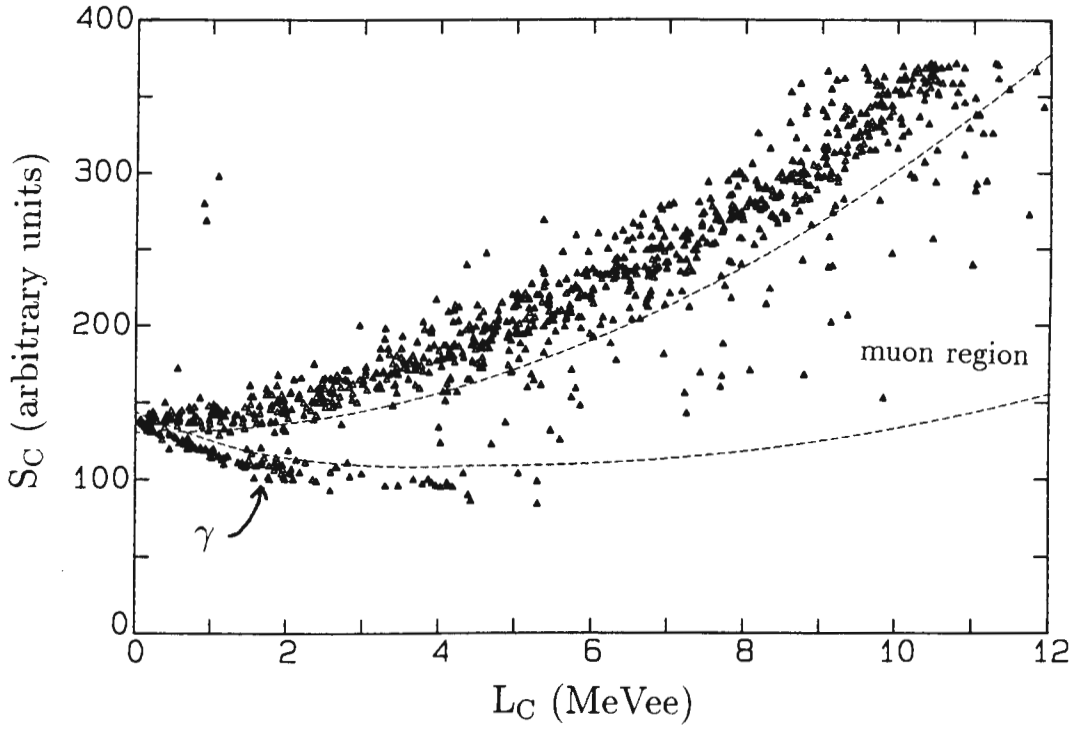

Figure 3.16: S_C vs L_C for 1 000 unvetoed events in deuterated anthracene. The γ (electron) locus is indicated, as is the region in which muons are expected to lie.

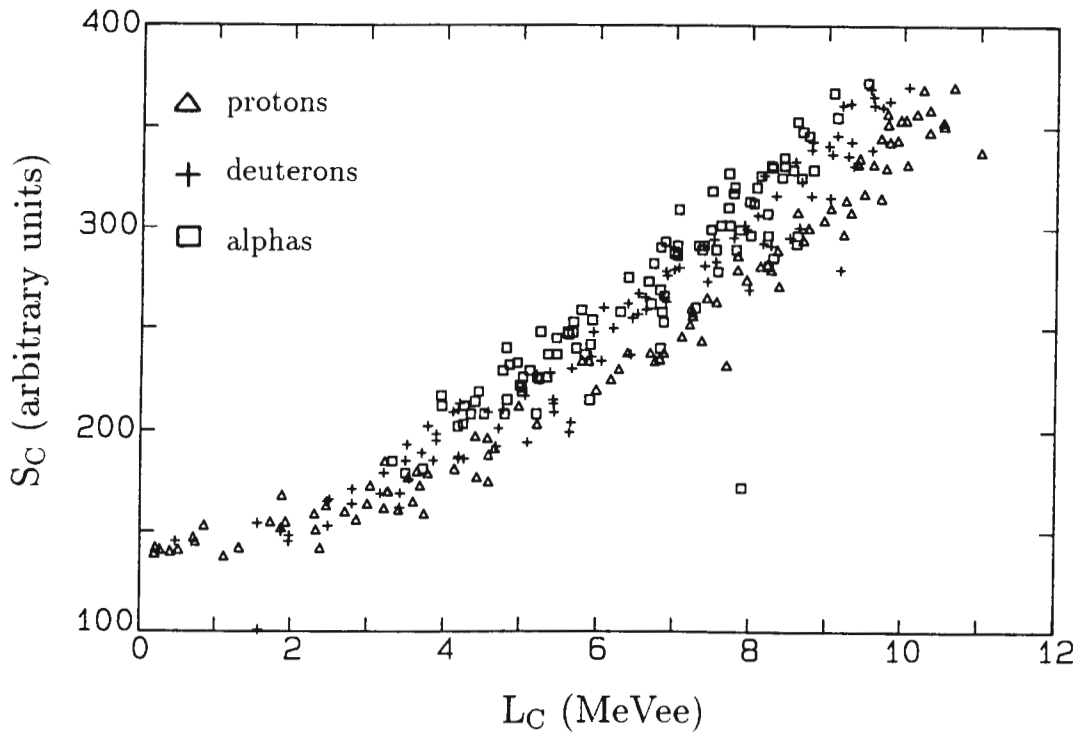

Figure 3.17: S_C vs L_C loci in deuterated anthracene, obtained by selecting events inside each of the three corridors indicated on Figure 3.15(b).

Cut	*Restriction*
R	768
LS_n^A	Neutron region in L_AS_A
T_M	95 – 110 ns
L_C	0 – 3.5 MeVee
T_A	6.9 – 11.0 ns
L_A	0.5 – 1.0 MeVee
LS_μ^C	Muon region in L_CS_C

Table 3.3: Cuts for selecting μCF candidates. For convenience LS_μ^C refers to the PSD cut of either crystal, as appropriate.

however, when compared for example with the separation of particles shown in Figure C.5 (Appendix C). The poor separation may be ascribed to the effects of pulse shape anisotropy in the crystal [Br 74], which manifests itself as a spread in pulse shape for the various particles.

Muons, having a mass intermediate between the proton and electron masses, are expected (despite the poor pulse shape discrimination) to occupy the region between the proton and electron loci in the L_CS_C plane, as shown in Figure 3.16.

For natural anthracene the positions of the various loci in the L_CS_C plane (not shown) differ slightly from those of the deuterated anthracene. This is due partly to the different responses induced by recoiling protons and deuterons, but chiefly because of the anisotropic response of anthracene [Br 74, Br 88] and the different orientations of the crystal axes relative to the cylindrical axis for the deuterated and natural anthracene crystals respectively. The 'muon' region in the L_CS_C plane of natural anthracene was therefore determined independently, in the same way as for the deuterated crystal.

3.5.3 Software cuts to select μCF candidates

Various software cuts, designed to select d-d fusion candidates, were applied to the data. These cuts are presented in Table 3.3 and discussed below.

The pattern register requirement was tightened to R = 768 in order to reject PA coincidences in addition to CV coincidences (refer to Table 3.2). Thus events were rejected for which charged particles were detected in A in coincidence with the MC coincidence. Neutrons in detector A were identified by a PSD cut LS_n^A, as before. The T_M and L_C windows were chosen to select cloud muons, as explained in Section 3.3.4, while the T_A and L_A windows again formed a 'fusion neutron box' in the L_AT_A plane. (The T_A window was modified appropriately to suit the distance between C and A, which differs from that of the Phase 1 experiment). In addition to any of these, the PSD cut LS_μ^C for the appropriate crystal (deuterated or natural) could be applied.

Set	Cuts	n_D	n_H	n_F	Upper limit
1	R,LS_n^A,T_M	21	13	8 ± 6	14
2	R,LS_n^A,T_M,LS_μ^C	12	8	4 ± 4	8
3	R,LS_n^A,T_M,L_C	5	2	3 ± 2	5
4	R,LS_n^A,T_M,L_C,LS_μ^C	2	0	2 ± 1	3

Table 3.4: Fusion neutron yield n_F for different cut sets.

3.5.4 Effects of the cuts: comparing deuterated and natural anthracene

Figures 3.18 to 3.21 contain plots of T_A vs L_A for different sets of cuts. In each of these figures, the upper and lower plots show deuterated and natural anthracene data respectively. The cuts R, LS_n^A and T_M, which together form the 'basic' cuts, are imposed throughout. Other cuts imposed in addition to the 'basic' set are indicated in the figure captions.

Comparing Figures 3.18 and 3.19, the application of LS_μ^C in addition to the basic cuts appears to select points inside the fusion neutron box preferentially for deuterated anthracene relative to the rest of the distribution. This does not occur for natural anthracene. Such a comparison is more difficult for Figures 3.20 and 3.21 because of the poor statistics involved. However, the application of each cut set results in a greater number of counts remaining inside the fusion neutron box for deuterated than for natural anthracene (see Figs. 3.18 to 3.21).

The neutron yield n_F from muon-catalysed dd fusion in the deuterated crystal can be estimated as follows from each of these four figures. If n_D and n_H represent the number of points inside the fusion neutron box for deuterated and natural anthracene respectively, then

$$n_F = n_D - n_H \pm \sqrt{(n_D + n_H)}\,.$$

Performing this calculation for each set of cuts results in the numbers presented in Table 3.4. Since the numbers of events are small and the validity of $\sqrt{n}$ statistics is questionable at this level, the results are also presented in the alternative form as upper limits at the one standard deviation level.

The number of negative muons incident on the deuterated crystal throughout the runs can be estimated from the μ^- flux obtained in Chapter 2:

$$\begin{aligned} N_{\mu^-} = \frac{dN_{\mu^-}}{dt}\,dt &= 0.012\ \mathrm{cm^{-2}\ min^{-1}} \times 1672\ \mathrm{min} \\ &= 20\ \mathrm{cm^{-2}}\,. \end{aligned}$$

Since the crystal presents a cross-sectional area of 0.64 $\mathrm{cm^{-2}}$ to the beam, this becomes $N_{\mu^-} = 13$. The fusion neutron yields obtained above then give a range of between 0.2 and 1.1 for an upper limit on the number of fusions per muon observed in deuterated anthracene. While this may seem unlikely, given the likelihood of

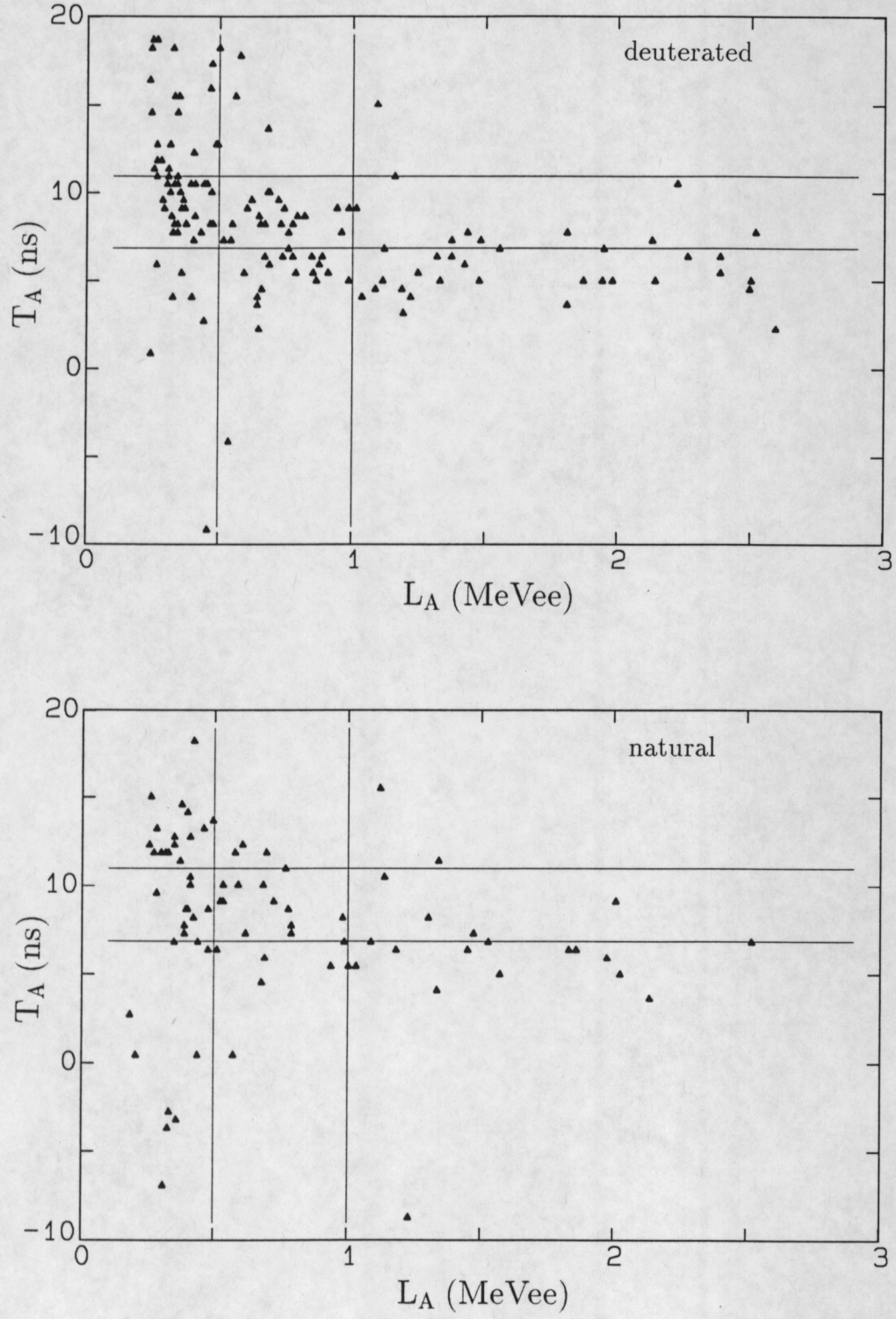

Figure 3.18: T_A vs L_A for the 'basic' cuts R, LS_n^A and T_M only. The upper and lower plots show data from the (equal-length) deuterated and natural anthracene runs respectively.

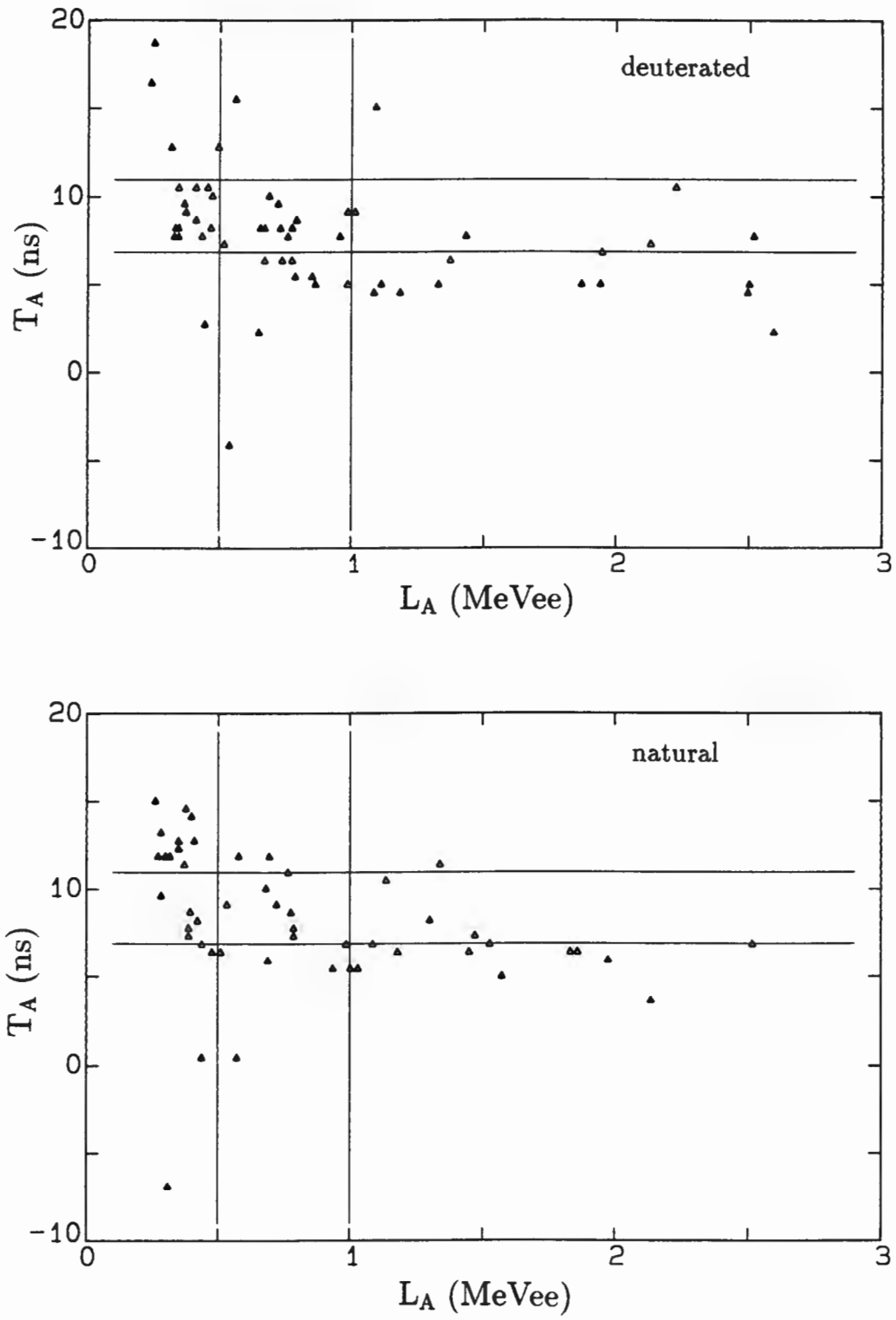

Figure 3.19: T_A vs L_A for the 'basic' cuts + LS_μ^C. The upper and lower plots show data from the deuterated and natural anthracene runs respectively.

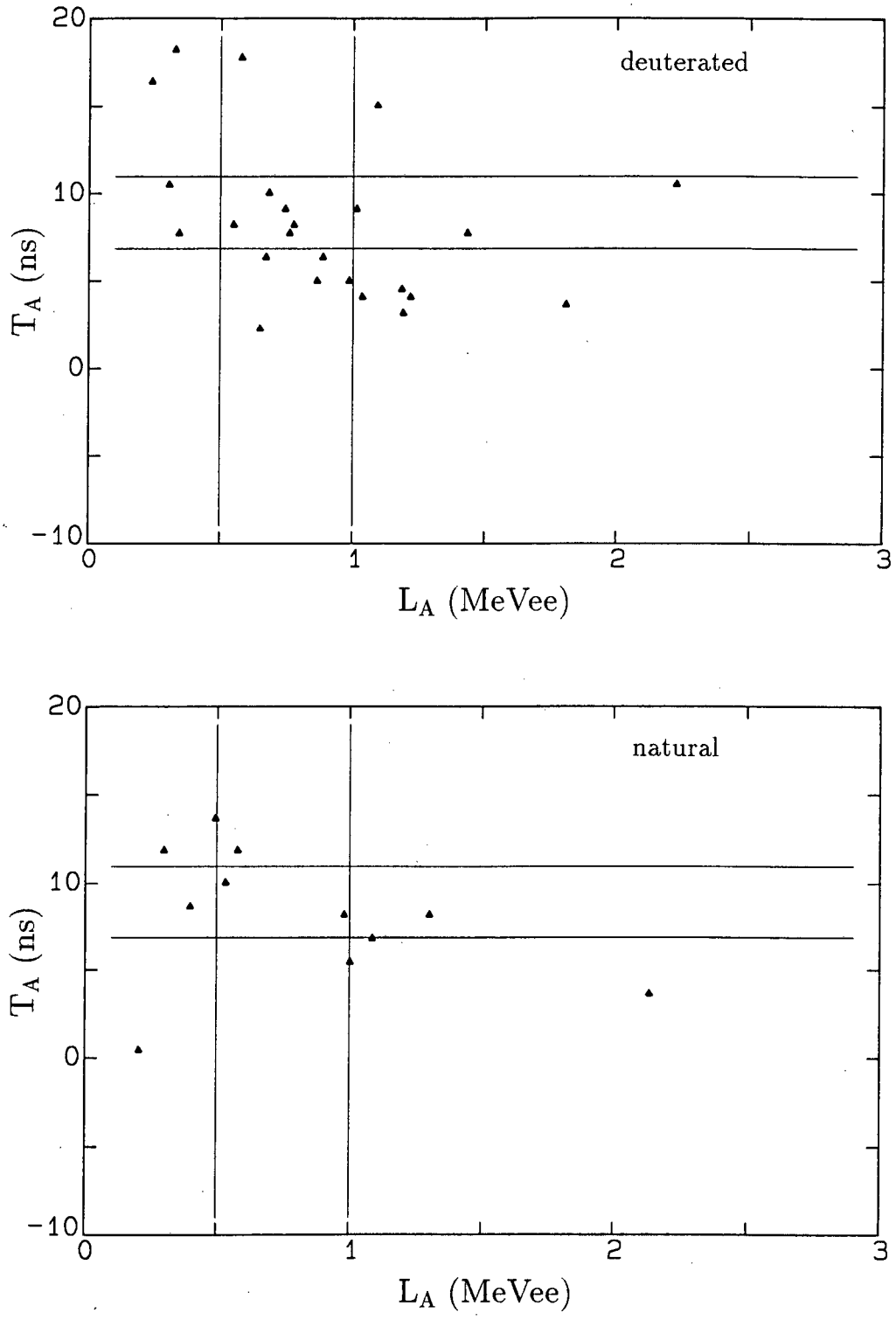

Figure 3.20: T_A vs L_A for the 'basic' cuts + the L_C cut. The upper and lower plots show data from the deuterated and natural anthracene runs respectively.

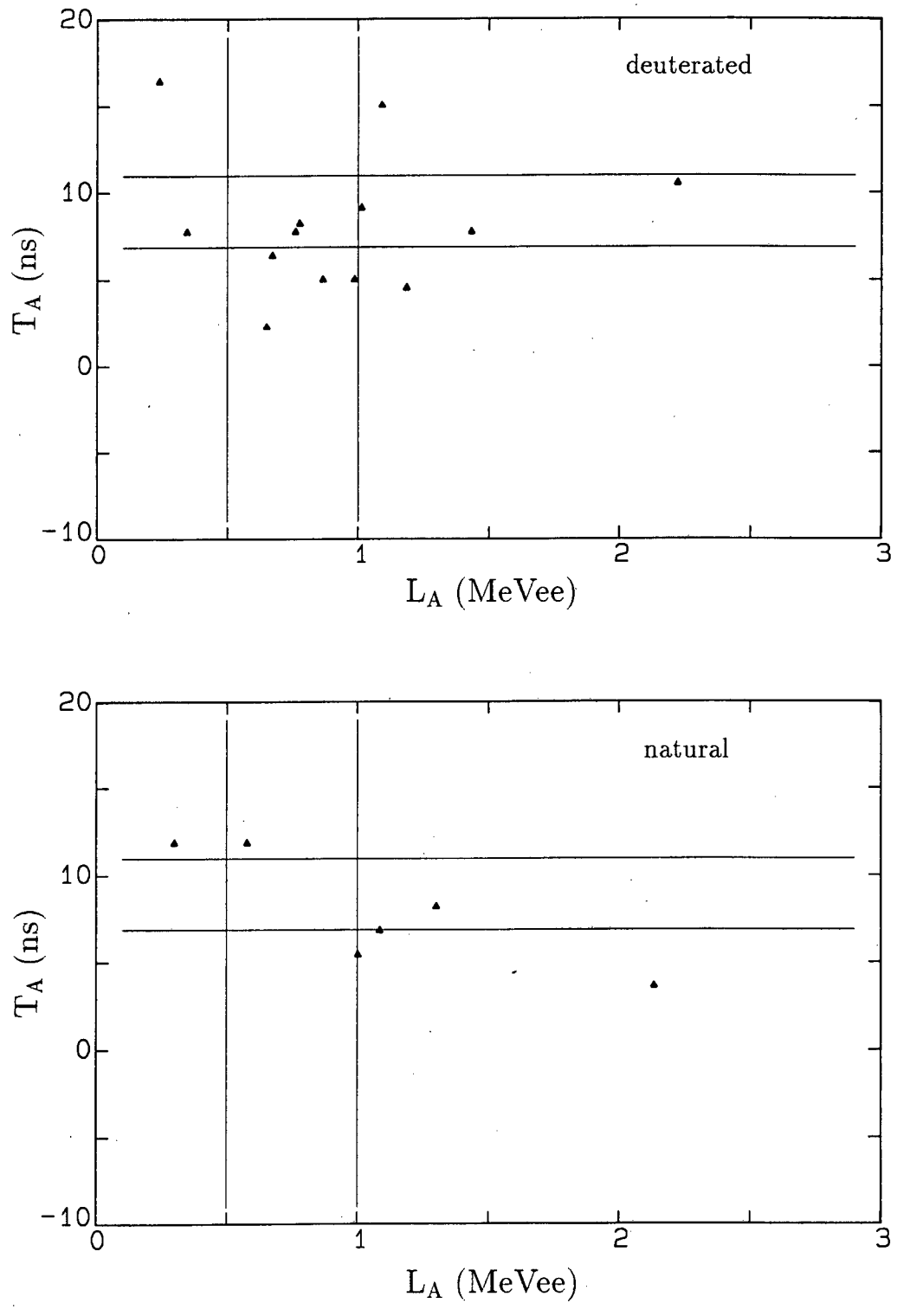

Figure 3.21: T_A vs L_A for the 'basic' cuts + LS_μ^C *and* L_C. The upper and lower plots show data from the deuterated and natural anthracene runs respectively.

muon scavenging by carbon, it does not seem completely unrealistic in the light of the 150 fusions per muon [Br 89] observed at liquid hydrogen densities.

3.5.5 Phase 2: Summary

Improvements introduced in this second experiment, after the experience gained in the first, include the following: the thickness of the plastic scintillator M used to tag charged particles into the crystal C was increased in order to ensure the detection of muons passing through it. The stilbene crystal V placed behind C was effective in eliminating events in which particles escaped from the crystal, thus reducing the background in the $L_C T_M$ planes. Pulse shape discrimination was introduced for the two anthracene crystals C, enabling events lying on the gamma, proton, deuteron and alpha particle loci in the $L_C S_C$ plane to be rejected.

These improvements contributed in such a way as to make the various cuts selecting possible μCF candidates rather more stringent than before. It then became possible to estimate, for each of four sets of cuts, the number of fusion neutrons n_F observed in detector A (thus indicating μCF in deuterated anthracene). If $\sqrt{n}$ statistics are assumed valid then each of these cut sets gives a result consistent with the detection of μCF significant to about the one standard deviation level. There does, therefore, seem to be a hint of a suggestion that muon-catalysed dd fusion may have occurred in the deuterated anthracene crystal.

Chapter 4

Conclusion

4.1 Overview and summary

The objective of this work was to seek evidence of muon-catalysed dd fusion in a solid deuterated hydrocarbon environment. This required an initial muon production test experiment to be performed at the NAC, its aim being to assess the feasibility of producing negative muons for use in a μCF experiment involving deuterated anthracene. The idea of producing negative muons using a 200 MeV proton beam was an ambitious one, for in addition to the sub-threshold incident proton energy, π^- mesons are created less effectively in pn- than in nn-collisions (and practically never in pp-collisions) [Po 90]. The choice of a neutron rich target such as ^{nat}Pb could only partially compensate for this.

An expected muon flux at the catcher (the position which the deuterated anthracene crystal would occupy in a μCF experiment) of 0.014 cm^{-2} min^{-1} was calculated, using approximations based on published cross-section data for (p,π) reactions from 201 MeV protons on ^{nat}Pb. The total muon flux estimated from the measurements, which were hampered by high backgrounds from cosmic muons, was 0.71 ± 0.35 cm^{-2} min^{-1}. Attempts to eliminate the cosmic muon background using a veto detector were foiled by uncertainties regarding the operating threshold and efficiency of the detector. The flux of negative muons, required for the μCF experiment, was estimated to be 0.024 of the total flux, or 0.012 ± 0.008 cm^{-2} min^{-1}. This very low μ^- rate was not fully appreciated, however, until after the μCF experiments with deuterated anthracene had been performed.

The search for μCF in deuterated anthracene comprised two stages: in the first experiment the deuterated and natural anthracene crystals were placed (in turn) outside a kapton window which sealed off the accelerator vacuum. A thin plastic passing detector was placed upstream of the window, inside the flight pipe, its purpose being to tag muons into the crystal. Background signals from particles passing right through the crystal contributed to the difficulties of identifying muons on T_M vs L_C plots. Various measures were taken to relieve some of these difficulties in the second experiment. The crystals were oriented differently so that each presented a greater thickness of (deuterated) anthracene to the beam, and events made by particles penetrating the crystals were eliminated by means of a veto detector behind

C. The plastic passing detector was thicker, to ensure the detection of muons, and pulse shape discrimination was introduced for the crystals C. The application of four different sets of cuts to these data resulted in estimates being made of the upper limits on the fusion neutron yield for each cut set. These limits indicated a number of fusions per μ^- of between 1.1 and 0.3, and thus hinted at the possibility of μCF having occurred in the deuterated anthracene crystal.

The major difficulty in both of these experiments was the very low muon flux incident on the crystals. Although the μCF signal looked for was a very clear one, the combination of the inevitable muon scavenging by carbon, and the limited solid angle of the NE213 scintillator, made the probability of detecting fusions very small indeed. In addition, the system was designed to look for evidence of the fusion channel $dd\mu \rightarrow {}^3He + n$, ignoring the alternative $dd\mu \rightarrow t + p$, while the branching ratio for these reactions is $Y_n/Y_p = 1.39 \pm 0.04$ [Br 89]. These effects, while they would still be present, could be largely overcome if the experiment were to be repeated at a muon facility which could deliver a high flux of low-energy[1] negative muons into the crystal. A clear muon locus would then appear in the $L_C T_M$ plane, and it is possible that a signal in the crystal from the simultaneous detection of a μ^- and a ^{3}He nucleus would have a distinctive pulse shape, whilst having a pulse height not significantly different from that of a single muon. Events from muon-catalysed fusion in the crystal could then be extracted by means of appropriate, highly selective software cuts on the data.

4.2 Mass separation by time-of-flight: applications

The $L_C T_M$ scatter plots introduced in Chapter 3 show how the technique of mass separation by time-of-flight can be used for particle identification. A sufficiently long flight path ensures that particles of different masses are separated at each TOF when this parameter is plotted against detector pulse height (which is a function of particle energy for each particle type).

While there are other techniques for particle identification, this method of separation has an important application in the field of nuclear physics: it could provide invaluable information regarding the responses of various detectors to different types of charged particle. Nuclear and particle physics experiments invariably depend on the detection and identification of many different reaction products. A knowledge of the detector responses for a particular type of charged particle is therefore of crucial importance. In addition to the dependence of detector pulse height on incident particle energy (i.e. the response), the lineshape (response function) of the detector for monoenergetic incident particles is also energy dependent. In particular, the energy dependence of the lineshape is interesting for energies $\geq$ 100 MeV, as nuclear interactions compete more strongly with electronic interactions in this realm, and the lineshape is thus broadened on the lower pulse height side.

[1]The energy of the muons must be sufficiently low for them to come to rest in the crystal.

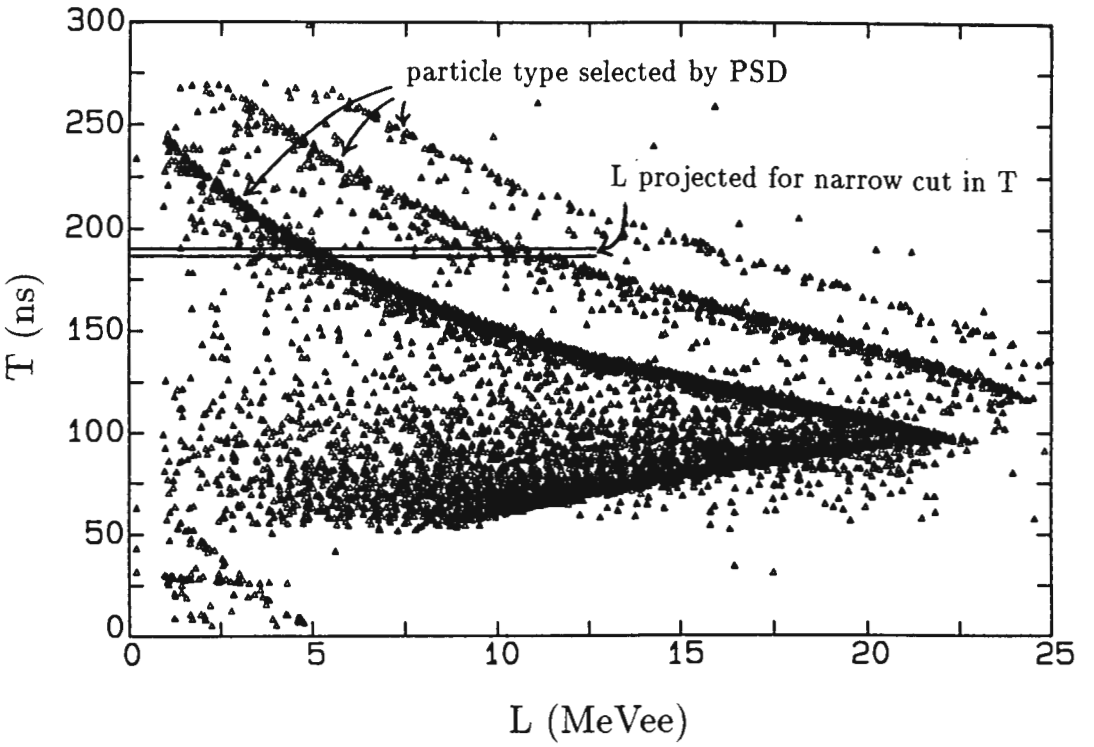

Figure 4.1: Time-of-flight T over 8 metres versus pulse height L in deuterated anthracene, showing loci distinguishing various types of particle. In general the PSD of the detector under study could be used to identify the required type of particle, the projection of L for a narrow cut in T then giving the detector lineshape at that particle energy.

The flight pipe used for the muon experiments at the NAC provides an ideal environment for collecting detector response data. Different charged particles with energies over a wide range could be produced by bombarding a thick (1 mm) lead target with 200 MeV protons, as was done in the muon experiments. With the detector to be investigated placed in the position of the anthracene crystal used previously (see Figure 3.1), the times-of-flight and pulse heights of the particles could be observed simultaneously. For each point on the locus of a specific particle the TOF coordinate would give the particle energy, while the pulse height coordinate would give the corresponding pulse height response. The lineshape of a particle at each energy could be obtained by projecting a narrow cut in TOF onto the pulse height axis (see Figure 4.1), with PSD being employed to select the required particle. This would prevent the desired lineshape from being corrupted by the reaction tails of other particles satisfying the TOF cut. Particles not brought to rest in the detector under study could be vetoed using a second detector behind the former.

Response data could be obtained in this manner for a variety of detectors e.g. liquid scintillator NE213, plastic scintillator NE102A, sodium iodide and caesium iodide crystal scintillators, and silicon semiconductor detectors. In addition, pulse shape data could be measured as a function of particle type and energy, particularly for the organic detectors and caesium iodide.

Appendix A

Energy requirement for pion production from proton-nucleon collisions

Consider a two-body collision in the laboratory frame (S) between a free, stationary target particle of mass m_1 and an incident beam particle of mass m_2 and speed v. In the centre-of-mass frame (S') the incident and target particles approach each other with speeds v' and u respectively (Figure A.1). The speed of S' moving through S is then also u.

In the special case where the incident and target particles have equal rest masses, such as for a proton colliding with a nucleon, $m_1 \simeq m_2 = m_N$, and $v' = u$.

The relation between the total energies in the two frames is given by the Lorentz transformation equation

$$E_{total} = \gamma(E'_{total} + \beta c P'_{total}) \ ,$$

where

$$\gamma = \left(1 - \frac{u^2}{c^2}\right)^{-\frac{1}{2}} \ .$$

Since $P'_{total} = 0$ in the centre-of-mass frame, this becomes

$$E_{total} = \gamma E'_{total} \ .$$

However, in this situation of equal-mass target and projectile particles,

$$E'_{total} = 2\gamma m_N c^2 \quad \text{i.e.} \quad \gamma = \frac{E'_{total}}{2m_N c^2} \ ,$$

so that

$$E_{total} = \frac{E'^2_{total}}{2m_N c^2} \ .$$

Now the kinetic energy T of the incident proton in the laboratory frame is given by $T = E_{total} - 2m_N c^2$, i.e.

$$T = \frac{E'^2_{total}}{2m_N c^2} - 2m_N c^2 \ .$$

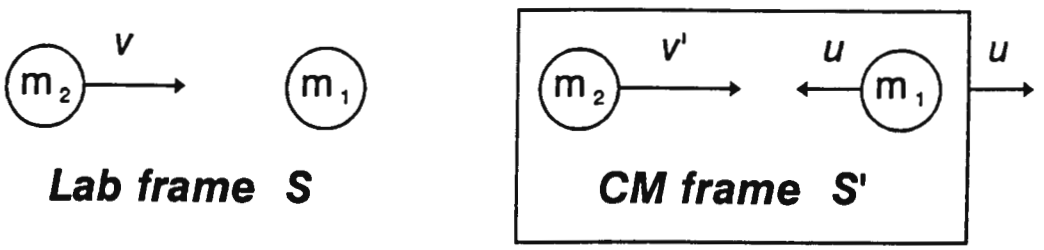

(a) (b)

Figure A.1: A two-body collision in (a) the laboratory frame S, and (b) the centre-of-mass frame S'.

After substituting the minimum total energy required for pion production in the centre-of-mass, $E'_{total} = 2m_N c^2 + m_\pi c^2$, this equation reduces to

$$T = m_\pi c^2 \left(2 + \frac{m_\pi}{2m_N}\right) .$$

Using $m_\pi c^2 = 140$ MeV and $m_N c^2 = 939$ MeV, the minimum kinetic energy required for pion production from a proton incident on a free, stationary nucleon is found to be 290 MeV.

Appendix B

Construction of the K detectors

The two NE213 liquid scintillators A and B which were used in the experiments described in Chapters 2 and 3 are referred to collectively here as the K detectors.

Each detector comprises a tinplate and glass cell of dimensions $13 \times 13 \times 7$ cm^3 containing NE213, and four photomultiplier tubes arranged as illustrated in Figure B.1. The inner walls of the cell are painted with reflecting paint, except where the photocathode faces of the tubes are coupled to the glass with optical grease.

Four rods extend out from the corners of each 7×13 cm^2 face, forming a frame around which a light-tight tin or aluminium foil and cardboard housing is constructed to contain the photomultiplier tubes. Two adjacent photomultiplier bases are built into the lid of the housing, with appropriate spring mountings to ensure that good light seals are maintained between the tubes and the glass cell walls. An anode signal is taken from each tube, and each pair of tubes runs off a single high voltage (HV) power supply. The power supplied to one of each pair of tubes can, however, be varied slightly from that of its partner by means of a potentiometer in the circuitry of its base. This ensures that the gains of the tubes can be matched to give the detector a good lineshape by supplying an appropriate HV to each tube.

B.1 Selecting photomultiplier tubes

As mentioned above, the quality of the K detector lineshape depends on the gains of its four phototubes. Since these gains vary with HV, the lineshape will be best when the high voltages are set to match the gains. Each tube will then give the same pulse height for a particular scintillation.

Tests were therefore performed on a number of tubes to establish their responses to changes in HV and to find voltages at which their gains were equal.

Each tube was subjected to the following procedure: a ^{241}Am alpha source, which gives rise to 5.4 MeV alphas, was placed on a plastic scintillator (2 cm diameter $\times$ 0.5 cm thickness) which was mounted onto the face of the tube. The anode output was connected via an Ortec 113 preamplifier to an Ortec 572 amplifier, whose output was fed into a multichannel analyser (MCA). Starting at a HV of 1500 V and with the amplifier coarse gain (CG) at $\times$50, the peak position in channel number was noted. This was repeated for a CG of $\times$20, and the two channel numbers used to

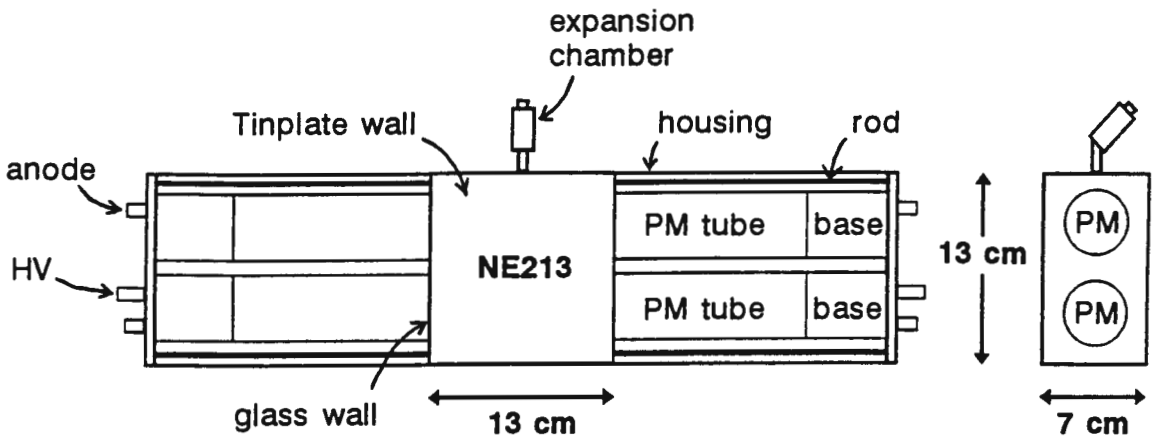

Figure B.1: Schematic diagram showing two views of a K detector.

find the position of true zero in the MCA spectrum. The CG was then set back to $\times 50$, and peak positions, corrected for true zero, were recorded for high voltages of 1485 V, 1455 V, 1425 V and 1395 V.

For each tube tested subsequent to the first one, the HV necessary to bring the peak into the channel corresponding to that of the first tube at 1500 V and CG $\times 50$ was recorded. The information obtained in these tests made it possible to select two pairs of closely-matched tubes for each K detector, bearing in mind that each pair of tubes would be run off a single HV supply.

Appendix C

Pulse Shape Discrimination

C.1 Basis for the technique

The passage of an ionizing particle through an organic scintillator has a number of effects. The incident particle produces primary excitations directly via the Coulomb interaction, and also releases secondary electrons, which themselves cause excitations as they come to rest in the scintillator environment. For heavily ionizing particles (p, d or α) this results in a particle path consisting of a core region (or track) of very high excitation density, with a surrounding region of excitation and ionization from the δ-rays. Localized regions of high excitation density can also occur outside the primary track.

The distribution of primary energy across the track and its surrounds, and the densities of primary excitations in these regions are determined by the charge Z, the energy E (hence velocity) and the specific energy loss dE/dx of the particle. Each of the regions along the particle's path length contributes to the scintillation process. The excitation and scintillation decay processes are described in detail in the review by Brooks [Br 79]. The latter process can be summarised as follows: a scintillation comprises two components. One is prompt and decays exponentially with a lifetime of the order of a few nanoseconds, while the other is a delayed, non-exponential component having a lifetime of around 300 ns. These components are illustrated in Figure C.1.

Since the components of a scintillation differ in their sensitivity to specific energy loss, their relative integrated intensities depend on dE/dx, and thus on the type of particle which produced the scintillation. Particle identification by pulse shape discrimination (PSD) is made possible by this phenomenon.

The PSD technique was originally developed in order to distinguish neutrons from γ-rays in scintillators. Figure C.2 shows the effect of the variation in the relative intensities of the prompt and delayed scintillation components on the light intensity vs time for neutrons and gammas in an NE218 liquid scintillator.

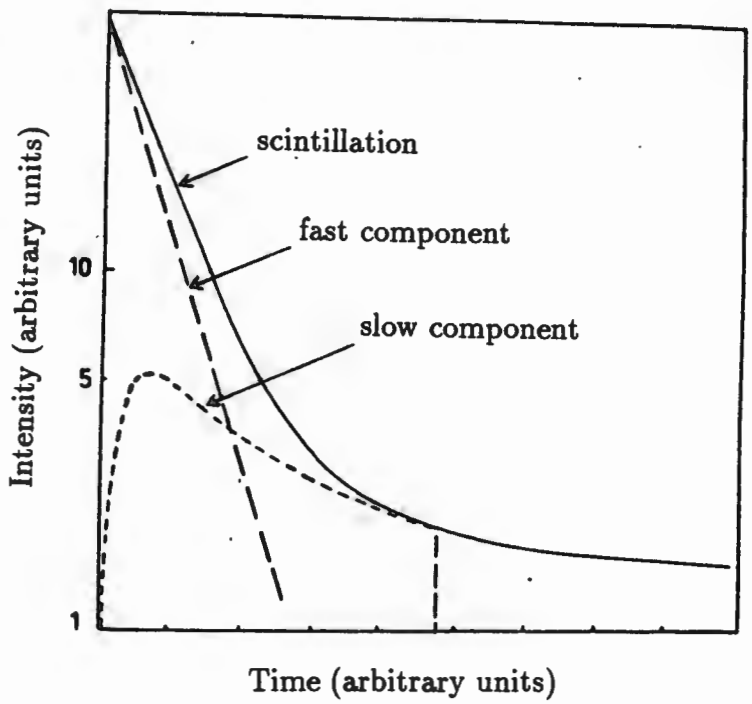

Figure C.1: Schematic representation of the scintillation decay of an organic scintillator, showing both the prompt and delayed components. From [Vo 68].

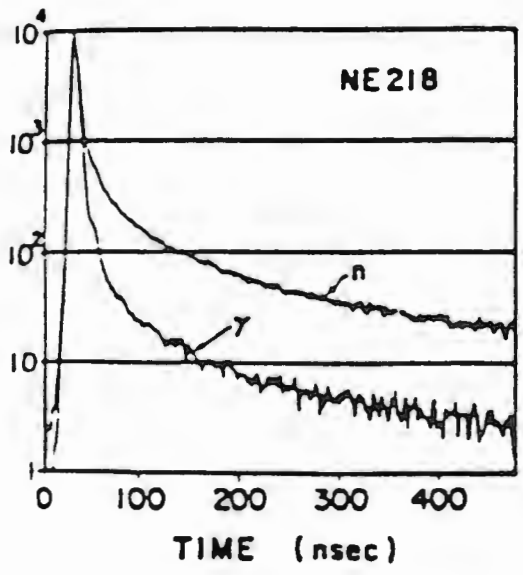

Figure C.2: Measured light intensity vs time t for scintillations produced by neutrons and γ-rays in NE218. From [Ku 68].

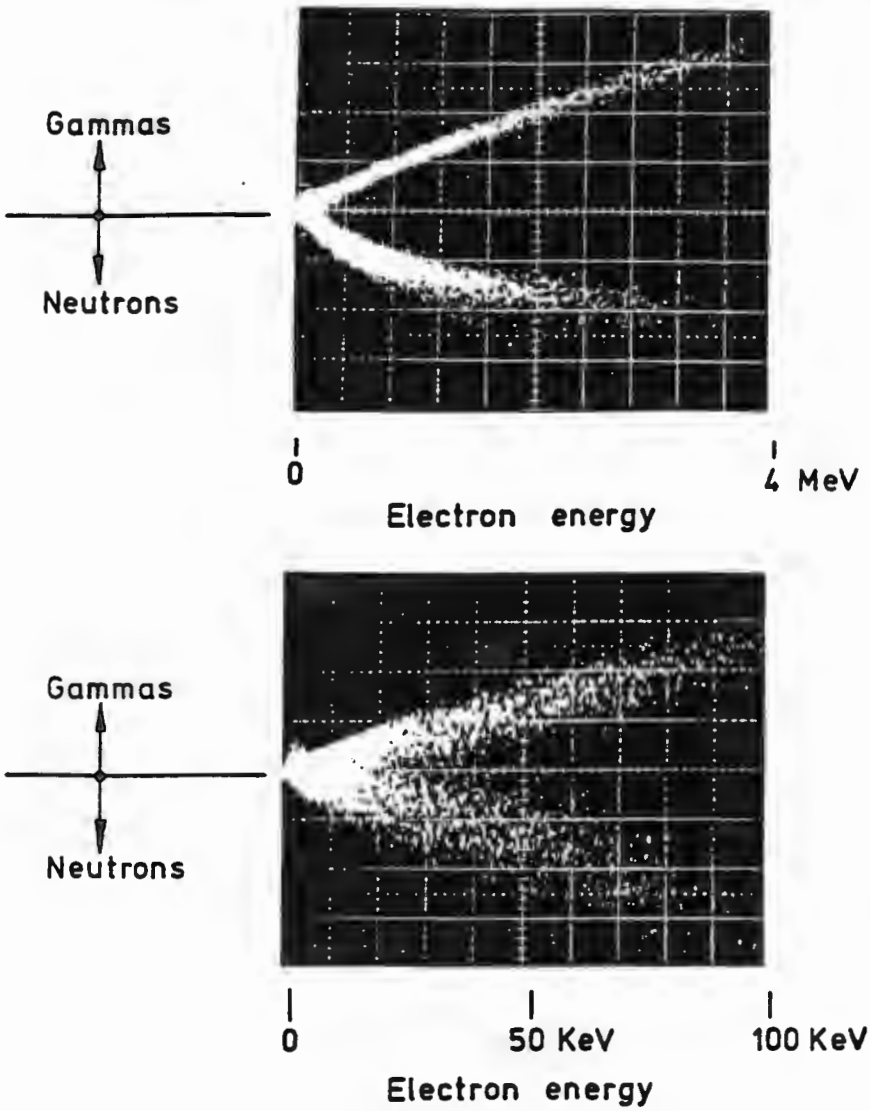

Figure C.3: Oscilloscope displays showing n-γ separation down to 30 keVee. From [Ad 78].

C.2 The Link 5010 Pulse Shape Discriminator

A few different methods of PSD now exist [Br 79]. One of these, that of charge comparison [Br 59], was used in the construction of a PSD instrument first designed and produced at the UKAEA[1], Harwell [Ad 78], which is now commercially available from Link Systems Ltd. This instrument is a double width NIM module with outputs to an oscilloscope in addition to those for particle identification, fast timing and an integrated signal. The oscilloscope outputs produce displays such as those shown in Figure C.3.

A simplified block diagram of the electronics contained in the 5010, showing waveforms, is displayed in Figure C.4. The anode signal from the detector photomultiplier triggers a constant fraction discriminator which opens two gated integrators. The signal itself is delayed by a short cable until the gates are fully open, after which it is integrated for times T_1 and T_2, typically 25 ns and 400 ns respectively.

[1]United Kingdom Atomic Energy Authority

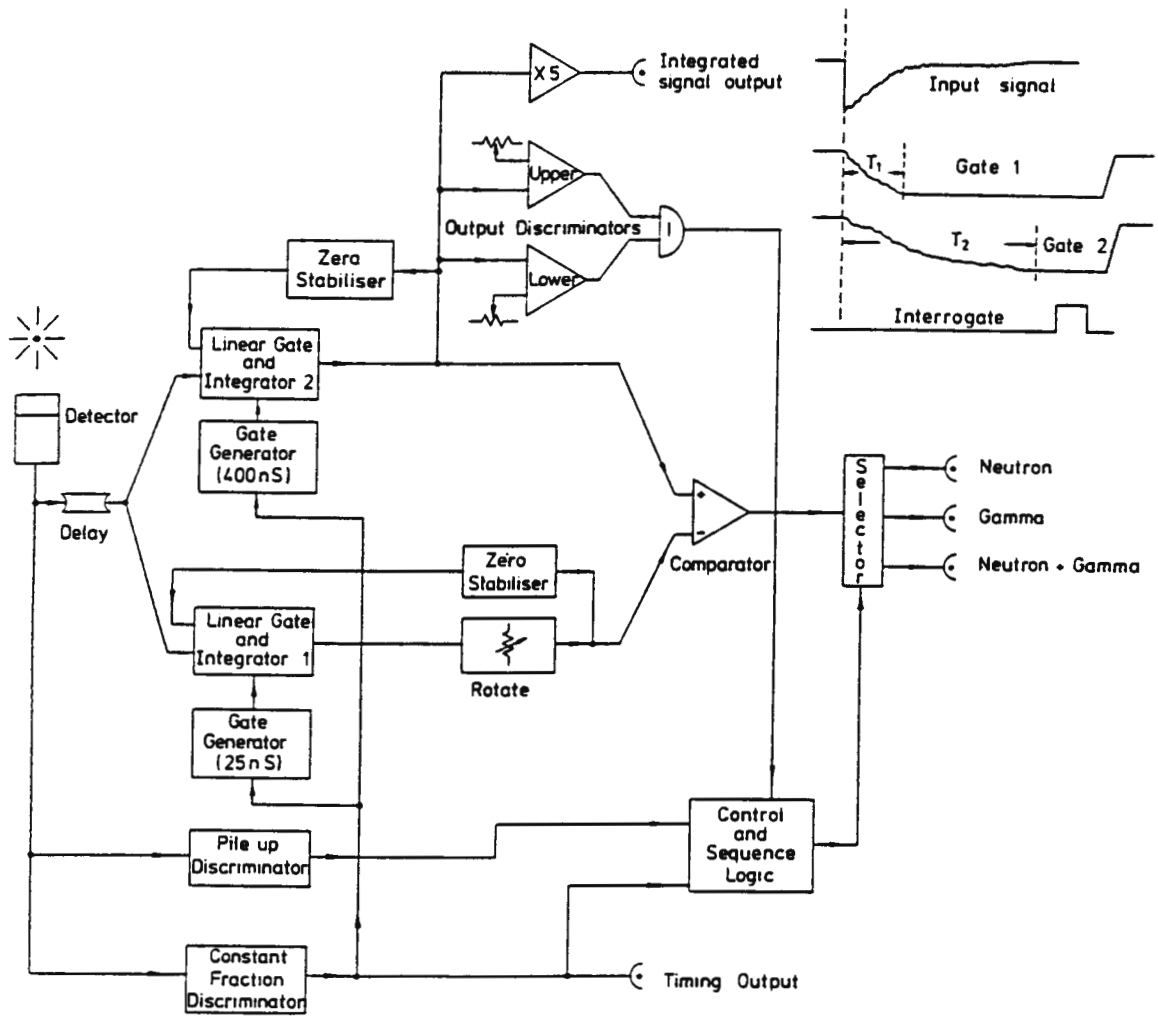

Figure C.4: Simplified block diagram of the electronics contained in the pulse shape discriminator. Waveforms of the input signal and the two integrated output signals, and the logic pulse which interrogates the comparator are also shown. From [Ad 78].

A comparator which is interrogated after T_2 indicates a neutron or a γ-ray by comparing the weighted outputs of the two integrators. If Q_1 and Q_2 are the charges collected during times T_1 and T_2 respectively, and K_1 and K_2 are weighting factors, then $K_1Q_1 > K_2Q_2$ identifies a γ-ray, while $K_1Q_1 < K_2Q_2$ identifies a neutron. The range of the integrated signal output L is controlled by the upper and lower output discriminators. The pile up discriminator inhibits the NEUTRON and GAMMA outputs if it detects another event during T_2. A detailed description of the circuitry, oscilloscope display options and PSD capabilities of the unit is given in the paper by Adams [Ad 78].

C.2.1 A useful modification of the Link 5010

The Link PSD units used in the experiments described in this work were modified so as to provide a signal output F from Integrator 1. The outputs L and F are parameters of each event which can then be combined in the off line data analysis to form the pulse shape S. This makes it possible to identify particles other than just neutrons and gammas. The pulse shape is given by

$$S = L - kF + C$$

where k and C are constants chosen to give the best particle separation for a particular scintillator. Figure C.5 shows a perspective view of counts plotted against pulse height L and pulse shape S for 63 MeV neutrons incident on an NE213 liquid scintillator. It shows clearly how particle identification is possible using the F output modification to the Link PSD module.

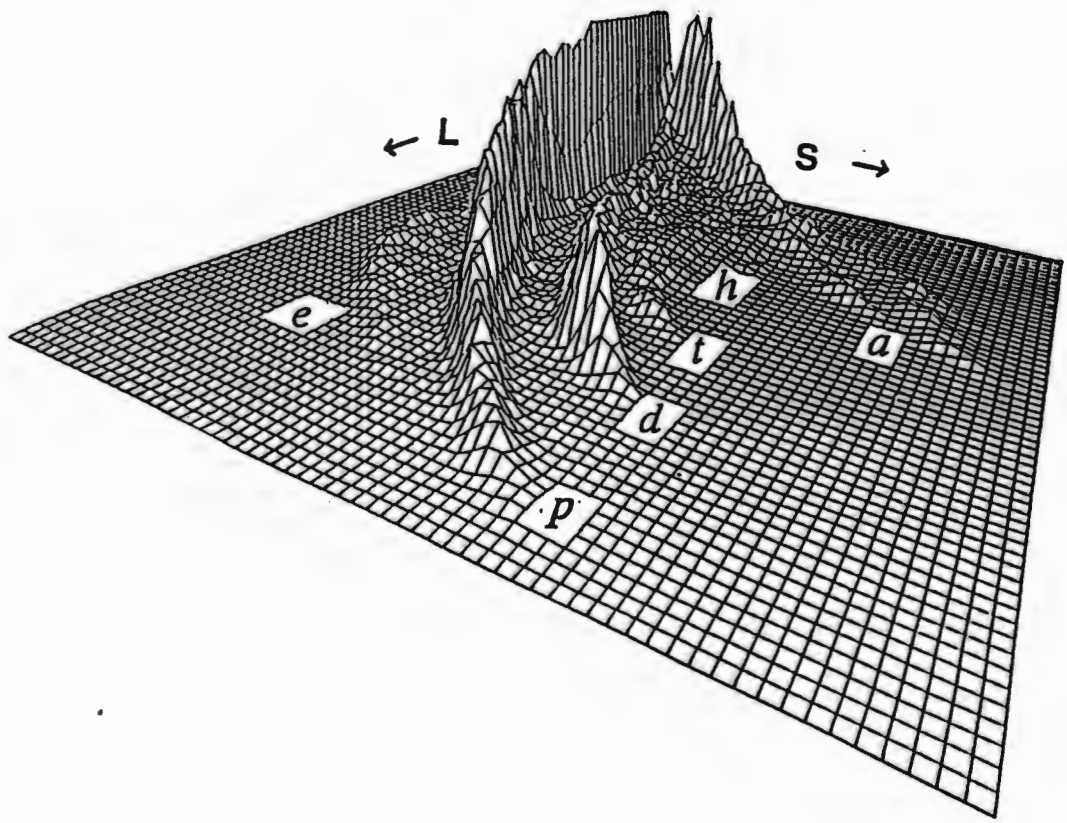

Figure C.5: Counts (vertical) versus pulse height L and pulse shape S for events in an NE213 scintillator exposed to 63 MeV neutrons. The loci associated with various charged particles are (p) protons, (d) deuterons, (t) tritons, (h) ^{3}He nuclei and (a) alpha particles. The locus (e) is due to escaping protons (i.e. those not brought to rest in the scintillator). From [Bu 90].

Bibliography

[Ad 78] J.M. Adams and G. White, Nucl. Instr. Meth. **156** (1978) 459.

[Al 57] L.W. Alvarez *et al.*, Phys. Rev. **105** (1957) 1127.

[Al 72] L.W. Alvarez *at al.*, Advent. Exp. Phys. α (1972) 72.

[An 36] C.D. Anderson and S.H. Neddermeyer, Phys. Rev. **50** (1936) 263.

[An 61] C.D. Anderson, Am. J. Phys. **29** (1961) 825.

[Ba 65] M. Bardon *et al.*, Phys. Rev. Lett. **14** (1965) 449.

[Ba 84] D.V. Balin *et al.*, Phys. Lett. **141B** (1984) 173.

[Bi 70] J.B. Birks, *Photophysics of Aromatic Molecules*, John Wiley & Sons Ltd., London, 1970, p. 44.

[Bi 85] L. Bimbot *et al.*, Nucl. Phys. **A440** (1985) 636.

[Bo 85] T. Bowen, Physics Today, July 1985, 23.

[Br 59] F.D. Brooks, Nucl. Instr. Meth. **4** (1959) 151.

[Br 74] F.D. Brooks and D.T.L. Jones, Nucl. Instr. Meth. **121** (1974) 69.

[Br 79] F.D. Brooks, Nucl. Instr. Meth. **162** (1979) 477.

[Br 82] L. Bracci and G. Fiorentini, Phys. Rep. **86** (1982) 169.

[Br 84] W.H. Breunlich *et al.*, Phys. Rev. Lett. **53** (1984) 1137.

[Br 88] F.D. Brooks *at al.*, Nucl. Instr. Meth. **A270** (1988) 149.

[Br 89] W.H. Breunlich *et al.*, Ann. Rev. Nucl. Part. Sci. **39** (1989) 311.

[Bu 90] A. Buffler, M.Sc. thesis (unpublished), University of Cape Town, 1990.

[By 80] V.M. Bystritsky *et al.*, Phys. Lett. **94B** (1980) 476.

[Cl 82] J.L. Clark *et al.*, Phys. Rev. **C26** (1982) 2073.

[Co 83] J.S Cohen, Phys. Rev. **A27** (1983) 167.

[Fa 91] M.P. Faifman and L.I. Ponomarev, Phys. Lett. **B265** (1991) 201.

[Fe 47] E. Fermi and E. Teller, Phys. Rev. **72** (1947) 399.

[Fr 47] F.C. Frank, Nature, **160** (1947) 525.

[Ge 77] S.S. Gerstein and L.P. Ponomarev, Phys. Lett. **72B** (1977) 80.

[Ge 81] S.S. Gerstein *et al.*, Sov. Phys. JETP **53** (1981) 872.

[Jo 83] S.E. Jones *et al.*, Phys. Rev. Lett. **51** (1983) 1757.

[Jo 86] S.E. Jones *et al.*, Phys. Rev. Lett. **56** (1986) 588.

[Ku 68] F.T. Kuchnir and F.J. Lynch, IEEE Trans. Nucl. Sci. **NS-15**, no. 3 (1968) 107.

[Le 84] M. Leon, Phys. Rev. Lett. **52** (1984) 605.

[Lo 82] D.G. Long *et al.*, Phys. Rev. **C26** (1982) 586.

[Ma 79] R.E. Marrs and R.E. Pollock, Phys. Rev. **C20** (1979) 2446.

[Mc 47] W.G. McMillan and E. Teller, Phys. Rev. **72** (1947) 1.

[Ne 37] S.H. Neddermeyer and C.D. Anderson, Phys. Rev. **51** (1937) 884.

[Ne 38] S.H. Neddemeyer and C.D. Anderson, Phys. Rev. **54** (1938) 88.

[Po 90] L.I. Ponomarev, Contemp. Phys. **31** (1990) 219.

[Sa 48] A.D. Sakharov, Report of the Physics Institute, Academy of Sciences, USSR, 1948 (unpublished).

[St 37] J.C. Street and E.C. Stevenson, Phys. Rev **52** (1937) 1003.

[Th 79] P.A. Thompson *et al.*, Nucl. Instr. Meth. **161** (1979) 391.

[Ve 67] E.A. Vesman, Sov. Phys. JETP Lett. **5** (1967) 91.

[Vi 77] S.I. Vinitsky *et al.*, Preprint JINR P4-10929, Dubna (1977). Later published in Zh. Eksp. Teor. Fiz. **74** (1978) 849.

[Vo 68] R. Voltz *at al.*, J. Physique **29** (1968) 297.

[Wu 69] C.S. Wu and L. Wilets, Ann. Rev. Nucl. Sci. **19** (1969) 527.

[Ya 75] T. Yamazaki *et al.*, Physica Scripta **11** (1975) 133.

[Ze 54] Ya.B. Zel'dovich, Dokl. Akad. Nauk SSSR **95** (1954) 493.